Chem Soc Rev

ROYAL SOCIETY OF CHEMISTRY

REVIEW ARTICLE

View Article Online
View Journal | View Issue

Check for updates

Cite this: *Chem. Soc. Rev.*, 2021, **50**, 6569

The challenges, achievements and applications of submersible superhydrophobic materials†

Yasmin A. Mehanna, [ab] Emma Sadler, [b] Rebekah L. Upton, [ab] Andrew G. Kempchinsky, [b] Yao Lu [c] and Colin R. Crick *[c]

Superhydrophobic materials have been widely reported throughout the scientific literature. Their properties originate from a highly rough morphology and inherently water repellent surface chemistry. Despite promising an array of functionalities, these materials have seen limited commercial development. This could be attributed to many factors, like material compatibility, low physical resilience, scaling-up complications, *etc.* In applications where persistent water contact is required, another limitation arises as a major concern, which is the stability of the air layer trapped at the surface when submerged or impacted by water. This review is aimed at examining the diverse array of research focused on monitoring/improving air layer stability, and highlighting the most successful approaches. The reported complexity of monitoring and enhancing air layer stability, in conjunction with the variety of approaches adopted, results in an assortment of suggested routes to achieving success. The review is addressing the challenge of finding a balance between maximising water repulsion and incorporating structures that protect air pockets from removal, along with challenges related to the variant approaches to testing air-layer stability across the research field, and the gap between the achieved progress and the required performance in real-life applications.

Received 16th October 2020

DOI: 10.1039/d0cs01056a

rsc.li/chem-soc-rev

1 Introduction

Highly water repellent (superhydrophobic) materials have received significant interest in recent years, due to their emerging potential and future implementation as innovative solutions to overcome real-word challenges.[1,2] Many artificial superhydrophobic surfaces are inspired by those found in nature, as numerous plants and insects have evolved natural superhydrophobic coatings over time (outlined in Section 2), for example; the lotus leaf, rice leaves, *Salvinia molesta* leaves, mosquito eyes, butterfly wings, in addition to many more.[3–8] The most widely-recognised natural superhydrophobic surface, firstly reported by Barthlott and Neinhuis, is the lotus leaf (*Nelumbo nucifera*).[4,9] This natural template has given rise to the self-cleaning phenomenon, 'the Lotus Effect'. The Lotus leaf architecture consists of micro-sized setae, affixed with

[a] *Materials Innovation Factory, Department of Chemistry, University of Liverpool, Liverpool L69 7ZD, UK*
[b] *School of Engineering and Materials Science, Queen Mary University of London, Mile End Road, London E1 4NS, UK*
[c] *Department of Chemistry, School of Biological and Chemical Sciences, Queen Mary University of London, Mile End Road, London E1 4NS, UK. E-mail: c.crick@qmul.ac.uk*

† Electronic supplementary information (ESI) available. See DOI: 10.1039/d0cs01056a

Yasmin A. Mehanna

Yasmin obtained her bachelor's degree in Materials Science from University of Science and Technology-Zewail City, Giza, Egypt in 2017. She worked in polymer research related to different applications (porous conducting polymers, polymeric fuel cell membranes). She joined the Crick Group in 2018. Her PhD research focuses on superhydrophobic polymer/polymer composite coatings.

Emma Sadler

Emma obtained a first-class Master's degree in Chemistry from the University of Liverpool in 2019. Currently, she is a PhD student in materials science under the supervision of Dr Colin Crick at Queen Mary, University of London. Her research focuses on submerged superhydrophobic materials and their use in antifouling applications.

nano-grooves, both of which are coated in a water-repelling wax. Subsequently, this facilitates an intrinsic mechanism, in which falling rainwater beads into near-spherical droplets and can efficiently clean the leaf surface, removing surface-bound dirt and/or bacteria. The low frictional adhesion of water to the leaf surface enables a beneficial rolling motion, and has received a tremendous amount of interest in the scientific literature, due to the wide range of properties it can give rise to if successfully integrated into synthetic coatings, including; self-cleaning, anti-fouling, drag reduction, anti-corrosion, *etc.*[10–13]

1.1 Superhydrophobic materials fabrication

Throughout the literature, diverse routes of engineering artificial superhydrophobic surfaces have been established, frequently involving the fabrication of biomimetic surfaces *via* the replication of natural architectures (*e.g.* using techniques such as soft lithography, moulding and/or templating).[6] In general, superhydrophobic materials utilise a combination of multi-scale surface roughness and an intrinsically hydrophobic material/surface coating. Fabrication techniques, therefore, require a method of inducing both surface texturing and surface hydrophobicity, or alternatively, generating both simultaneously. Generally, these techniques fall into two categories; (i) 'top-down' techniques which involve the removal/deposition of a bulk material to generate surface roughness and includes techniques, such as; lithography, chemical etching, plasma etching and micro-machining, or (ii) 'bottom-up' techniques where surfaces are structured and built-up *via* the collection of small building blocks (*e.g.* molecular precursors/nanomaterials), including; chemical vapour deposition, electrospinning and more facile techniques (spray coating, dip coating, spin coating, *etc.*).[14–22] Both classes of techniques have found equal success in fabricating synthetic superhydrophobic surfaces. However, limiting factors relating to complexity, equipment costs and compatible precursor materials can determine the suitability of each technique, specific to the coating/surface requirements.

1.2 Wetting models

Understanding the inherent wetting behaviour of any given surface is of high importance as it allows for fine-tuning of the

Rebekah L. Upton

Rebekah is a final year PhD student, currently working within Dr Crick's group, on the development of polymer–nanoparticle composite superhydrophobic coatings. She studied undergraduate chemistry at the University of Liverpool between 2013–2017, where she obtained a first class MChem degree and has remained to conduct her PhD research.

Andrew G. Kempchinsky

Andrew completed his MSc dissertation in the Crick Lab at Queen Mary, University of London with a focus on antifouling and the wetting behaviour of biological surfaces. Andrew has since joined the Bullman Lab at the Fred Hutchinson Cancer Research Center in Seattle, Washington, USA where he is focused on the micron-scale interactions of bacterial communities in colorectal tumours.

Yao Lu

Dr Yao Lu is a Lecturer in Chemistry Department at Queen Mary, University of London. He obtained his PhD from UCL Chemistry and was a postdoctoral fellow at UCL Mechanical Engineering. He is interested in nature inspired functional materials such as lotus leaf inspired superhydrophobic surfaces and pitcher plant inspired slippery surfaces, and their applications such as self-cleaning, anti-icing, anti-corrosion and liquid droplet transport.

Colin R. Crick

Dr Colin Crick is a Senior Lecturer in the School of Engineering and Materials Science at Queen Mary, University of London. He undertook his PhD Studies at UCL Chemistry, with postdoctoral experience primarily based at Imperial College London Chemistry. His research interests focus on applied functional materials, and the effect of surface morphology and chemistry on the material properties/functionality. Currently this is primarily focused on the study of superhydrophobic materials and enhancing their potential real-world performance.

surface microstructure to enhance the resultant surface wettability/properties and therefore, govern compatible applications.[23] For example, surface coatings which induce water pinning and surface coatings which have very little contact with water, may be more suitable to different applications. To better understand surface wetting, alternate wetting models have been established and are discussed briefly in the following section.

1.2.1 Young's equation. In general, the wettability of a solid surface is defined by its water contact angle (WCA, θ) – the angle between the plane of the solid surface and the tangent of the air–liquid interface – which in the case of hydrophobic and superhydrophobic materials, is $\theta > 90^\circ$ or $>150^\circ$ respectively.[24] The simplest wetting model, based on a flat and chemically homogenous surface that is in a state of thermodynamic equilibrium, is Young's equation. This model uses interfacial surface tensions/energies (per unit area) to indicate the resultant equilibrium contact angle (eqn (1)).[25]

$$\cos\theta_e = \frac{\gamma_{SV} - \gamma_{SL}}{\gamma_{LV}} \quad (1)$$

When the three interfacial tensions [solid–vapour (γ_{SV}), solid–liquid (γ_{SL}), liquid–vapour (γ_{LV})] balance and reach thermodynamic equilibrium, the contact angle is determined (Fig. 1). For a surface that exhibits a hydrophobic wetting behaviour, the solid–liquid interfacial energy (γ_{SL}) exceeds that of the solid surface free energy (γ_{SV}) and so the water droplet changes shape in order to minimise the solid–liquid interfacial area, until the lowest possible energy state of the system is reached. Therefore, large contact angles are observed, reflecting the hydrophobic nature of the solid surface. The reverse is true for hydrophilic surfaces, where $\theta < 90^\circ$ and $\theta < 5^\circ$ are seen for hydrophilic and superhydrophilic wetting behaviours respectively.

Arguably, no common solid is chemically homogenous and flat. Surfaces generally vary in composition and properties, and therefore, usually contain surface defects/impurities and some extent of surface roughness.[26] Surface roughness is fundamental in developing materials which display high water repellence, owed to the fact that flat surfaces engineered from the lowest surface-energy materials (small energy difference between the bulk material and the surface, hence, forming a new solid–liquid interface with water is energetically unfavourable), *e.g.* $-CF_3$ (6.7 mJ m^{-2}), can only display a maximum WCA of $\sim 120^\circ$.[27,28] An exception to this, being, surfaces which experience the Leidenfrost effect (a physical phenomenon that occurs when liquid is deposited onto a high-temperature surface, not solely dependent on surface chemistry/microstructure, see Section 5.2.3) which have been reported to exhibit WCAs nearing 180°, where the droplet effectively 'levitates' above the surface.[29,30] Young's equation can no longer be used to accurately predict the wetting behaviour of a 'non-ideal' surface, as heterogeneous contact beneath the droplet is not accounted for. As a result, alternative wetting models have been proposed to elucidate the wetting behaviours of real-life solid surfaces.[31,32]

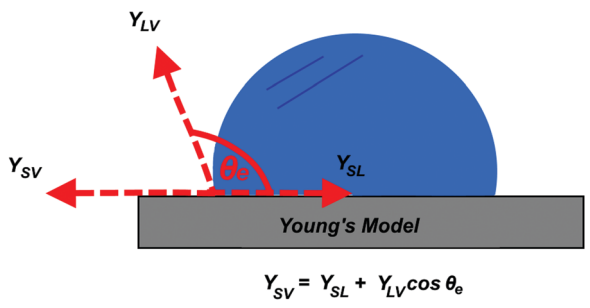

Fig. 1 Illustration of Young's model (including Young's equation), highlighting the equilibrium contact angle (θ_e) and interfacial surface tensions [solid–vapour (γ_{SV}), solid–liquid (γ_{SL}), liquid–vapour (γ_{LV})] of a static water droplet on a flat surface.

1.2.2 Wenzel model. The Wenzel model has been used to relate surface wettability to surface roughness and surface energies, *via* the direct inclusion of a roughness factor (r, eqn (2)):[32,33]

$$\cos\theta_w = r\cos\theta_e = \frac{r(\gamma_{SV} - \gamma_{SL})}{\gamma_{LV}} \quad (2)$$

The roughness factor can be defined as the ratio of the actual surface to the geometric/planar surface (eqn (3)). Therefore, a roughened surface will display a value which exceeds 1.

$$r = \frac{\text{Actual surface}}{\text{Geometric projected surface}} \quad (3)$$

The Wenzel equation presumes a homogeneous wetting state. A state where full contact is made between the solid surface and the liquid (Fig. 2) and determines the extent of surface wettability, based on the net energy change of the dried surface *vs.* that of the wetted surface. As a surface becomes roughened, the surface energy of a particular unit area intensifies in line with the inherent wettability of the surface, due to the increased contact area. It must be noted, that the specific surface energy of a solid cannot be altered, as that is solely dependent on the surface chemistry. However, the energy change associated with the formation/destruction of a new interface will be intensified if the surface is roughened. Owing to this, surface wettability is said to be proportionally related to surface roughness, meaning that an increasingly textured hydrophobic surface will see a corresponding increase in apparent contact angle. Contrastingly, the opposite effect for an inherently hydrophilic material, as θ tends towards 0°.

1.2.3 Cassie–Baxter model. Upon roughening of a surface, it was observed by Cassie and Baxter that pockets of air often become retained within the surface porosity (*i.e.* heterogeneous surface wetting, Fig. 2).[31] Surfaces that follow this wetting regime generally show very little water adhesion and have been defined as 'slippery' by Quéré *et al.*, reflected by their extremely low contact angle hysteresis ($\sim <10^\circ$).[34] Contact angle hysteresis refers to the difference between the advancing contact angle and the receding contact angle of a given surface, which are recorded when water is dispensed into (advancing) or withdrawn from (receding) a droplet resting on the surface, or alternatively, can be recorded when the surface is tilted.[35] When interfacial air is present, water bridges across the tops of the surface microstructures and avoids penetrating the grooves of the surface, contrasting with what is predicted by the Wenzel model.[32] In the Cassie–Baxter model, the interaction of water with a surface is described by considering all

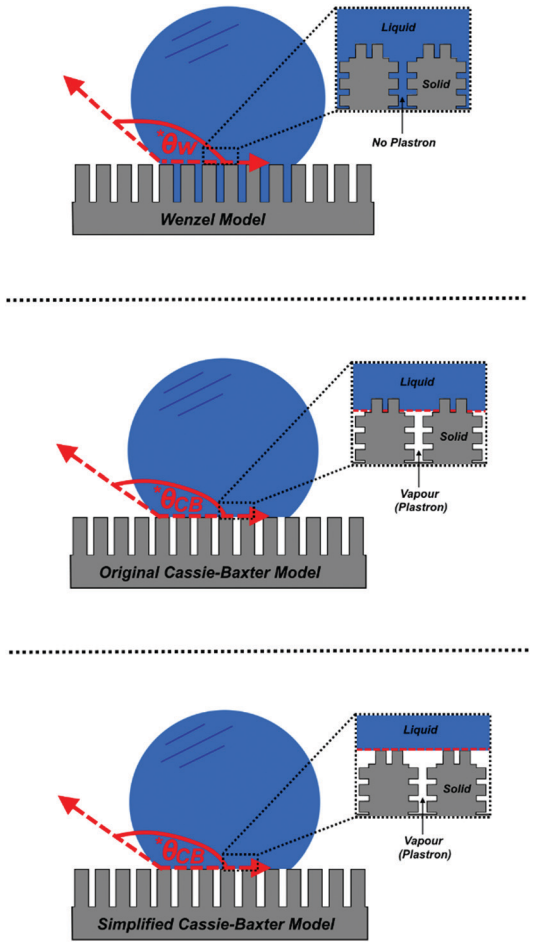

Fig. 2 Schematic to show the interaction of water with a roughened solid surface, as outlined by; the Wenzel regime (top), and original Cassie–Baxter regime (including the roughness factor in the f_1 term, middle) and the simplified Cassie–Baxter version where the solid–liquid interface is considered as flat (bottom).

of the interfacial areas and interfacial energies, including the liquid–vapour interface. The wetting of a hydrophobic surface results in the displacement of a region of solid–vapour interface with two newly generated interfacial areas (solid–liquid and liquid–vapour), in which, the overall net free energy change (E_D) can be considered to be energetically unfavourable. Hence, only a small area of the solid surface becomes wetted and large contact angles are observed for superhydrophobic materials. E_D can be expressed as follows:

$$E_D = f_1\gamma_{SV} - f_1\gamma_{SL} + f_2\gamma_{LV} \quad (4)$$

where f_1 is the total solid–liquid interfacial area and f_2 is the total liquid–vapour interfacial area in a unit of plane geometrical area parallel to the rough surface. An apparent contact angle can then be computed by relating the overall net free energy change to the interfacial surface energies in Young's equation using the advancing contact angle. Hence, the apparent contact angle can be derived as follows:

$$\cos\theta_{CB} = \frac{-E_D}{\gamma_{LV}} = f_1\cos\theta_e - f_2 \quad (5)$$

where θ_{CB} is the apparent contact angle and θ_e is the equilibrium contact angle. In the original model derived by Cassie and Baxter (eqn (5)), the solid surface roughness is accounted for in the solid–liquid interfacial area term, f_1, as it includes the roughness factor, r. Therefore, if the liquid–vapour interfacial area is equal to zero, *i.e.* the surface no longer has any interfacial air, the Cassie–Baxter equation is now said to equal to the Wenzel equation, directly relating both wetting models.

The Cassie–Baxter model can be used to produce exceptionally accurate predictive results, as it aims to describe a wetted interface in detail. However, a comprehensive understanding of how water interacts with any given surface is hard to achieve, as the exact position of the different interfaces cannot be accurately characterised or predicted – particularly for surfaces that do not have repeating structures. As a result, a simplified version of this model has been proposed by Quéré *et al.*, which considers the solid–liquid and liquid–vapour interfaces to be planar, disregarding the roughness factor, and enabling both interfaces to be considered as fractional areas (Fig. 2).[36] Both fractional areas can be assigned – ϕ_S as the solid–liquid interfacial area and $1 - \phi_S$ as the liquid–vapour interfacial area – as the interface is considered planar, the sum of both areas is then equal to 1. This gives rise to the following simplified equation (computing $\cos\theta_{AIR} = -1$):

$$\cos\theta_{CB} = \phi_S\cos\theta_e + \phi_S - 1 \quad (6)$$

The simplified Cassie–Baxter model can be used to successfully predict how changes to the liquid–vapour interfacial area can impact the surface hydrophobicity of a given coating (see Section 1.3.1).

1.3 Importance of retained air

Engineering surfaces that adopt a Cassie–Baxter wetting behaviour is necessary for many applications (see Section 7). Various surface functionalities rely on the presence of air retained within the surface microstructure, primarily to provide 'slippery' surface conditions. This functionality provides a wide range of promising application areas (*e.g.* textiles, building and windows, paints and coatings industries, *etc.*), where a number of synthetic superhydrophobic coatings have already been commercially marketed, *e.g.* NeverWet self-cleaning coatings.[37–39] However, due to their typically low durability, coatings which are designed in the absence of any intrinsic self-healing mechanisms generally exhibit short-term usage before re-application is required to regenerate surface properties.[40–43] Retained air plays a crucial role as it contributes heavily to the generic durability and applicational feasibility of superhydrophobic materials. Although the physical resilience of many materials has been investigated throughout the literature, factors other than mechanical durability can contribute to air-layer degradation, as outlined throughout this review. Therefore, the investigation into maintaining a stable Cassie–Baxter state is of high importance if superhydrophobic materials are to be implemented as real-world innovative technologies.

It must be noted that, while superhydrophobic surfaces are usually being defined by their high WCAs and low tilt angles and WCA hysteresis, surfaces with high air retention ability

don't always possess these characteristics (*i.e.* some surfaces with good air layer stability exhibit a 'pinning effect' (Section 2.2) where a water droplet sticks to the surface and shows a very high tilt angle).[44] For this reason, the use of the 'superhydrophobic' term throughout this review mainly refers to the surface being generally water repellent, rather than stating it fits with the conventional definition of superhydrophobic surfaces.

1.3.1 Surface requirements. The formation of air pockets within the surface microstructure will occur only if the appropriate chemical and structural criteria are met. Quéré *et al.* purposed a critical contact angle to describe the threshold between both Wenzel and Cassie–Baxter wetting states:

$$\cos\theta_C = (\phi_S - 1)/(r - \phi_S) \quad (7)$$

In the case of a highly roughened surface ($r \rightarrow \infty$), θ_C is said to equal 90°. Hence, it was stated that for a highly roughened surface with an $\theta_e > 90°$, a heterogeneous wetting state should be adopted as it becomes favourable for air pockets to form within the porosity of the surface microstructure.[34] Conversely, when $\theta_e < \theta_C$, retained air is generally unfavourable owing to the intrinsic hydrophobicity of the solid surface (determined *via* Young's contact angle) being too low to induce the formation of air pockets. However, states which are not fully stable and can exhibit both Wenzel and Cassie–Baxter characteristics (metastable states), for example, partial penetration into the surface porosity, have been reported to exist (Fig. 3).

As the majority of synthetic superhydrophobic coatings are both; (i) extremely textured and (ii) have an equilibrium contact angle that exceeds 90°, the Cassie–Baxter wetting state is primarily assumed. However, the apparent contact angle is heavily dependent upon the solid–liquid fraction and can be seen to readily decrease as the solid–liquid fraction is enhanced (reducing the volume of retained air).[44] Using the simplified Cassie–Baxter equation (eqn (6)), a surface with a solid fraction of 10% and $\theta_e = \sim 120°$ is predicted to yield an apparent contact angle of $\sim 160°$. Conversely, when the solid fraction is increased to 20% for the same solid material, the expected apparent contact angle is now reduced to $\sim 150°$, highlighting the importance of the liquid–vapour interfacial area. As the apparent contact angle starts to decrease, the surface functionalities will become inhibited, eventually rending the coating unusable.

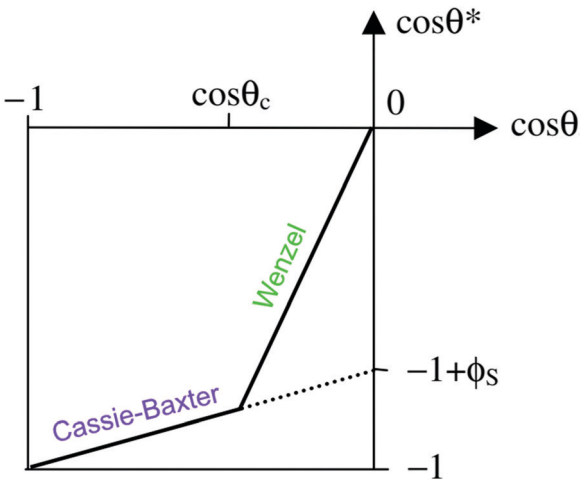

Fig. 3 A diagram showing the different wetting states that are taken by superhydrophobic surfaces; relating the apparent contact angle ($\cos\theta^*$) to the equilibrium contact angle ($\cos\theta$) and the extent of surface roughness/solid surface fraction. The critical contact angle ($\cos\theta_C$) marks the threshold between both wetting states and the dotted line represents a metastable state, in the case that air pockets partially form for surfaces with $\theta < \theta_C$.[34]

1.3.2 Plastrons. Plastrons are defined as the thin air-layer locked within the surface porosity of a solid when wetted, and play a fundamental role in materials which display high contact angles (as seen above).[45] Visually, the plastron can be identified by its inherent slivery mirror-like complex during immersion in water, owing to the total internal reflectance (TIR) of light (Fig. 4) which has been reported to occur at the air–liquid interface by many research groups (Section 3.1.1).[45–50]

The term 'plastron' is commonly used within the biological community and originally evolved to aid the underwater respiration systems of many aquatic insects (*Aphelocheirus*, *Elmidae*, *etc.*), where the entrapment of air within a series of surface textures facilitates oxygen exchange with the surrounding aqueous environment, as discussed in Section 2. The Riffle beetle (*Elmidae*) is an aquatic insect that is commonly found in streams and is well-documented to have a 'permanent' plastron, whereby, plastron regeneration is not necessary.[51,52] Translating this to synthetic materials, the entrapped air layer can give rise to many desirable properties/applications, for example, act as a protective barrier to inhibit the wetting of the substrate, which is desirable for the prevention of surface corrosion and/or bacterial adhesion and colonization (see Section 7.2).[49,53–55] In addition, the plastron can provide an environment with low friction drag and macroscopic slip, subsequently minimising the contact of an object moving through an aqueous medium (see Section 7.1).[40,56–58] Furthermore, the presence of a stable air-layer could be highly relevant to applications were underwater gas-consuming reactions and gas transportation take place (see Section 7.3).[59–64]

1.3.3 Critical pressure. When a superhydrophobic material is submerged underwater, the surface air-layer is exposed to external stimuli that can ultimately induce a wetting transition and therefore, degradation of the plastron. Hydrostatic pressure

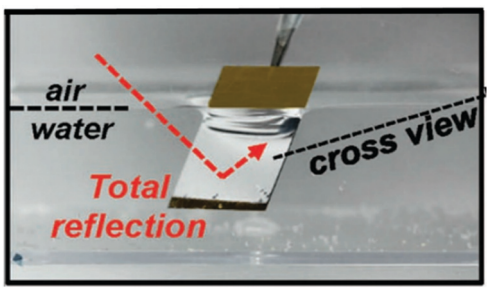

Fig. 4 Digital image of superhydrophobic ZnO nanorods submerged in water, highlighting the TIR of light (silvery surface) which occurs at the liquid–vapour interface due to the presence of the plastron. Reproduced with permission from ref. 50. Copyright (2015) NPG Asia Materials.

as a result of increased immersion depth, can quickly result in plastron destabilisation and is a major issue which can affect the plastron lifetime (discussed further in Section 4). As a greater depth is reached, an increased amount of hydrostatic pressure P_h is felt by the plastron, following:

$$P_h = \rho g h$$

where ρ is the density of water, g is the gravitational acceleration and h is the immersion depth. The pressure acts to agitate/move the trapped air from its equilibrium position, while enabling the penetration of water into the surface microstructure. Subsequently, increasing the internal pressure and decreasing the air volume. As higher depths are reached and therefore, a higher pressure felt by the meniscus, an increased rate of sagging will be observed. Researchers often characterise the stability of these surface by the pressure at which a wetting transition to the Wenzel state begins, which is known as the critical pressure. By balancing the forces acting on the plastron (Fig. 5), the critical pressure can be calculated using the general equation:[65]

$$P_{cap} + P_{air} = P_{amb} + P_h$$

where P_{cap} is capillary pressure, P_{air} is the pressure within the trapped air-layer and P_{amb} is the ambient pressure. This general formulation can be expanded to represent specific surfaces and take into consideration different features (*e.g.* pore volume, interface shape, pitch) and will vary greatly between surfaces due to the complexity and variation between pore shapes and sizes. A transition will begin when the hydrostatic pressure overcomes the opposing capillary pressure and pressure of the retained air-layer. The resistance against hydrostatic pressure by the compressed air and capillary pressure is the reason for the metastability of underwater superhydrophobic materials, with the total resistance being dependant on the size of pores and gas area fraction. For example, the generalized theory as discussed by Hemeda *et al.* shows that shallow pores have a higher critical pressure than deeper pores as they exhibit increased resistance against the hydrostatic pressure.[65] Compared with deeper pores, the ratio between the volume of air displaced as a result of sagging to the volume of the pore is much greater. This leads to higher compression pressures, which oppose the hydrostatic pressure, thereby stabilising the trapped air to a greater extent.

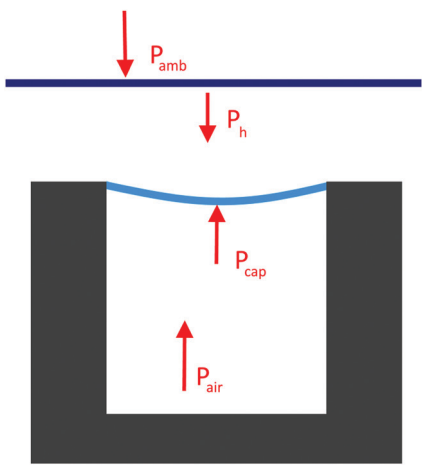

Fig. 5 Pressures acting on the air–water meniscus on a submerged superhydrophobic surface.

1.4 A potential target market: the marine sector

A target market where superhydrophobic coatings could be hugely effective is the marine sector.[38,66–68] If developed successfully, underwater superhydrophobic coatings could be the solution and driving force behind establishing 'greener' technologies within this sector, with many potential applicational areas, which are explored in detail in Section 7. Nonetheless, the market for underwater superhydrophobicity is yet to be effectively infiltrated due to long term underwater superhydrophobicity still being under premature investigation. The longevity of underwater synthetic superhydrophobic coatings is less well explored than that of generic superhydrophobic coatings, which primarily only face susceptibility to chemical and physical degradation. The additional instability of the plastron under dynamic conditions (hydrostatic pressure, contamination, oscillations, pressure fluctuations, *etc.*, see Section 4) can facilitate the displacement of the liquid–vapour interface, *via* the diffusion of gas into the surrounding aqueous environment (marked by a wetting state transition from the non-wetted Cassie–Baxter state to the wetted Wenzel state).[50,69–72] Furthermore, structural and chemical design features can also contribute to rapid plastron decay (see Section 2).[71,73] Hence, the exploration of natural designs is fundamental in understanding underwater superhydrophobicity and long term plastron stability.

1.5 Review summary

Within this review, the important considerations which must be taken into account when designing underwater superhydrophobic coatings/materials with long-term plastron stability will be discussed. This includes; advanced methods of characterizing the presence of interfacial air to visualize and monitor the stability of the plastron, environmental factors which can limit the plastron lifetime and accelerate the degradation process, a summary of the alternative design/fabrication processes used to produce high performance superhydrophobic surface coatings, and the current targeted underwater applications which the use of superhydrophobic materials are being investigated for within the literature. In doing so, we will draw comparisons between synthetic materials and those found in nature, highlighting the importance of specific design features, in order to achieve long-term underwater stability. Furthermore, the best performing, state-of-the-art superhydrophobic surface coatings which have been fabricated using innovative approaches will be reviewed.

2 Underwater stable systems from nature

The natural world is full of examples of plants and insects which have obvious uses of superhydrophobic functionalities (*e.g.* self-cleaning of Lotus leaves), as well as the ability to

maintain an air layer while underwater for different periods, depending on their needs.[71,74–78] As many insects have life cycles connected to water, their bodies have evolved accordingly to repel water, which is necessary for their breathing and additional functionality.[77] A thorough examination of surfaces found in nature reveals key design features required for air-layer stability underwater. Although environmental conditions (*e.g.* pressure) play a principal role in determining the air-layer stability (see Section 4), the surface structure/surface chemistry also largely contributes to plastron stability. This is demonstrated by the fact that some insects can retain air for only two days, while others can remain dry underwater for weeks or months.[77] Factors associated with surface localised features, such as; size, density, orientation and elasticity, were found to have major effects on protecting the air-layer.[71,77,79,80] Examples of well-established natural superhydrophobic surfaces, seen in plants and insects, are discussed below.

2.1 Water-bound insects

Many insects are known for their ability to 'walk on water', for example, the water spider (*Gerris remigis*). The ability to stand on the surface of the water is primarily attributed to the high surface tension, owed to the waxy coating often found on the legs of insects (Fig. 6a).[74,78] The spider's light bodyweight, accompanied by their long legs relative to their small bodies, make the spider's body carriable by buoyancy and curvature forces associated with water surface tension. In addition, the hydrophobic leg coating further hinders the possibility of breaking the surface tension and dipping inside the water, which supports the spider movement on the surface of water.[81–83] However, a closer examination of the legs of the water spider (*e.g. via* electron microscopy) reveals a surface structure consisting of micron-sized filaments that have a nano-grooved nature (Fig. 6b and c), resulting in a dual-scale roughness.[74,84] Studies have revealed that each leg provides a maximal supporting force of 152 dynes, equivalent to 15 times the weight of the entire body.[74] Another species of the water spider, *Argyroneta aquatica*, lives mostly underwater and only returns to the surface to regenerate its stores of oxygen.[75,85] The water spider's air supply is carried around its abdomen (Fig. 6d), where it takes air from the surface and brings it beneath where it makes a 'diving bell' that stores oxygen for the spider's respiration requirements.[85] The surface of its abdomen is covered with similar hydrophobic filaments, which repel water and allow for the retention of air (Fig. 6e–g).[75]

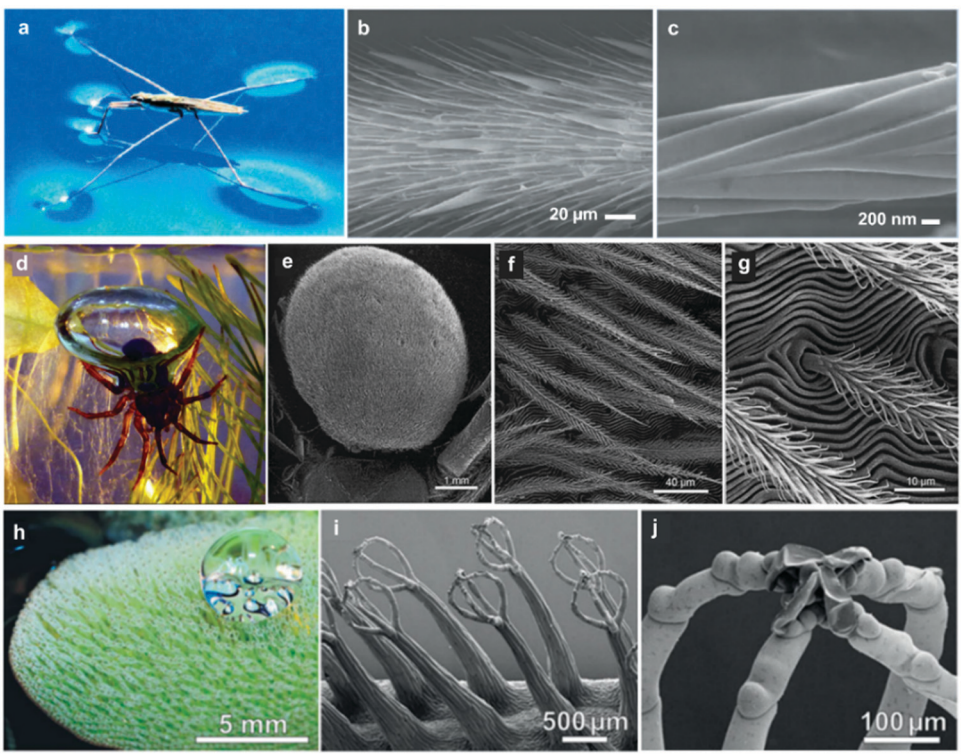

Fig. 6 Water-retention examples from nature. *Gerris remigis* (a) can stand on the water surface due to its highly structured superhydrophobic leg. SEM of the leg shows the micron-sized setae (b) covering the leg structure, and the nano-grooves (c) that each of these features contains. *Argyroneta aquatica* (d) forms a diving bell underwater for oxygen storage, and the abdomen structure (e–g) provides the necessary hydrophobicity to hold and transform air bubbles. The *Salvinia molesta* leaf surface (h) is covered with a dense layer of hairy features, which give the surface the superhydrophobic properties. These features, as visualized using SEM (i and j), consist of an egg-beater structure (i), with few dead cells landing on the top part (j). (a) Reproduced with permission from ref. 78. Copyright (2006) Wiley-VCH Verlag GmbH & Co. KGaA. (b and c) Reproduced with permission from ref. 74. Copyright (2004) Nature Publishing Group. (d) Reproduced with permission from ref. 85. Copyright (2011) The Company of Biologists Ltd. (e–g) Reproduced with permission from ref. 75. Copyright (2013) Neumann and Woermann; licensee Springer. (h–j) Reproduced with permission from ref. 71. Copyright (2010) Wiley-VCH Verlag GmbH & Co. KGaA.

The relationship between the morphological structure of the bodies of different air-retaining insects (*Galerucella nymphaea*, *Corixa punctata*, *Ilyocoris cimicoides*, *Gerris lacustris*, and *Notonecta glauca*) and the time they can remain submerged underwater, has been reported. Each selected insect was found to have specific air retention mechanisms dictated by the time they needed to stay submerged in water.[77] Structural-related differences were noticed, with some insects being covered with tall hairy features, referred to as 'setae', which allowed for high air-volume storage (Fig. 7a). On the other hand, smaller features called 'microtrichia' were found in other insects, which appeared to be more densely-packed (Fig. 7b).[77] When comparing the lifestyles of some of the insect species, it was found that *G. nymphaea* live on water lily leaves and rarely make contact with water, whereas *C. punctata* and *I. cimicoides* remain underwater but travel to the surface regularly to breathe.[77,86] All of these insects can retain an air layer for a maximum of two days. After examination of their surfaces, a similar morphology was detected, with a low density of setae ($\sim$1000–4000 structure per mm^2 and mean distance $\sim$10–30 μm) that are 20–35 μm in height.[77] In comparison, *G. lacustris* live mostly on the water surface and only dive for mating and egg-laying.[77,87,88] Subsequently, these were found to have a much higher air retention time, reaching that of two weeks. The higher stability of the plastron was linked to; (i) a higher density of setae ($\sim$10 000 mm^{-2}) and (ii) covering of shorter ($\sim$3–4 μm) and denser ($\sim 1 \times 10^6$ mm^{-2}, mean distance $\sim$0.6 μm) microtrichia.[77] Finally, *N. glauca*, which spend most of their life underwater and can preserve a stable air layer for over 120 days, was found to have a very dense layer ($\sim 2–7 \times 10^6$ mm^{-2}) of small microtrichia only.[77,89] Although larger setae features can hold a greater air volume, the smaller, yet densely-packed microtrichia, have been demonstrated to store air for a longer period of time (Fig. 7a and b). Hence, it can be concluded that large air volumes are generally of less importance for long-term air retention and that density is more impactful.[77] Typically, a feature density of 1–2 $\times 10^6$ mm^{-2} with a mean distance below 1 μm is considered to be the minimum requirement for long-time air retention.[77] However, having features of dual-size (large setae and smaller microtrichia), could provide double protection against wetting (Fig. 7c and d). In this arrangement, setae can hold a large volume of air under low water pressures, and as pressure starts to increase and the air-layer starts to deplete, microtrichia would still be able to preserve the dry surface beneath.[77]

Although both feature size and packing density are highly important, this is not the only surface property key to aiding long-term air-retention. It has been observed that the surface hair-like features are not completely verticle/perpendicular, but rather are angled towards the surface.[77] As setae have an inherent hydrophobic nature, this bending would increase the solid–water contact and decrease the air–water interface. Hence, providing greater support for the water, resulting in higher energy required for wetting the solid surface and displacing air, therefore stabilising the air layer.[77,79]

2.2 The Salvinia effect

Another example of natural long-term air-retention is found in a fern (*Salvinia molesta*), in which the leaf can sustain a stable air layer for several weeks during underwater submersion.[71,90] As this plant lives on the surface of the water, its air-retention ability becomes important when accidentally immersed in water to maintain its respiration and photosynthesis processes.[76] This has been attributed to the external layer of densely packed hair-like features on the leaf surface (Fig. 6h).[71,76,91,92] Each micro-scale feature has an egg-beater-like structure that is formed by four connected multicellular hairs (Fig. 6i and j), where the tip of each feature has four dead cells that are hydrophilic, on the otherwise intrinsically hydrophobic hair.[71] While the hydrophobic parts repel water to the surface and protect the air layer beneath, the hydrophilic tips get attracted towards the water. This attraction results in what is known as '*Salvinia* effect' or 'pinning effect', in which the hydrophilic tips remain attached to a water droplet when it is being pulled away, effectively pinning the air–water interface (Fig. 8).[71] This effect was found to be the reason for the high air-retention ability, as it minimizes local pressure fluctuations, and hence, increases the energy needed for the trapped air to be released.[71]

In addition to the distinguished feature structure and their hydrophilic-tip/hydrophobic body nature, the elasticity/flexibility of the hairs were found to play a role in stabilizing the air layer in *Salvinia* leaves. In regular surfaces, changes in local pressure lead to the displacement of the air layer and wetting of the surface. However, in surfaces with elastic features, the air–water interface can move in response to pressure fluctuations, making the air layer stable under higher pressures.[71,80]

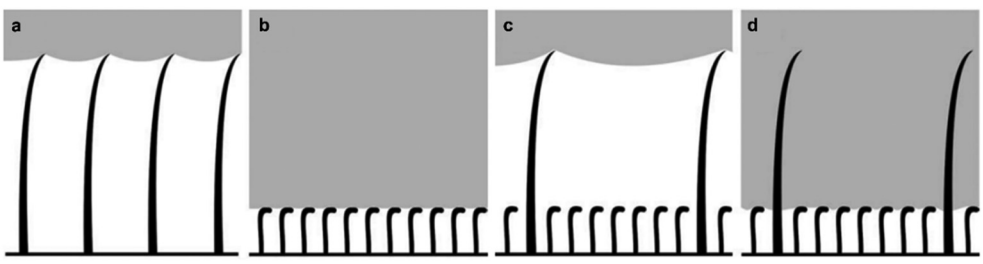

Fig. 7 Air layer stored underwater between setae (a) and microtrichia (b). While larger setae help to store a larger volume of air for a short time, densely-packed microtrichia store a smaller volume of air, but for longer periods. Some insects have a surface design that combines both setae and microtrichia (c and d). In this case, setae can store large air volumes at low water pressures (c). When the pressure goes higher, microtrichia form a second barrier against wetting (d). (a–d) Reproduced with permission from ref. 77. Copyright (2011) Wiley-VCH Verlag GmbH & Co. KGaA.

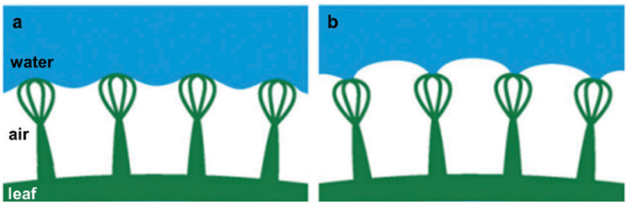

Fig. 8 Air-retention of a *Salvinia* leaf, (a) shows the repellence of water by the hydrophobic hairs, while (b) shows the 'pinning effect' of the hydrophilic tips when a water droplet is being pulled away from the surface. (a and b) Reproduced with permission from ref. 71. Copyright (2010) Wiley-VCH Verlag GmbH & Co. KGaA.

There are numerous examples where natural surfaces exhibit remarkable long-term superhydrophobic properties underwater, where an in-depth study of these surfaces has provided an insight into understanding the factors that contribute to plastron stability and longevity (including; feature size, density elasticity and chemical heterogeneity). These principles have been widely applied also in manufactured surfaces, as detailed in Section 5.

3 Air-layer characterization

Understanding the resilience of air plastrons is key to determine the surface effectiveness and longevity in many applications.[93,94] As plastron decay involves a Cassie-to-Wenzel transition, this concept has been utilized as an indication of air-layer stability. Straightforward visualisation of droplet-behaviour has been utilised for both of these major wetting models *via* WCA measurements.[93,95–97] Sole monitoring of WCAs can indicate a Cassie-to-Wenzel transition, as the surfaces in the Wenzel state generally have overall lower values.[95] In addition, WCA hysteresis, roll-off angles and bouncing behaviour have all been reported as key differentiators between the two wetting states.[36,95,98] In Cassie–Baxter wetting, water droplets show a relatively low adhesion to the surface due to the lower solid–liquid contact caused by the filled air pockets. As a result, droplet shape doesn't dramatically change during advancing/receding angles measurements, and the hysteresis values for such surfaces tend to be small.[98] Contrastingly, Wenzel wetting involves higher contact with the surface and less 'slipping' behaviour, resulting in a much higher hysteresis (reaching as high as 100°).[98] Following the same theory, roll-off angles are expected to be lower for 'slippery' Cassie surfaces, and bouncing behaviour could be demonstrated, in comparison with 'sticky' Wenzel wetting where droplet travel on surfaces is reduced.[95,98] The principles governing the droplet behaviour apply similarly to water jets impacted on the superhydrophobic surface with a defined angle. In this case, higher water repellency is linked with higher deflection angles of the water jet.[99,100]

Although these conventional characterisation methods have been widely reported, they suffer from many limitations when attempting to track wetting transitions. This is compounded by the uncertainty in defining the three-phase contact line when utilising WCA measurements.[101] In addition, some reports showed that measuring WCAs does not always reflect surface micro-wetting changes and that different wetting configurations can show the same WCA/hysteresis reading, which makes accurate tracking of plastron decay challenging.[93,102–104] As a way to directly visualize the small-scale wetting, methods such as cryogenic focused ion beam/scanning electron microscopy (cryo-FIB-SEM) have been reported.[105] Although such techniques can give an accurate visualization of plastron degradation, they require advanced technology and difficult preparation/operation conditions, in addition to the inability of dynamic tracking of wetting transitions.[105]

In this section, we give an overview of some methods that have been reported for characterizing air-layer stability. These methods are categorised depending on their operation principle into the following measurements: (i) optical, (ii) force, (iii) acoustic and (iv) electrochemical methods. As most of these techniques are not directly designed for air layer monitoring, the section highlights how they have been adapted to give information on wetting behaviour.

3.1 Optical methods

Light microscopy has been widely reported in the measurement of air retention in superhydrophobic surfaces. Optical methods enable visualization of plastrons, as well as the real-time tracking of their decay. This allows for understanding the effect of immersion time on the lifetime of the air layer.

3.1.1 Reflection measurement. Trapped air on a submerged surface can be easily verified by its shiny mirror-like appearance, which is a result of the TIR phenomena (Fig. 9a).[106]

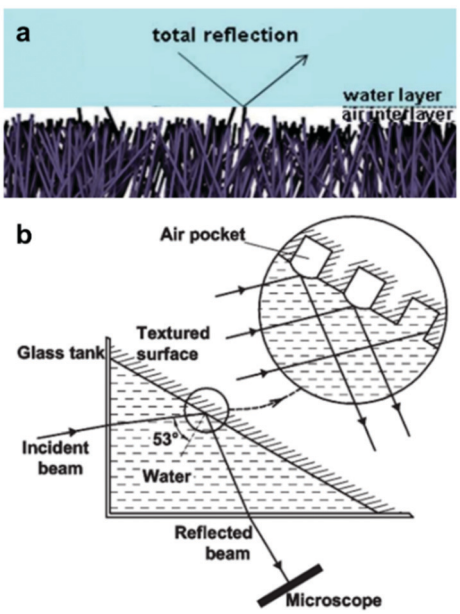

Fig. 9 (a) Illustrates the total internal reflection phenomena. (b) A schematic of the setup used to measure reflection intensity. An incident beam gets reflected off the air-layer trapped in an examined surface, and collected/analysed by a microscope. (a) Reproduced with permission from ref. 106. Copyright (2012) The Royal Society of Chemistry). (b) Reproduced with permission from ref. 109. Copyright (2009) American Chemical Society.

When light travels through two media with different refractive indices, the light gets refracted. However, if the incident beam exceeds a certain critical angle while travelling to a lower refractive index medium, the beam gets reflected, causing the silvery look of the surface (Fig. 4).[107] In this case for light travelling from water to air, the critical angle is 48.75°.[108] The intensity of the reflected beam could be tracked and used to visualize the plastron-decay process. Fig. 9b shows the setup used for this purpose. The examined surface is placed in a water tank, where a beam source is adjusted to make contact with the surface at a specific angle to promote reflection, and then the light is collected by a detector/microscope which is positioned on the other side.[109] Surface entrapped air appears as a bright spot, while water-filled pockets do not reflect the beam.[109] In this way, monitoring air stability over time can be quantitatively determined. Both the mapping of bright/dark spots and the tracking of total reflection against time have been used for visualizing the decay process.[47,110] This setup also allows for testing surfaces under different conditions with simple adjustments, including; changing immersion depth,[73,106,111] applying higher hydrostatic pressures[112] and/or examining the air-stability underflow (discussed in Section 4).[47]

3.1.2 Confocal microscopy. Laser scanning confocal microscopy (LSCM) has been reported widely for assessing surface wetting.[101] Similar reflection behaviour of the laser beam could be observed and utilized for this technique (Fig. 10a). Utilising a similar principle as illustrated above, the reflection intensity of the water–air interface is higher than that of the water–solid interface.[113] This generates bright and dark spots, respectively, from these interfaces. Hence, for a surface with a retained air layer, a bright line could be observed where the air–water interface is located.[113–115] The movement or disappearance of this reflection with time indicates the areas of the sample where plastron-failure occurs.[113,115] The microscope is placed above a water-filled tank containing the examined sample (imaging setup is shown in Fig. 10b). A two-dimensional intensity profile (Fig. 10b) was generated from this setup while examining a nanofur sample after a submersion period of 7 days.[116] The image indicates the high air retention ability of this sample.[116] Similar to the previous technique, live-tracking of the plastrons decay could be performed.[73,113,116] The setup also allows testing samples at higher pressures, which Vüller *et al.* have reported.[115]

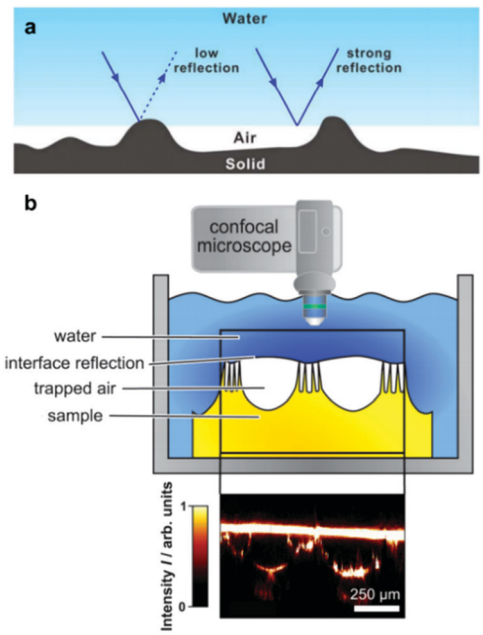

Fig. 10 (a) A schematic for the reflection of the laser beam and how it is affected by changing the reflection interface. (b) (above) A schematic of the setup used for the air-layer assessment using LSCM, and (below) a vertical intensity profile of a nanofur sample placed underwater for 7 days. (a) Reproduced with permission from ref. 113. Copyright (2010) Wiley-VCH Verlag GmbH & Co. KGaA. (b) Reproduced with permission from ref. 116. Copyright (2014) Wiley-VCH Verlag GmbH & Co. KGaA.

3.2 Force methods

The following methods depend on force measurement to provide information on air stability. The techniques in this section allow for the estimation of surface wetting and air retention conditions, including water penetration depth and volume of the air retained.

3.2.1 Atomic force microscopy. Atomic force microscopy (AFM) has been reported for accurate examination of numerous surfaces, including delicate biological systems and liquid interfaces.[117] AFM relies upon nanoscaled probes that usually make contact with the analysis surface/interface, and owing to its high precision, it can provide information on nanostructured surfaces.[117] AFM has been utilized for examining air–water interfaces for surfaces submerged underwater by many researchers (Fig. 11a). Both tapping mode[117,118] and non-contact mode[119,120] were applied for this purpose. Moosmann *et al.* reported the examination of a micro-structured epoxy surface, both in air and underwater, which enabled estimating the water penetration depth.[118]

For the previous light-based techniques, the visualization was limited to micro-scale structures, as the resolution of optical microscopy hinders observing smaller features.[117] In contrast, AFM can be beneficial in getting details on the nano-scale, which Elbourne *et al.* utilized to map the surface of a Si-nanopillar textured sample.[117] Fig. 11b shows the cross-section height profile for the sample, which highlights two things: the ability to distinguish nanoscale features and the penetration depth of water into the surface. Fig. 11c and d shows how the height profile has been constructed. The surface was mapped in air and water, and the difference in height detected by the cantilever was used to extract information about surface wettability.[117]

3.2.2 Buoyancy measurement. In contrast to the previous methods aimed to map the surface and visualize the air layer, buoyancy measurements were developed to measure the volume of the retained air.[121] This is achieved by measuring the buoyancy force. In the setup, a force sensor is connected to a metal needle, and the measurement sample is suspended from the needle by nylon strings (Fig. 12).[121] The test is then performed twice; before and after surface wetting (the removal of trapped air). The difference in buoyancy force provides the ability to calculate the volume of the air layer.[121] The reported setup can be used to measure air volumes up to 900 µL, with a

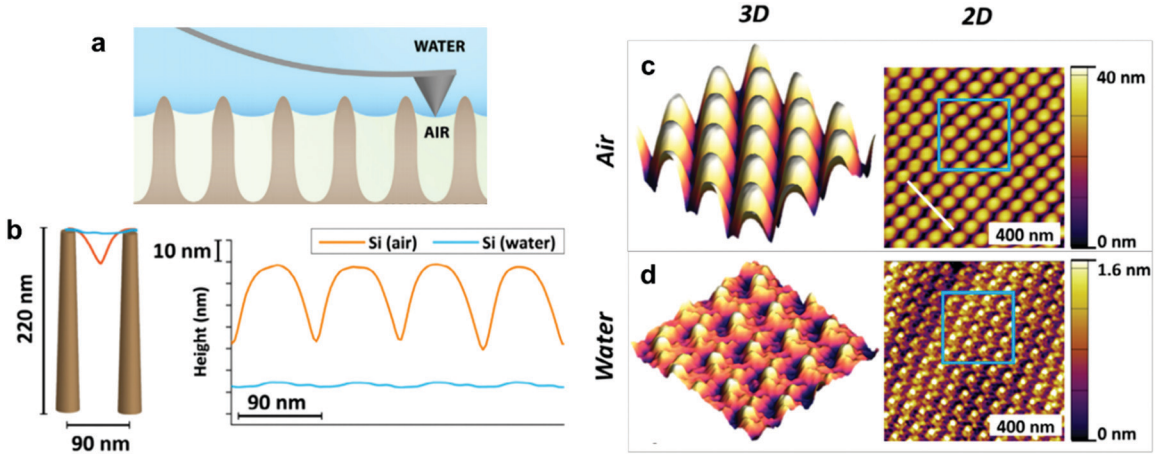

Fig. 11 (a) A schematic of measuring the penetration depth using tapping mode in AFM. (b) Shows the cross-section high profile measured by AFM for a sample textured with Si nanopillars, both in air and in water, showing the penetration depth. (c and d) Show the images from which (b) has been constructed. (c) Shows the 3D (left) and 2D (right) images of the nanopillars sample placed in the air, while (d) shows the images for the sample placed underwater. (a–d) Reproduced with permission from ref. 117. Copyright (2018) Elsevier Inc.

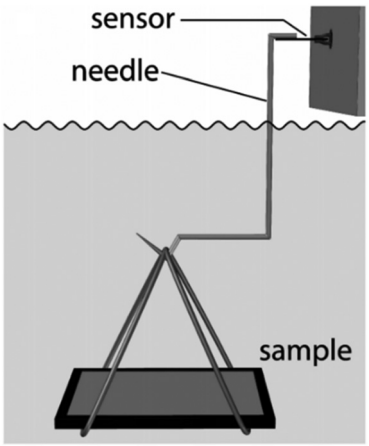

Fig. 12 The setup used for buoyancy measurement. Reproduced with permission from ref. 121. Copyright (2014) Mayser *et al.*; licensee Beilstein-Institut.

0.1 μL precision, and was utilized to measure the air volume stored by the *Salvinia* plant species. It was found that they can hold up to 1 L m^{-2} of air while placed underwater.[121]

3.3 Acoustic methods

The following methods were reported for the detection of different wetting states and their transitions by applying acoustic waves. These methods, although lacking the visual illustration of plastron decay, allow real-time tracking of the average surface wettability changes, which have subsequently provided an understanding of surface properties and air-retention abilities.

3.3.1 Quartz crystal microbalance. Quartz Crystal Microbalance (QCM) is an acoustic-wave device with high sensitivity to changes in mass, and therefore, enables the detection of minute mass gain or losses associated with interfacial processes like adsorption/desorption.[101,122] The device consists of a vibrating quartz crystal resonator, with a gold electrode laying above it (Fig. 13a). Small changes occur on the electrode surface causing a frequency-shift in the generated acoustic waves, which are analyzed and used to draw conclusions about surface processes.[101] Owning to its high sensitivity and accuracy, the technique has been applied in detecting wetting transitions.[105,122–124] Wave propagation into the liquid forces an amplitude decay, therefore, higher liquid penetrations lead to lower frequency shifts.[101] This mechanism allows detection of Cassie, Wenzel and intermediate states with high differentiation ability, albeit as a bulk measurement across the entire material.[105] Roach *et al.* highlighted the effect of surface chemistry, structural geometry, and liquid viscosity on the frequency shifts detected and proved the ability to identify different wetting configurations in these cases.[123] Wang *et al.* used droplet-freezing to image surfaces with cryo-FIB-SEM and visualize different wetting states, which agreed with the results obtained by QCM.[105]

3.3.2 Ultrasound. Another form of acoustic-based methods was reported by Saad *et al.* that employed ultrasound waves to track wetting behaviour.[102] Fig. 13b illustrates the setup used in their experiment. A transducer is integrated into the back-side of the examined surface, producing an ultrasound wave that propagates and reflects from the above surface.[93,101,102] Similar to the principle described in QCM, the reflection coefficient (r^*) decreases for waves reflected at solid–water interfaces (Wenzel), compared to those reflected at solid–air interfaces (Cassie).[93] This is explained by the decrease in the amplitude of waves reflected from solid–water interfaces.[101] Typically, for a textured surface with a bottom (exposed to air in Cassie and water in Wenzel) and a top (exposed to water in both cases) solid portions, the normalized coefficient $\left(r^*_{\text{bottom}}\right)$ goes from 1.00 (in air and Cassie state) to 0.86 (during Wenzel wetting).[93] For $\left(r^*_{\text{top}}\right)$, it decreases to 0.86 when the surface is first wetted, and then further to 0.75 during Wenzel wetting, which could be explained by the textures being surrounded with water from the sides.[93] In this way, tracking wetting states and transitions can be achieved.

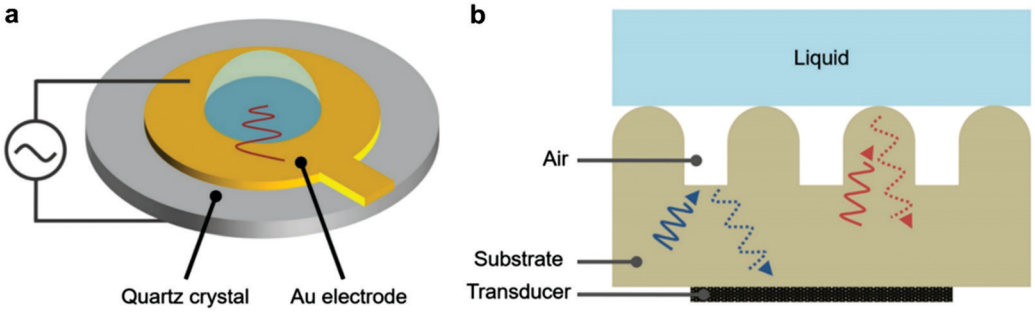

Fig. 13 (a) A schematic for the quartz crystal microbalance. (b) A schematic for the operation principle of detecting wetting states by analysing reflected ultrasound waves. (a and b) Reproduced with permission from ref. 101. Copyright (2019) Wiley-VCH Verlag GmbH & Co. KGaA.

3.4 Electrochemical-based methods

3.4.1 Electrochemical impedance spectroscopy. In this technique, electrochemical impedance, which could be defined as the system resistance against the interaction with ions in solution, is being utilized to characterize surface wetting.[101,125] In general, the presence of air gaps between the electrolyte solution and the surface increases the impedance, as ion mobility is being hindered.[125] Accordingly, surfaces in Cassie wetting state would show high impedance. As the water penetration increases, impedance goes lower until reaching a minimum during Wenzel wetting.[101] Tuberquia *et al.* reported the analysis of polymer films wettability using electrochemical impedance spectroscopy and established a mechanism for wetting transition.[125,126] They highlighted three main steps that lead to Cassie–Wenzel transition: (i) a 'nucleation' step, where small areas beneath air–liquid interface adopt the Wenzel state and get wetted, (ii) a 'propagation' step in which the Wenzel state becomes more dominant and larger air volumes are being displaced, and (iii) a 'termination' step where the air layer is compacted into small isolated air pockets which are located randomly on the surface, with no effective retention ability.[125] The technique represents a powerful tool for real-time wetting characterisation.

This section highlights many different methods for air layer analysis. The choice of a specific technique is dependent on the type of analysis desired (*i.e.* precise mapping of the air–water interface or an estimation of the amount of air present), and the compatibility with any external stimuli applied (*e.g.* submersion pressure or water flow). These two factors (the type of analysis and compatibility) must be considered in conjunction with the tolerance for the complexity of any research project. This multi-faceted consideration of analysis techniques has resulted in the diverse array of methods presented in this section.

4 Environmental factors affecting plastrons' stability

Upon immersion, plastrons are exposed to several factors that can promote the transition from a Cassie–Baxter to a Wenzel state, in addition to the chemical and physical degradation that would usually occur when not submerged in water.[91] Underwater degradation can occur under increased hydrostatic pressure, as a result of increased depth or fluid shear forces, in addition to the diffusion of air and other external stimuli. These factors can result in the air–water interface being pushed toward the surface as air is lost from the system. Once the meniscus reaches the bottom of a surface feature, such as a pore, the surface is said to have undergone a transition to a wetted state. These environmental factors have resultantly been utilised to assess the air layer stability, both examining air layer degradation and full wetting transitions.

4.1 Pressure

Hydrostatic pressure as a result of increased depth or fluid shear forces is one of the causes of plastron instability, with some surfaces only requiring a small change in pressure to induce a transition.[72,91] Over the past decade, a range of experimental and theoretical investigations have focused on understanding the effects of such pressures and the wetting transitions they cause. These studies utilise two main varieties of materials; those with random surface features, and surfaces with ordered/repeating designs. Generally, initial studies in this area focus on the use of indirect optical techniques, in which a wetting transition can be observed by recording intensity as a function of pressure. As a result, any wetting transition occurring as a direct consequence of increased water pressure can be observed without completely resolving the liquid–air interface (Section 3.1).[91] For example, Lei *et al.* submerged polydimethylsiloxane (PDMS) treated transmission gratings within a fluidic chamber, allowing for the observation of diffraction patterns when a laser was passed through the grating.[127] As the pressure within the chamber increased, the intensity of the diffraction pattern would decrease (Fig. 14). This results from water replacing air within the grating and the refractive index of PDMS (1.41) being similar to that of water (1.33).

By gradually decreasing the applied pressure, the gratings were observed to recover their plastrons. A full recovery of the plastron was achieved up to a maximum applied pressure of 50 mbar. However, as this maximum value increased the ability to recover decreased, showing a partial recovery at a maximum pressure of 60 mbar and no recovery when a 100 mbar pressure was applied.[112]

More commonly, methods utilising the reflective properties of the plastron are used to monitor the transition. Samaha *et al.* demonstrated the effects of increased hydrostatic pressure on

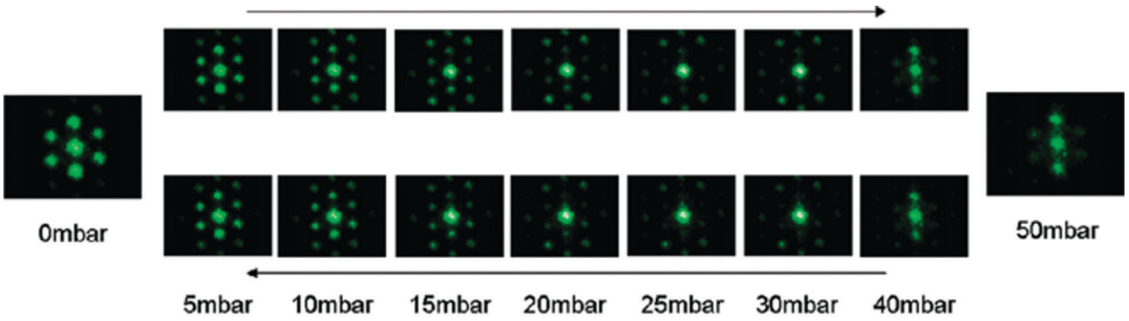

Fig. 14 Variation of laser diffraction patterns up to a maximum applied pressure of 50 mbar. A decrease in pattern intensity indicates a decrease in trapped air. Reversing the pressure leads to an increased intensity indicating a recoverable transition. Reproduced with permission from ref. 127. Copyright (2009) American Chemical Society.

randomly microstructured silicon dioxide-based aerogels.[112] Further still, the effect that gas area fraction (GAF, which relates to $1 - \phi_S$ in Section 1) had on plastron stability was investigated. The rate of decrease in light intensity as pressure increased was greater in surfaces with larger GAFs, indicating a higher instability to hydrostatic pressure. In addition, the terminal pressure (*i.e.* the pressure in which a complete loss of air has occurred) was recorded. For large GAFs, a terminal pressure of $\sim$100 kPa was reached, this increased to $\sim$600 kPa (equivalent to $\sim$60 m underwater depth) when smaller particles were used. Lee *et al.*[106] recorded greyscale images of their submerged $W_{18}O_{49}$ nanowire arrayed superhydrophobic structures. This allowed a threshold to be applied from which the plastron intensity could be recorded as the ratio of white (dry) to black (wet) pixels. The tungsten oxide nanowires were produced by thermal evaporation and chemical modification with alkyltrichlorosilanes to achieve surfaces with varying surface energies. To understand the effects of hydrostatic pressure on the plastrons stability, the wires were submerged underwater. At all depths, the air layer remained intact for a period before rapidly decaying. As shown in Fig. 15, as the immersion depth increased, the stability of the superhydrophobic state dramatically decreased due to an increased pressure deforming the plastron interface.

To understand the effects surface energy has on plastron stability, samples were kept at a 20 cm submersion depth. Here, it was shown that with increasing surface energy (with a decreased carbon number (CN) on the alkyltrichlorosilane), the lifetime of the plastron rapidly decreased. That is to say, higher stability was achieved when lower surface energy (higher CN) material was used. As the surface energy increases, the contact angle of the surface decreases. A lower contact angle will give a concave air–water interface and, as a result, the Laplace pressure induced by capillary forces will be exerted downwards, aiding the hydrostatic pressure.[128] In contrast, higher WCAs lead to a convex interface and an upwards Laplace pressure, stabilising the plastron.

Along with increased depth, fluid shear forces (*e.g.* caused by water flow over the material) increase the pressure exerted on a surface. Samaha *et al.* investigated how increased flow velocities affected the air-layer on electrospun superhydrophobic polystyrene fibres.[129] By creating a water jet on the sample inside a pressure vessel, as shown in Fig. 16, a simulation of a moving submersible could be achieved. The intensity of reflected light was monitored

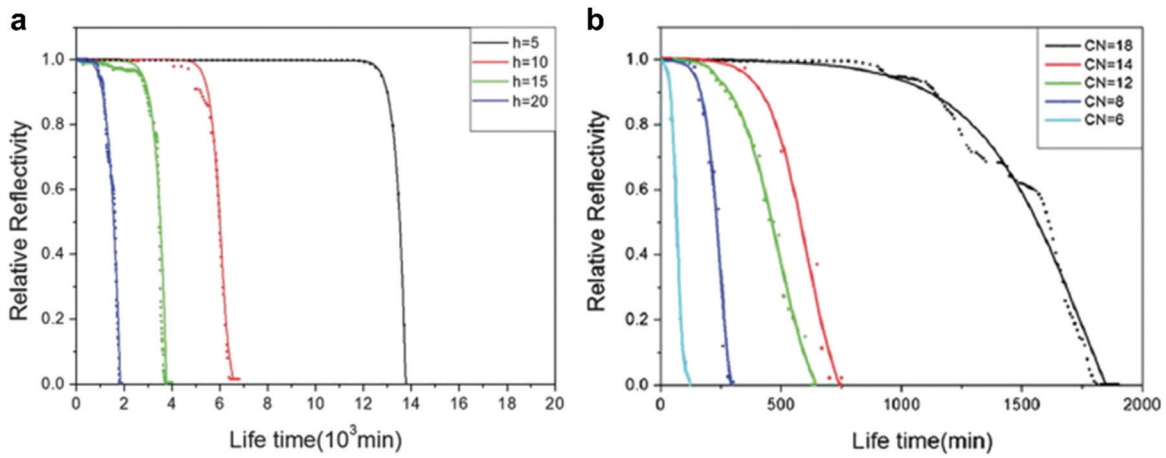

Fig. 15 (a) Relative reflectivity for octyltrichlorosilane-modified W18O49 nanowire as a function of time at different immersion depths (5, 10, 15 and 20 cm). The intensity was recorded as the ratio between dark (wet) and light (dry) spots on greyscale images which were recorded at 20 min intervals. (b) Relative reflectivity of alkyltrichloromodified-modified nanowires at 20 cm submersion. Carbon numbers (CN) were increased to vary surface energy. CN = 6 (hexyltrichlorosilane), CN = 8 (octyltrichlorosilane), CN = 12 (dodecyltrichlorosilane), CN = 14 (tetradecyltrichlorosilane), and CN = 18 (octadecyltrichlorosilane). (a and b) Reproduced with permission from ref. 106. Copyright (2012) The Royal Society of Chemistry.

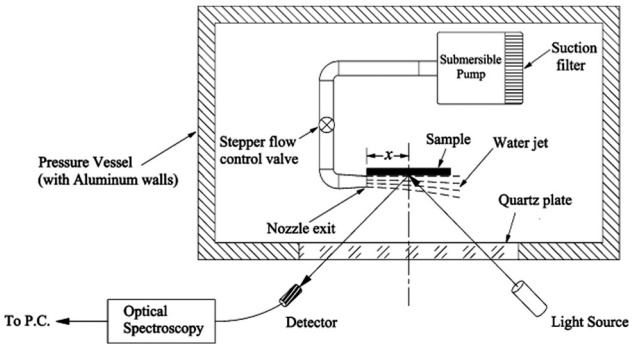

Fig. 16 Schematic illustration of the setup used to investigate the effect of water movement on the longevity of the air layer under flow conditions. Reproduced with permission from ref. 129. Copyright (2012) American Chemical Society.

as a function of jet Reynolds number and time. The Reynolds number is a dimensionless number representing the flow of fluid, where high Reynolds numbers indicate turbulent flows and low Reynolds numbers are laminar flows. Their results similarly showed that an increased flow rate led to the greater dissolution of trapped air. For static conditions, a level of trapped air could be maintained upwards of 70 hours, however, when the jet flow was applied this greatly reduced to ~15 hours.

Vüllers *et al.* also studied the dynamic wetting conditions on their superhydrophobic surfaces.[70] Varying surface structures, topographies and materials were used including three densities of polycarbonate nanofur, a hierarchical wrinkled Teflon amorphous fluoropolymer (AF) surface and an ordered polytetrafluoroethylene (PTFE) pillared array. By attaching surfaces to a dip-coater, the velocity could be ranged from 20 mm min^{-1} to 200 mm min^{-1}. For high density (HD) nanofur, after a velocity of 50 mm min^{-1} is reached, 8% of the surface had been wetted. Increased velocities after this point showed no further wetting. As the densities of fur decreased, the wetted area increased with medium-density (MD) fur and low density (LD) fur, showing 63% and 88% wetting at 200 mm min^{-1}, respectively. Additionally, MD and LD nanofur showed an accelerated rate of wetting compared to HD (Fig. 17). This was a result of increased pitch between fur and, therefore, less support to the plastron interface. This lead to increased sagging and ultimately greater wetting of the surface. In comparison, the hierarchical structure of the Teflon wrinkles was able to remain completely intact at all immersion speeds, and the PTFE showed 63% wetting at 200 mm min^{-1}.

The random nature of the Teflon surface leads to cavities and barriers which help protect against shear forces as opposed to the open-air layer on the ordered surface. Comparing nanofur to the pillared array, the polycarbonate of the nanofur has higher surface energy than PTFE, allowing for easier pinning to feature tips and therefore increased stability. Based on their findings, a list of topographical features was recognised for increased stability: (i) hierarchical topography; (ii) high-density surface features; (iii) minimal water-solid contact area; (iv) nanoscale feature size; and (v) reentrant geometries. Each surface also highlighted how an increased flow rate resulted in a decreased plastron lifetime due to enhanced diffusion of trapped air. It should be noted that the stability promoting features relate directly to the specific material investigated in this report, a more general summary is provided at the end of this review.

Another indirect method for understanding the effects of pressure on plastron stability is to monitor the effectiveness of drag-reduction or corrosion resistance. These effects are a direct result of trapped air and, therefore, a reduction in either would indicate air loss. Ou *et al.* used superhydrophobic aluminium samples immersed at varying depths in aqueous NaCl to observe the corrosion behaviour.[130] The results indicated that, as hydrostatic pressure increased, the degradation of superhydrophobicity increased and more severe corrosion was observed for non-oxidised samples. The air layer acting as a protective barrier was lost at increased pressures allowing corrosive species, such as Cl^- ions, to reach the surface. Interestingly, oxidised aluminium surfaces showed an increased level of corrosion between 1 kPa and 15 kPa of hydrostatic pressure, but an even greater amount at 0 kPa of hydrostatic pressure. This is thought to be due to the

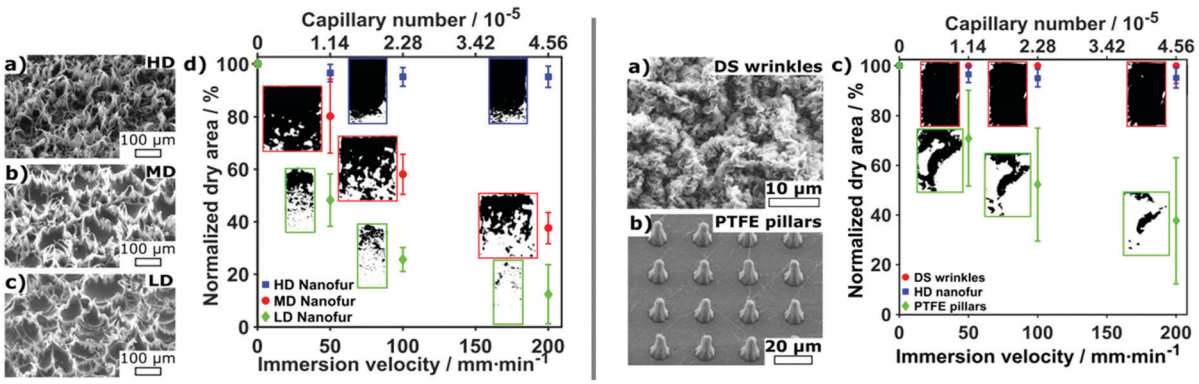

Fig. 17 SEM images and dynamic plastron stability at different velocities. Averaged dry area as a function of immersion speed in Milli-Q water where dark and white areas represent dry and wetted areas respectively. Error bars show respective standard deviations for at least n = 3 measurements. (left) LD = low density, MD = medium density and HD = high density nanofur. Results indicated that a lower hair density and higher pitch resulted in a less stable air layer. (right) Wrinkled and PTFE pillared array structures. Reproduced with permission from ref. 70. Copyright (2019) Vüllers *et al.*

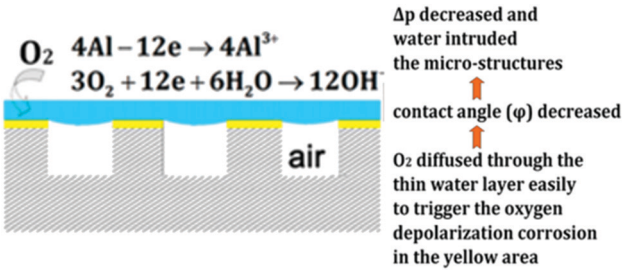

Fig. 18 Schematic of the oxygen corrosion of the aluminium substrate and proposed corrosion mechanism. Reproduced with permission from ref. 130. Copyright (2018) American Chemical Society.

reduction of the sample by oxygen. The proposed mechanism of which is shown in Fig. 18. As only a thin layer of the aqueous solution was present, oxygen from the air could easily diffuse through to the metal substrate. In comparison, at higher fluid pressures, a greater volume of water separated the air and surface, and so oxygen could not diffuse through easily to corrode the aluminium.

An alternative approach was reported which utilises theoretical study and calculations to investigate how an increase in hydrostatic pressure can affect the air layer of various surfaces. Emami *et al.* carried out a range of studies on randomly structured surfaces, submerged in water while applying hydrostatic pressure.[131] The loss of superhydrophobicity was then calculated. To do so, a partial differential equation was derived from the Young–Laplace equation and solved to obtain the shape of the air–water interface. The results showed that as the pressure increased, the meniscus depth increased as the interface sagged into the surface (Fig. 19).

For post structures, it was noted that the critical pressure for randomly distributed samples was much lower than ordered posts. Similarly for fibrous coatings, a lower critical pressure was seen when fibres were randomly orientated as opposed to their orthogonal counterparts. Randomly structured surfaces can often show a dramatic increase in pitch and as such fewer posts support and pin the plastron in place. This means there is less resistance against hydrostatic pressure and such the transition of the interface occurs much more readily.

As discussed in Section 3.1.2, confocal microscopy is a useful tool that allows for observation of the air–water interface, which gives insight into the mechanism of transition and the existence of metastable states. The metastability results from the compressibility of trapped air, resisting the push of water into the surface by hydrostatic pressure.[73,132] The wetting transition has been observed (both mathematically and experimentally) to follow a sagging transition in which the meniscus remains pinned to the corners of surface features but the contact angle increases.[65,91,133,134] From this point, the angle will increase until a critical point is reached, after which the interface de-pins from the edges and slides down the surface topography. Using LSCM, Lv *et al.* observed the transition from the Cassie–Baxter to Wenzel state, including de-pinned metastable states (Fig. 20).[132] The transition was carried out for cylindrical micropores etched into a silicon substrate coated with a self-assembled monolayer of fluorosilanes. At lower pressures, the surface was able to stabilise against the hydrostatic pressure, remaining in a pinned Cassie–Baxter state. As this pressure increased, however, the interface de-pins from the micro-posts and slides into the structures. Remaining

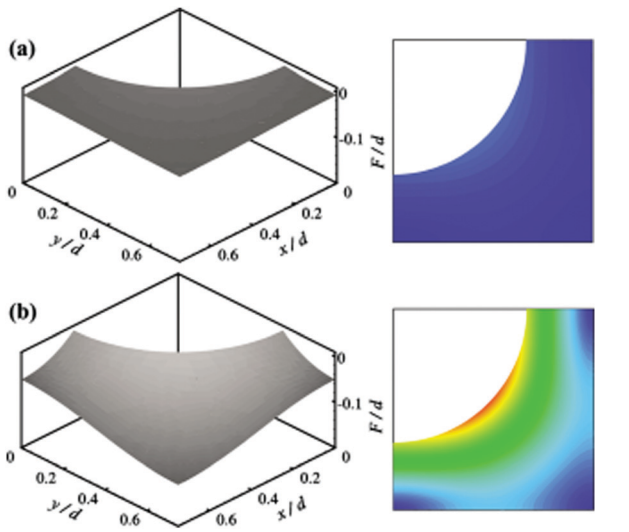

Fig. 19 Calculated air–water interface and gradient contour for ordered identical posts. (a) 1000 Pa and (b) 7000 Pa. Surface function, F, and the coordinates x and y are normalised with the post diameter. As the hydrostatic pressure increased the meniscus curves down due to the pressure. (a and b) Reproduced with permission from ref. 131. Copyright (2011) American Institute of Physics.

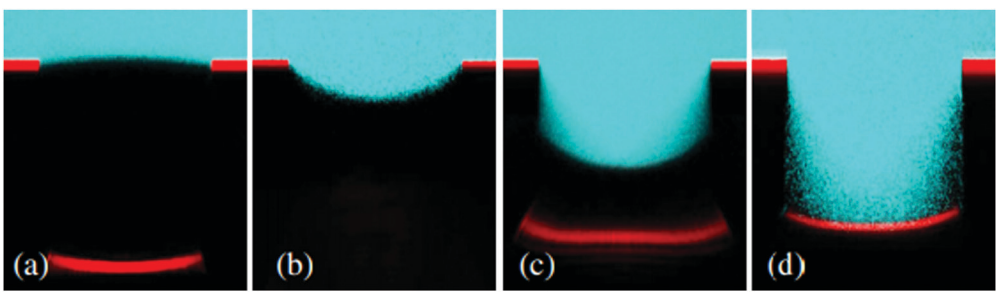

Fig. 20 LSCM images showing the air–water interface 5 minutes after immersion at different pressures (a–c); (a) Cassie–Baxter (0 kPa), (b) pinned metastable Cassie–Baxter (14 kPa), (c) depinned metastable state (50 kPa), and (d) shows the interface 15 minutes under 50 kPa where full wetting has been reached. (a–d) Reproduced with permission from ref. 132. Copyright (2014) American Physical Society.

at this pressure eventually led to a full transition to the Wenzel state.

4.2 Diffusion of air

Even if a surface is designed to withstand high hydrostatic pressure or exists in a metastable state, the longevity of the air layer is a key consideration.[91,135] When air is trapped along the surface of a submerged superhydrophobic structure, it is separated from ambient conditions so that it exists in a closed state. This means in addition to the mechanical equilibrium, a new chemical equilibrium is established controlling the overall stability of the plastron.[136] This chemical equilibrium is governed by the exchange of gases between the plastron and surrounding water and, therefore, the rate is overwhelmingly controlled by the concentration gradient across the interface. Despite this, even in fully gas saturated water, gas within trapped air bubbles will still diffuse out over time, due to surface tension and compression, resulting from hydrostatic pressure as shown by Epstein and Plesset.[137] Other factors affecting the diffusion rate include; pressure, fluid flow, temperature and in the case of surface plastrons, pinning effects to surface features. The overall time for loss of plastron air as a result of diffusion is, therefore, determined by the volume of trapped gas and the diffusion rate.

Bobji *et al.* investigated the stability of trapped air on several superhydrophobic surfaces by leaving the samples submerged in air-saturated water for a minimum of 2 days.[109] Three of the surfaces were regularly arrayed silicon structures consisting of pillars, ridges or holes prepared by photoetching whilst the last was a randomly arrayed aluminium surface. A self-assembled layer of 1*H*,1*H*,2*H*,2*H*-perfluorooctyl trichlorosilane rendered the samples hydrophobic. An optical microscope was used to observe the reflective properties of the sample (air pockets appearing as bright spots) and monitor plastron deterioration. Of the surfaces, the pillared surface trapped the largest amount of air and hence took the longest to completely transition to a Wenzel wetting state.

As the number of bright spots decreased, it can be concluded that the interface has either travelled deep enough into pores that the microscope cannot observe the reflected light or that complete wetting has been achieved. Fig. 21 shows the results obtained for the hole arrayed structure and demonstrates how the rate of diffusion started slow, increasing to a maximum rate between 15–20 minutes into submersion before decreasing back to a slower rate. As air bubbles begin to diffuse from the pores, the local concentration of air is altered, affecting the concentration gradient and hence leading to an increased rate of diffusion. For all samples despite the difference in topography, the air pockets decreased over time highlighting the instability of the plastron due to diffusion of air.

Poetes *et al.* similarly used the reflection of light and confocal microscopy to study the decay of plastrons over time due to diffusion.[73] The submerged material was a superhydrophobic Teflon surface with micrometre-sized protrusions separated by <100 nm secondary features. The images in Fig. 22 shows how the plastron began as a continuous air layer that is ~ 70 μm thick (Fig. 22d) and supported on the micrometre-sized features.

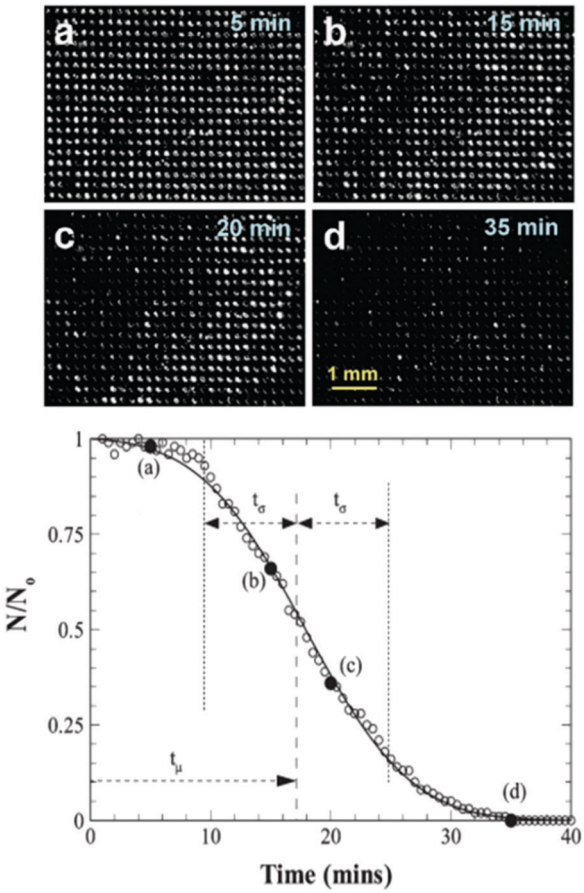

Fig. 21 (top) Microscope images of air pockets variation with time on hole arrayed surface. The reduction of holes as time passes indicated the transition of the interface deeper into the holes. (bottom) Variation of the normalised number of bright holes indicating trapped air as a result of total internal reflection, with time for arrayed hole structure. N_0 represents the total number of bright holes at the start of the experiment, 522. Solid circles (×) between (a–d) represent the time at which photos were taken. Reproduced with permission from ref. 109. Copyright (2009) American Chemical Society.

As time passed, the plastron began to thin, decreasing to ~ 50 μm after an hour (Fig. 22e). As the air diffused, the plastron came in contact with more surface features and began to separate into a collection of smaller bubbles distributed across the surface (Fig. 22f).

Diffusion rates are further increased with elevated hydrostatic pressure or liquid flow. Hokmabad *et al.* observed the effect that an increased Reynolds number had on air dissolution.[47] The surfaces consisted of random spray-coated textures created with a commercially available superhydrophobic coating (NeverWet). The lifetime was estimated as the time over which the intensity of the reflected light decreased to zero. As the surfaces were subjected to flows with higher Reynolds numbers, the lifetime of the air layers decreased by up to $\sim 50\%$. The reason for increased rates of air loss is suspected to be from the mass transfer mechanism changing from a diffusion regime to forced convection caused by fluid shear stress increasing by up to 75% (Fig. 23).

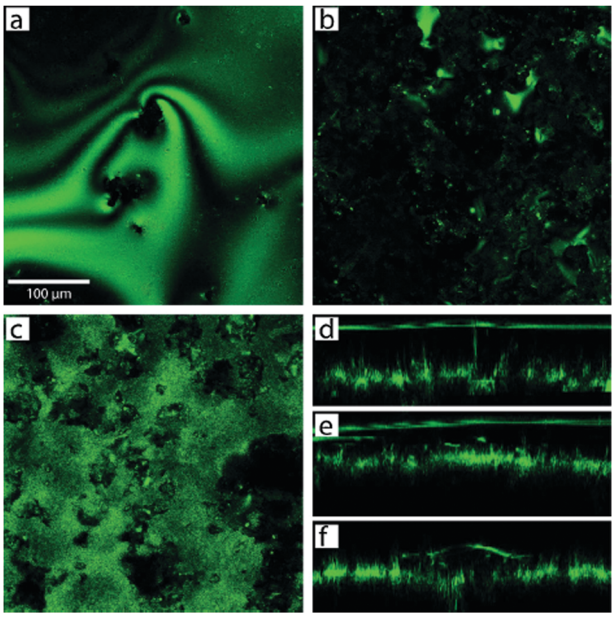

Fig. 22 Confocal microscopy images and cross-sections showing the decay of plastron with time. Images taken at different immersion times (a) 15 min, showing a complete plastron and (b) 30 min, showing localised air bubbles. (c) In-place slice of the plastron at the air–water interface after 5 days highlighting the increased number of contact points between water and surface features. Cross-sections are shown (d–f) where (d) shows the plastron immediately after immersion, (e) after 1 h, and (f) shows how the plastron decayed into spherical cup-shaped bubbles pinned to the surface after longer periods. (a–f) Reproduced with permission from ref. 73. Copyright (2010) American Physical Society.

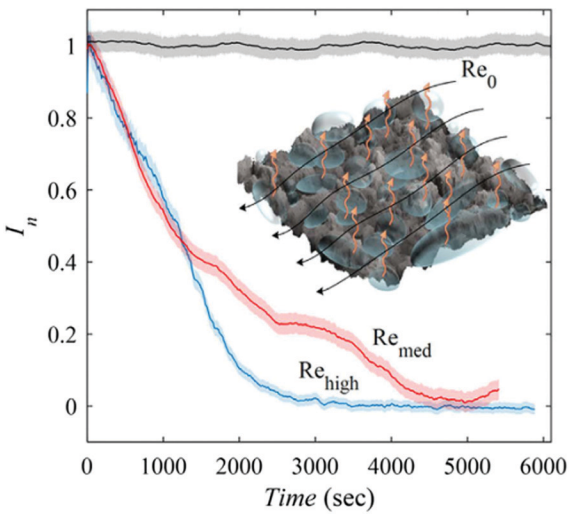

Fig. 23 Normalised reflected light intensity as a function of immersion time in under-saturated conditions (95% saturation). Re_0 indicates a sample within still waters and shows how as the Reynolds number increases the rate of dissolution, as indicated by a loss in intensity, increases. The black arrows indicated the direction of fluid flow and orange indicated the direction of air loss from the plastron. Reproduced with permission from ref. 47. Copyright (2017) Springer Nature Limited.

In real-world conditions, surfaces will not be in deionized water and as such will be exposed to particles that will collide with the plastron as fluid flows over the surface. To model this, 2 μm (average size) silver-coated glass spheres were added to the water at a concentration of 20–30 particles per mm^3. In static conditions, the presence of the micro-particles did not affect the plastron lifetime, however, once flow was applied, the plastron lifetime decreased by 50%. This results from the particles impacting the plastron and destabilizing the trapped air, in addition to damaging the surface structure.

4.3 Condensation

Formation and condensation of water droplets can occur as a result of impurities on the surface of a submerged superhydrophobic material and offer an alternative mechanism by which a wetting transition can occur. Though not as extensively studied as pressure experiments, the effects of microdroplets have been observed. Lv *et al.* recorded the growth of microdroplets on cylindrical micropores in a silicon substrate using LCSM (Fig. 24).[138] Hydrophilic impurities on the surface facilitated the growth of microdroplets.

From the recorded images, it was deduced that microdroplets were forming at the bottom of pores with defects, and advanced until they reach the upper interface. At this point, the interfaces coalesce and start the transition of the liquid–air boundary down the micropore until a full wetting transition has occurred. After coalescence of the meniscus and microdroplet, a transition to a Wenzel state occurred within 1 minute.

The above discussion highlights how the act of submerging surfaces exposes the air layer to a range of new factors which can decrease the stability of the entrapped air. Increased fluid pressure and fluid flow act to destabilise the plastron leading to a loss of air and, therefore, a loss of beneficial properties. Differing from sessile droplets on a surface that only need to satisfy a mechanical equilibrium, a new chemical equilibrium is also established which drives the diffusion of gas from the plastron. Through the design of surface topography, the rate at which air is lost, resulting from these mechanisms, can be decreased. However, in real-world environments loss of air will occur after some time if no procedures are set in place to replenish air.

5 Approaches for underwater stability in manufactured surfaces

The understanding of plastrons and their decay, in combination with natural designs with high air retention, has led to much research attempting to fabricate surfaces with high underwater stability. As elaborated earlier in Section 4.1, high water pressures and/or pressure fluctuations can displace trapped air and a Cassie–Wenzel transition occurs.[45,57,139–141] Starting from this definition, some routes have been developed to overcome this issue and enhance underwater stability. These routes can be classified into three major categories and are discussed with detailed examples in this section.

(1) Systems inspired by nature: many reports have directly utilized natural references to improve the properties of man-made surfaces. In these reports, the detailed study of natural

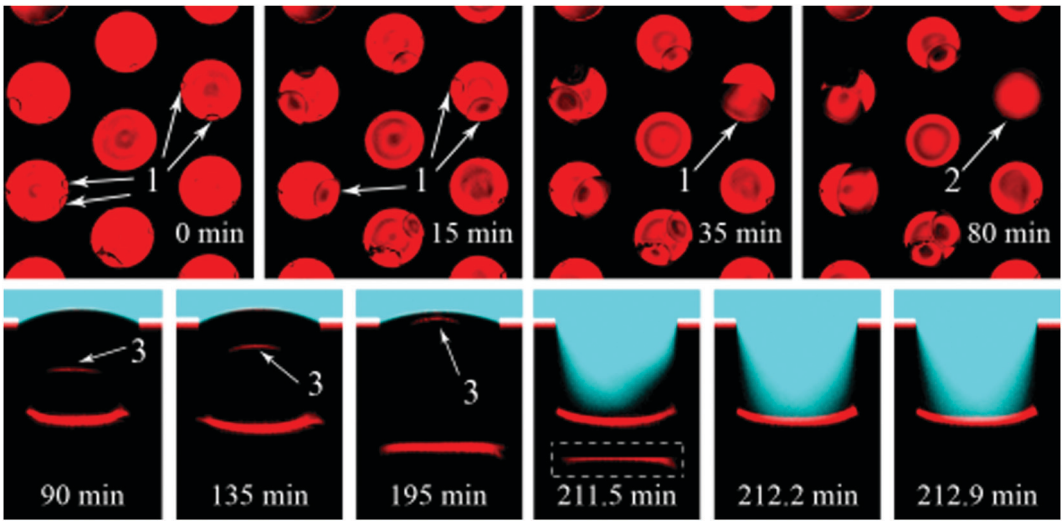

Fig. 24 LSCM images showing the formation of microdroplets. Top row: Top view of microdroplets forming in pores (dark circles indicated by (1). Bottom row: Images of a pore in which the dark circle has fully covered the bottom of micro-pore (labelled 2) showing the wetting transition that results from the formation of a condensed droplet (indicated by 3). Reproduced with permission from ref. 138. Copyright (2015) American Chemical Society.

designs (*e.g. Salvinia* leaves) has directly influenced the choice of selected materials/chemicals and fabrication methods, which helped to improve the air retention ability.[142–145]

(2) Controlling plastrons' environment: other methods attempt to work on the environmental conditions around the plastrons and how to make them less detrimental for plastrons' lifetime. In this case, the target is to record higher failure/breakdown pressures than what would be achieved solely by optimising design/fabrication conditions.[115,141,146,147] Some researchers reported the ability to adjust the plastrons pressure in response to changing water pressure (by changing the depth of submersion, and/or applying flow, *etc.*). Others reported controlling the gas-solubility of water to decrease air diffusion from plastrons.

(3) Plastron regeneration/recovery: while it can be challenging to ensure that the air layer would always remain stable, some reports tried to find ways by which a failed system with damaged plastrons can be recovered.[45,148]

5.1 Systems inspired by nature

As discussed in Section 2, nature has provided numerous examples of high-stability plastrons. Among these examples, many reports expressed a great interest in the intricate structure of *Salvinia* leaf and its resultant underwater stability.[142–144] The "*Salvinia* effect" has received particular attention as it has excellent air layer stability but does not display extreme water-repelling properties, with reported WCAs of $\leq 140^{\circ}$.[76,149] From investigations of the leaf properties and structure, it was concluded that five factors are essential for any surface to show the *Salvinia* effect: (i) choosing an inherently hydrophobic material, (ii) inducing a high aspect-ratio feature (hair, filament, *etc.*), (iii) the elasticity of these features, (iv) the presence of small inclinations, and (v) chemical heterogeneous.[71,80,92,150] The reported *Salvinia*-inspired surfaces aimed to incorporate as many of these five factors as possible, with the hope of obtaining similar plastron stability when submerging synthetic super-hydrophobic materials underwater.

In some reports, attempts to fabricate an exact duplicate of *Salvinia* hair features with the egg-beater attachments were made, utilizing techniques that enable high control over the product's dimensions, *e.g.* 3D printing and direct laser lithography.[142,143,151] Yang *et al.* utilized a mixture of photocurable resins with multi-walled carbon nanotubes to construct the 3D-printed *Salvinia* leaf (Fig. 25a).[142] Tricinci *et al.* were able to scale down the original leaf hairy features (100 times smaller) and fabricate a micropatterned surface using direct laser lithography (Fig. 25b).[143,151]

In a different study, Zheng *et al.* attempted to mimic the heterogeneity of the *Salvinia*'s hairs and fabricate a hydrophobic structure with hydrophilic pins (Fig. 25c).[144] For this purpose, the meniscus-confined electrodeposition technique was utilized (Fig. 26). Taking advantage of the trapped air, the metal was deposited only on the tips, as there is no electric current in the areas that are not in direct contact with the electrolyte. This selective coating was found effective to induce the pinning effect and increase the droplet adhesion to the tips. This was noticed when compared to that of the uncoated-hydrophobic surface in terms of the depinning force and contact angle hysteresis.[144]

Other attempts were made at fabricating air-retaining synthetic surfaces, inspired by the *Salvinia* leaves, *via* the employment of techniques with less morphological control, as such methods could be highly expensive and not commercially scalable.[116] Mundo *et al.* reported using oxygen-fed plasma etching on Teflon sheets to construct random cones.[152,153] Depending on the etching conditions, these cones could be either topped with spheres or filament-like structures (Fig. 25d and e).[152,153] When both surfaces were placed underwater, it was noticed that, unlike the sphere-topped surface, the filamentary-topped material appeared shiny, indicating a layer of air being preserved.[153] This was attributed to the fact that the open filaments with air cavities present, act similarly to the egg-beater attachments in *Salvinia* leaves,

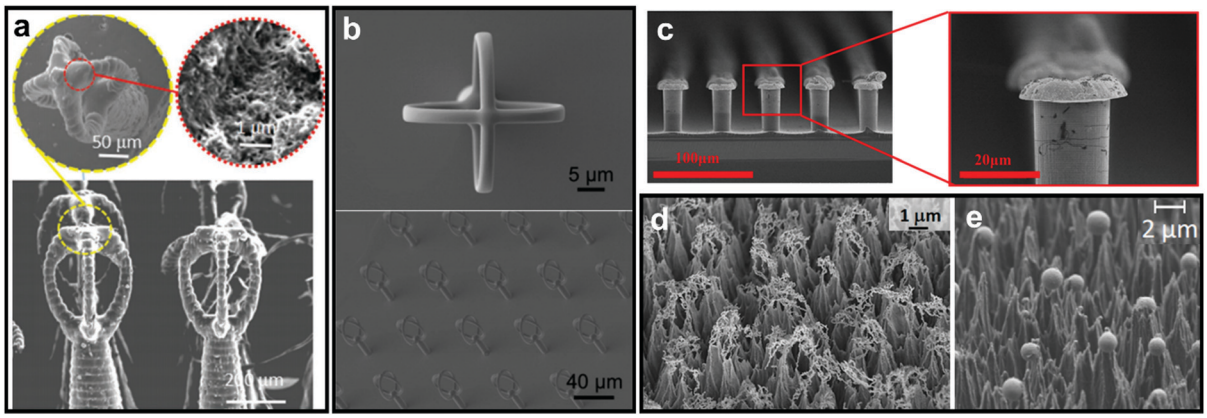

Fig. 25 SEM images of *Salvinia*-inspired manufactured systems. The egg-beater array was fabricated using (a) 3D printing and (b) direct laser lithography. The selective deposition of hydrophobic tips on hydrophobic features/surface was done using (c) meniscus-confined electrodeposition. Teflon sheets were microstructured into cones using oxygen-fed plasma process, with either (d) filaments or (e) spheres on top of the structure. (a) Reproduced with permission from ref. 142. Copyright (2018) Wiley-VCH Verlag GmbH & Co. KGaA. (b) Reproduced with permission from ref. 151. Copyright (2017) MDPI. (c) Reproduced with permission from ref. 144. Copyright (2017) American Chemical Society. (d) Reproduced with permission from ref. 152. Copyright (2017) MDPI (e) Reproduced with permission from ref. 153. Copyright (2016) Elsevier Inc.

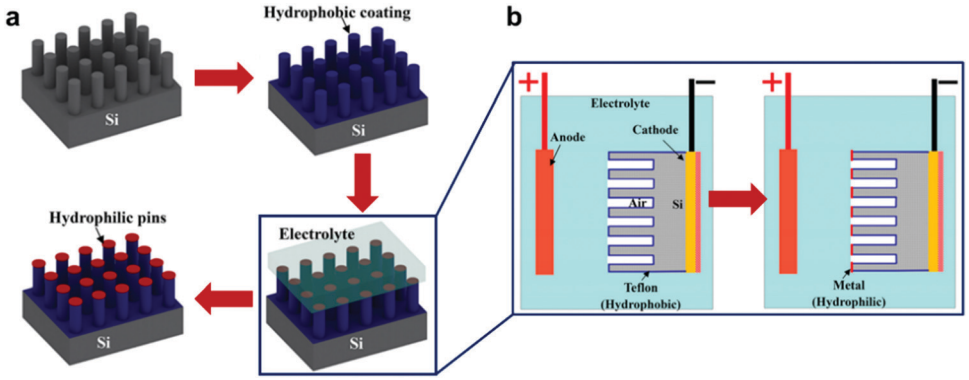

Fig. 26 (a) Fabrication process of hydrophobic-coated Si-micro-posts with hydrophilic metallic pins. (b) Demonstrates the meniscus-confined electrodeposition process that is used to selectively coat the pins and leave the rest of the structure. (a and b) Reproduced with permission from ref. 144. Copyright (2017) American Chemical Society.

which was not possible in the case of the solid spheres.[153] In another report, Babu *et al.* applied water-assisted chemical vapour deposition to synthesize vertically aligned carbon nanotubes.[150] To make them superhydrophobic, a regrowth process of CNTs was initiated to roughen the surface, followed by coating with PDMS.[150] Again, the surface shows the reflective layer when submerged, demonstrating air-retention ability.[150]

In contrast to the previous examples, other reports were interested in mimicking different creatures which rely on other mechanisms for air retention. Air-retaining grids are not common in nature; examples of creatures that contain grid-like structures as a part of their biological body are scarce, but have been known, *e.g.* the plant *Aponogeton madagascariensis*, Fig. 27a, and examples where these grids display air-retaining abilities are even rarer.[92] The only known example of this case is *Hydrozetes* (a schematic of its surface in Fig. 27b).[92,154] Its structure consists of a grid held by props, which Mail *et al.* were aiming to mimic (Fig. 27c). They examined different geometric shapes of the meshes (round, square, hexagonal, and rectangular) with

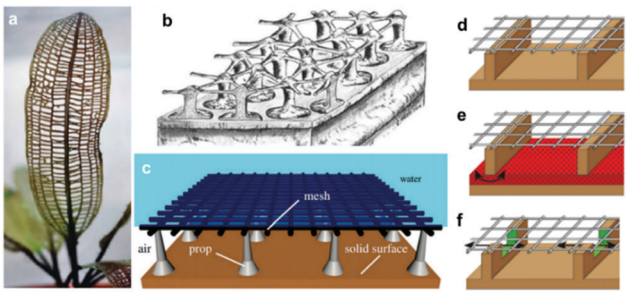

Fig. 27 (a) *Aponogeton madagascariensis* is an example of plants with grids in their structure, while (b) *Hydrozetes* is probably the only known plant where the grid is used to air retention purposes. The image is a schematic of the plant structure. (c) A schematic of the proposed air-retaining grid. (d–f) Schematics for different designs of the air grid. In (d) the compartments are not connected, while in (e) and (f), the compartments are connected by a porous sintered metal sheet (red) in the bottom and by small embrasures (green) located under the grid, respectively. (a–f) Reproduced with permission from ref. 92. Copyright (2019) the Royal Society.

different opening sizes, and also different holding props (either allow or don't allow connection between compartments). It was found that while meshes with smaller opening areas remain stable at higher pressures, square geometries showed better air-retention compared to the circular ones with the same opening size. It was attributed to the fact that square shapes have higher circumferences (when both shapes have equal areas), which results in water being suspended by a higher solid fraction, and subsequently, more energy is required to overcome this interaction. In addition, connected compartments displayed rapid wetting at the beginning of the experiment, as air can travel freely to compartments where water pressure is minimized. As the experiment proceeded, the isolated plastrons decayed more rapidly, while connected compartments allowed higher air-volume preserved, and hence a higher resistance against the water pressure.

Mimicking the surface structure and/or chemical composition of naturally occurring air-retaining surfaces has led to the fabrication of materials with compelling properties. However, further reports have been focused on finding characteristics shared by many natural surfaces and applying this feature to their proposed designs. As mentioned in Section 2, properties like the density of the hairy features, their physical properties and alignment with respect to the surface were found common between different natural surfaces, and are believed to be crucial to their air-retention abilities.

As an example, a straightforward approach has been reported for the synthesis of nanofur (Fig. 28a and b) inspired by the dense-hairy layer covering the *Salvinia* leaf and the *Notonecta glauca* bug.[114,116] A thermoplastic polymer (polycarbonate) was placed between two moulds and pressed with heating, at a temperature that exceeded the polymers glass transition temperature (T_g). When the mould was pulled away, the softened polymer randomly elongated, increasing the aspect ratio of the resultant surface, in addition to enhancing roughness.[114] Although mould fabrication in general can be complex, the mould employed here was made by sandblasting (Fig. 28a), a technique which effectively roughened the steel plate surface. Using this method, a dense layer of hairs (nano/microscale) were obtained, with microcavities randomly distributed between them, as a result of using sandblasting particles (Fig. 28c).[114,116]

The possibility of introducing the pinning effect into the nanofur samples was examined by Vüllers *et al.* Experimentation was carried out to probe the effect of surface energy, controlled by changing the surface coating, on the air retention ability.[115] The polycarbonate nanofur was coated with a higher (silver) and a lower (fluoroalkylsilane, FAS) surface energy material. For the silver-coated sample, the penetration depth (the distance that the air–water interface moves when changing hydrostatic pressure from 0 to 300 mbar) was found to be the same for the original uncoated nanofur, while it increased dramatically (from 11 μm to 92 μm) for the FAS-coated sample.[115] This was attributed to the fact that the water pinning effect disappeared, due to the lack of points where water could adhere when the surface energy of the coating was lowered.[71,115] By measuring the pressure at which the air–water interface breakdown occurs, both the hydrophilic silver and the hydrophobic FAS coatings had lower air stability compared to the uncoated sample.[114,115] This suggests that although a low surface energy material would limit the pinning effect, a high surface energy (hydrophilic) coating would, lower the energy cost of wetting the surface. Hence, a material with moderate surface energy is required to achieve balance. This means that a water droplet pinned on the tips of hydrophobic hairs, its most energetically favourable position, would require energy input to be relocated, either forced to wet the surface or be removed from it.[76,115] It is noticed that this situation is differentiated from superhydrophobic surfaces that are not involved in underwater applications, where lower surface energy leads to a more slippery surface and, hence, higher water repellence.[155,156]

Another aspect that has been featured in many natural examples, such as, *Salvinia* leaves and the skin of springtails (Collembola), is the re-entrant structure.[90,157] Any structure with a convex texture ($\beta < 90^\circ$, Fig. 29b and c) is considered to be re-entrant, this definition can include a range of different

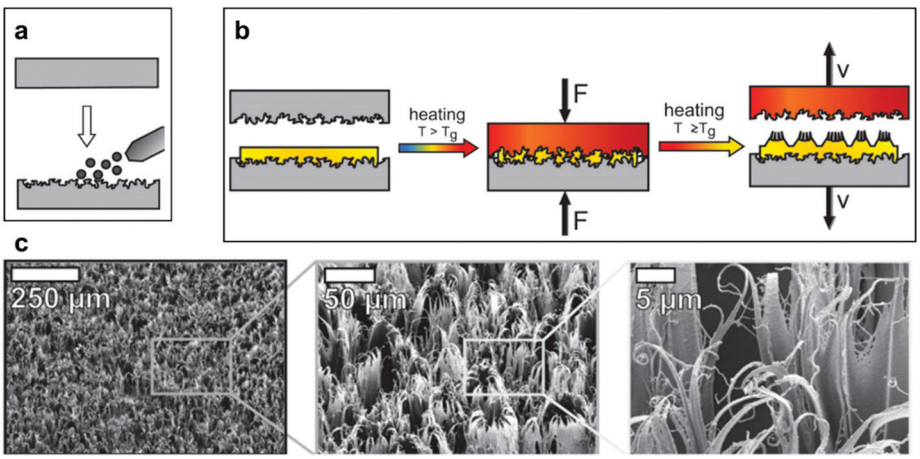

Fig. 28 (a) Sandblasting of a steel plate to make a mould. (b) The mould is pressed against the polymer under heating. When removed, the soften polymer elongates to form the high aspect-ratio hairy features. (c) SEM images of nanofur showing its high roughness and features' density. (a–c) Reproduced with permission from ref. 116. Copyright (2014) Wiley-VCH Verlag GmbH & Co. KGaA.

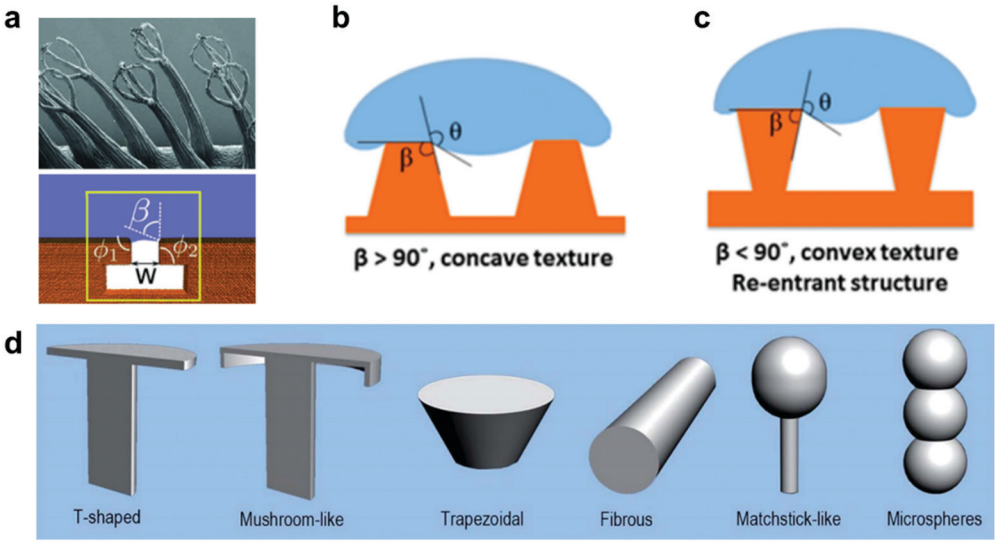

Fig. 29 (a) *Salvinia* egg-beaters could be modelled as a re-entrant structure. (b and c) Schematics showing the difference between concave and convex texture. (d) Different geometries that lay under the re-entrant structure definition. This includes (from left to right) t-shapes, mushroom-like, trapezoidal, fibrous, matchstick-like and microspheres geometries. (a) Reproduced with permission from ref. 90. Copyright (2015) Amabili *et al.* Published by Wiley-VCH Verlag GmbH & Co. KGaA. (b and c) Reproduced with permission from ref. 145. Copyright (2019) American Chemical Society. (d) Reproduced with permission from ref. 158. Copyright (2017) The Royal Society of Chemistry.

shapes and geometries, as illustrated in Fig. 29d. These structures have captured many interests due to their ability to maintain a stable air layer, even with liquids with low surface tensions.[91,158,159] This is because the three-phase contact line is pinned by the edges of these textures, which can suspend liquid for a period that is 10^7 million times longer compared with simple cylindrical textures, as reported by Domingues *et al.* (for mushroom-shaped silica cavities immersed in hexadecane).[160–162] Many reports highlighted the application of these surfaces as superomniphobic surfaces,[96,163–166] with the ability to repel both water and oil, even when employing textured hydrophilic surfaces.[167–169] Some reports utilized these properties to create surfaces with a controlled switching ability between superomniphobic and omniphilic, using an electric[170] or a magnetic[171] field. More relevantly, re-entrant structures have been reported for water immersions and they were found to increase the breakdown pressure at which a Cassie–Wenzel transition takes place, making these surfaces more stable underwater compared to simple cylindrical textures.[145,161,162]

Re-entrant structures are reported for the fabrication of distillation membranes, due to their stability against fluid pressures which enable their application under water-fluxes during the distillation process.[145,172,173] Lee *et al.* reported a dual-layer membrane fabricated by; (1) electrospinning of polyvinylidene fluoride-*co*-hexafluoropropylene (PVDF–HFP), followed by, (2) electrospraying of PVDF/PDMS-microspheres (Fig. 30).[173] The presence of polymer microspheres formed the re-entrant convexity, which allowed air-pocket formation and water repellent behaviour. The liquid entry pressure (LEP, the pressure at which liquid starts entering the pores and wetting the membrane) measured for membranes with (PDMS-3%, PVDF-2%) sprayed solution was 111 kPa (1.11 bar), with a partial wetting observed when using seawater with 0.1–0.2 mM sodium dodecyl sulfate (SDS).[145] To extend the membrane anti-wettability under harsher saline conditions, Deka *et al.* aimed to increase the membranes roughness and superhydrophobicity by including hydrophobic silica aerogel into the microspheres (Fig. 30c and d).[145] Using 30% aerogel concentration, the LEP was enhanced to reach 129.5 kPa, and the wetting resistance was observed even under 0.5 mM SDS concentration.[145]

Although these re-entrant structures have shown the ability to hold a stable air layer, this can be highly affected by structural defects. Domingues *et al.* illustrated that for single, isolated mushroom-like pillars, when the surface suffers from localized physical damage (*e.g.* broken pillars), this discontinuity causes a rapid wetting at the defect area. This then allows the liquid to push the trapped air outside and spread further to un-damaged areas, leading to a complete surface wetting (Fig. 31a).[162] As a solution, they proposed mushroom-like cavities (also referred to as doubly re-entrant cavities), in which the solid material is connected and air pockets are isolated (Fig. 31b). To investigate this, doubly re-entrant silica surfaces with induced local damage were immersed in water. Fig. 31c shows optical images of the wetting state at different periods. In these images, cavities (3, 1), (4, 1) and (3, 2) were connected before the experiment took place. It was noticed that after the three cavities were filled, the surrounding cavities remained intact, even after 30 days of immersion.[162]

In another report, t-shaped (re-entrant) and doubly re-entrant cavities were compared to simple cavities in terms of their ability to sustain the air layer (Fig. 31d). Circular geometries, along with square and hexagonal (with different corner radii) were prepared from un-coated silicon wafers.[161] When measuring breakthrough pressures (P_b) (Fig. 31e), all structures with simple cavities failed at low pressures compared to other cavities. It was

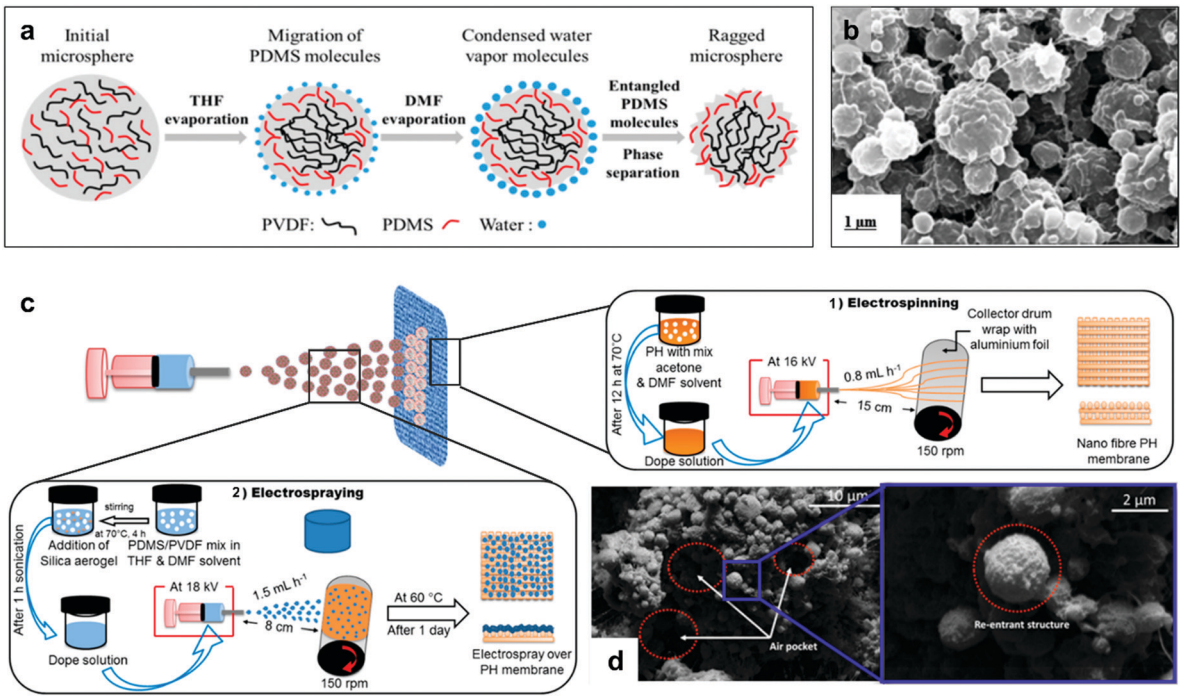

Fig. 30 (a) A schematic showing the formation of PVDF/PDMS-microspheres. (b) SEM image of the electrosprayed microsphere solution (PDMS-3%, PVDF-2%). (c) The process of fabricating electrospun (PVDF–HEP) membranes followed by electrospraying of aerogel/PDMS/PVDF solution. (d) SEM images of a membrane fabricated using (aerogel-30%, PDMS-3%, PVDF-2%) spraying solution. The image shows the formation of air pockets and defined re-entrant structures. (a and b) Reproduced with permission from ref. 173. Copyright (2017) American Chemical Society. (c and d) Reproduced with permission from ref. 145. Copyright (2019) American Chemical Society.

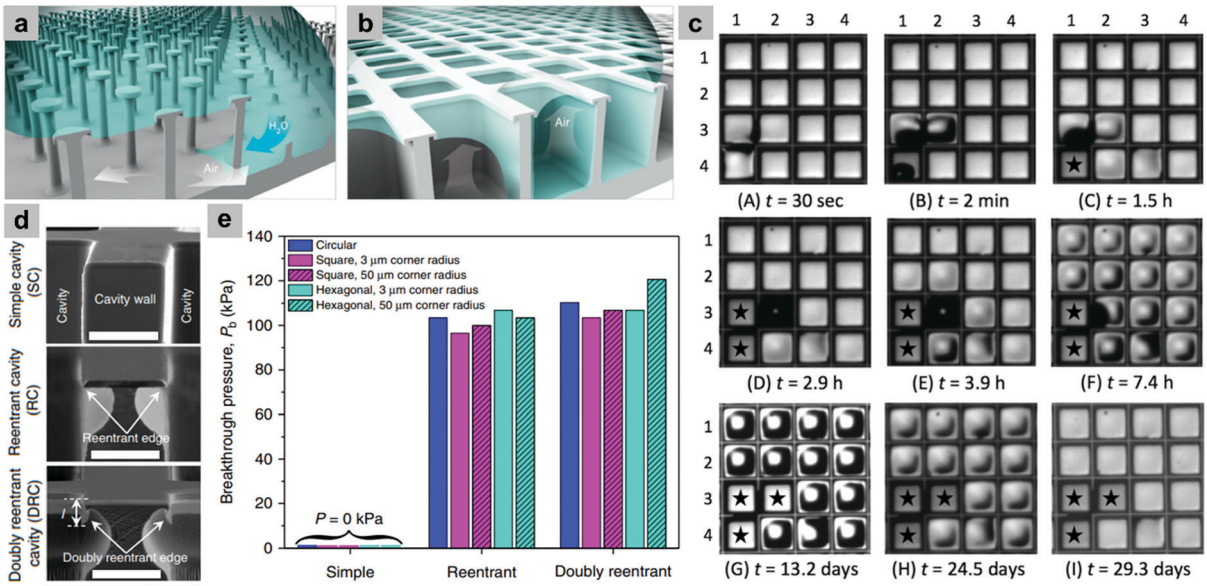

Fig. 31 (a and b) Schematics show the impact of physical damage on the wetting resistance in the case of pillars and cavities, respectively. (c) Optical images for the wetting transition of doubly re-entrant silica surfaces immersed in water, with cavities (3, 1), (4, 1) and (3, 2) are connected due to physical damage. Cavities marked with a star (★) are water-filled. (d) The different cavity-shapes examined (from top) were simple, re-entrant and doubly re-entrant cavities. (e) Graph for breakthrough pressures measured for different geometric microtextures with different cavity shapes, showing how complex cavities are better in stabilizing air layers compared to simple cavities. (a–c) Reproduced with permission from ref. 162. Copyright (2017) American Chemical Society. (d and e) Reproduced with permission from ref. 161. Copyright (2018) Nature Publishing Group.

found that doubly re-entrant cavities, in general, show better stability against high pressures.[161] More importantly, the dependence of P_b on the cavity diameter was highlighted. While the examined cavities with a diameter = 200 μm showed a P_b

value ranging between 100–120 kPa, decreasing the diameter would allow for a higher contribution of Laplace pressure pushing water upwards. Typically, the predicted P_b for cavity diameter = 100 nm is 1700 kPa.[161] This gives a guide for designing surfaces with sustained hydrophobicity underwater.

In summary, nature designs are a great source of inspiration for their exceptional air retention abilities. From the *Salvinia* leaves to the dry-underwater insects, many lessons were learned regarding the influence of surface design, structural geometry and chemical composition. In addition, the challenges of mimicking natural surfaces, with some of them exhibiting a degree of complexity, have been addressed and many solutions were proposed. However, the progress achieved to date is still considered to be below the required for many application fields, which leaves room for more efforts to be invested.

5.2 Controlling plastrons' environment

The development of the structural design of materials has led to significantly improved underwater stability. However, currently obtained results have limited applicability relative to the expected challenges faced in a real-world application environment. Therefore, alternative approaches are required, one of these methods is the control of the plastrons pressure, adjusting it in response to the increased water pressure.[115,141,146,147] Other methods include operating under air-saturated water flow,[174] and heating the surface to create a stable solid–vapour interface.[29,57] The following section will discuss these approaches and how they enhance plastrons' lifetime.

5.2.1 Controlling pressure. Materials targeted at increased plastron stability commonly aim to increase the tolerance against high fluid pressures. However, the air pressure within the plastron would change insignificantly (compared to the outside pressure) regardless of the pressure change applied by the fluid above the plastrons, which is a major threat to plastrons longevity (Section 4).[146] Controlling plastron pressure and enable their adaptation with the applied pressure can be an effective solution for this issue.

Carlborg *et al.* designed a channel that allows the trapped-air pressure to increase when liquid flow exerted pressure on plastrons.[146] Fig. 32a and c shows a schematic of the standard channel and the self-regulating design they proposed. In the self-regulating design, a feedback channel is introduced, which is connected to the air trapped in the gas pockets. When the flow takes place, the liquid compresses air in the feedback channel, which in turn increases the pressure in the air pockets, allowing for longer sustainability of the air layer.[146] Fig. 32b and d shows the difference between both channel designs in a prototype experiment. Once the flow started, gas pockets in the standard design failed gradually. However, the self-regulating design allows pressure adaptation with increasing fluid pressure. When the fluid pressure was raised from 2 kPa to 8 kPa and then 25 kPa, the pressure inside the gas pockets increased in response from 0 kPa to 3 kPa and then 14 kPa, respectively.[146]

A notable limitation of the previous design is when the fluid pressure goes above a certain threshold, the feedback channel would no longer be able to accommodate the increased liquid volume.[141] When this point is reached, the system would start to behave like the standard system, and the air stability would be threatened. Another way to overcome this and increase the lifetime of the plastron further was introduced by Vüllers *et al.*,

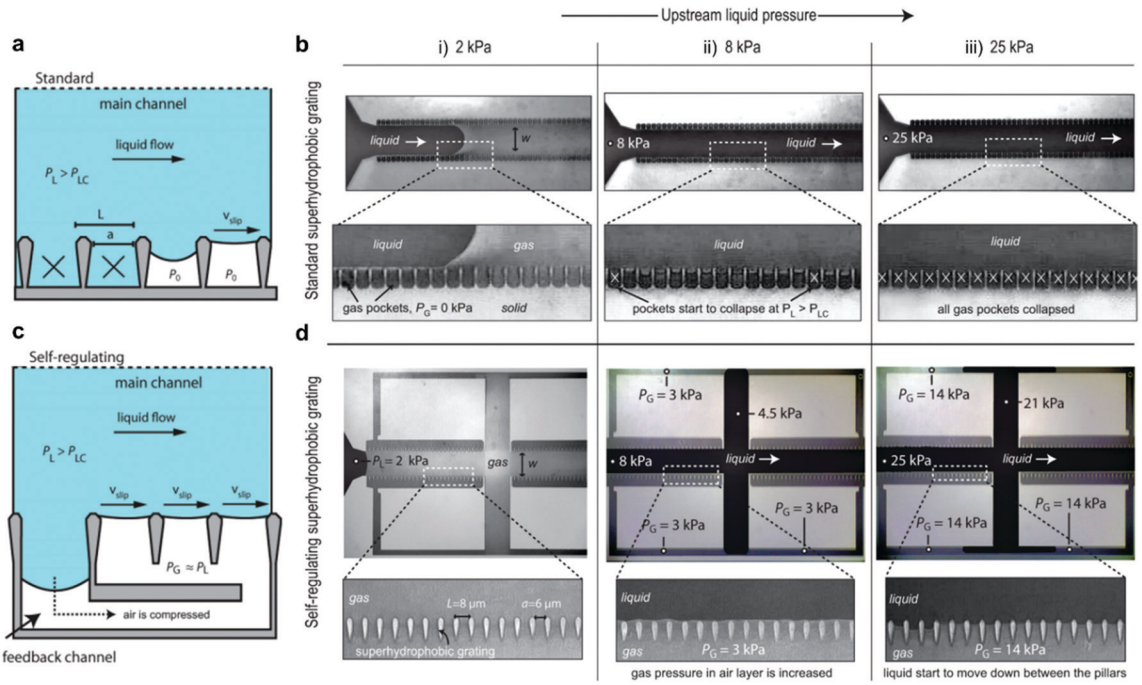

Fig. 32 Schematic of (a) the standard channel and (c) self-regulating channel. The difference in liquid pressure tolerance is shown in (b) (standard) and (d) (self-regulating) under the following pressures: (i) 2 kPa, (ii) 8 kPa and (iii) 25 kPa. (a–d) Reproduced with permission from ref. 146. Copyright (2010) American Chemical Society.

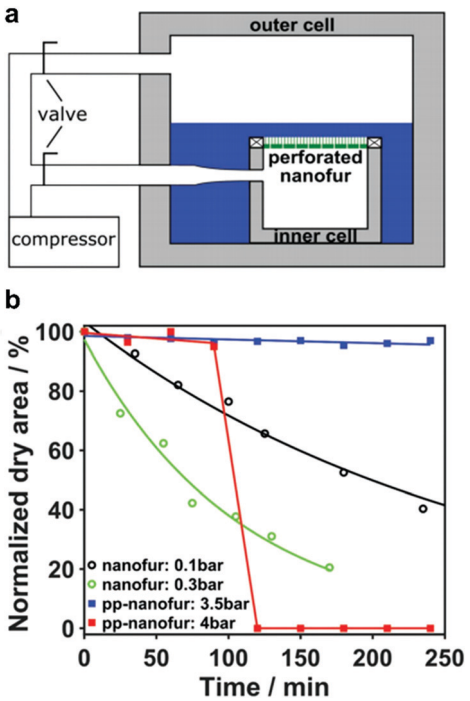

Fig. 33 (a) Schematic of the double-cell setup used to pressurize the nanofur (attached to the inner cell) and to control the applied water pressure (outer cell). (b) A graph showing the change of dry area percentage with time for samples immersed under different pressures. (a and b) Reproduced with permission from ref. 115. Copyright (2018) Wiley-VCH Verlag GmbH & Co. KGaA.

as illustrated in Fig. 33a.[115] Nanofur was used in this experiment, which was perforated to allow pressure control. The nanofur was attached to the inner cell in a double-cell setup, allowing pressurizing of the trapped air in the plastrons. The outer cell, where water is placed, was also pressure-controlled. The experiment revealed that, while un-pressurized nanofur suffered from an exponential decrease in the percentage of the dry area over time, even under a small applied external pressure, pressurized samples showed much-enhanced stability (Fig. 33b). Samples tested under 3.5 bar remained almost completely dry for over 4 hours. Increasing the pressure, 86% of trapped air was retained at 4 bar, which is equivalent to submerging the surface at 40 m water depth.[115]

A modified approach has been reported by Li *et al.*, with porous superhydrophobic titanium (Ti) surfaces.[141] The surfaces were nano/micro-structured with the presence of micropores, which allowed an active supply of air to feed the plastrons (Fig. 34). While water pressure increases, the air supply creates an opposing pressure, which stabilizes the trapped air and prevents plastrons decay.[141] Using this setup, the Ti surfaces were able to sustain the air layer under a 350 kPa hydrostatic pressure (3.5 bar).[141]

To conclude, controlling the plastron pressure gives a way to further extend the lifetime of the plastron. The total pressure tolerance of a system could be much enhanced by adapting the plastron pressure to the surrounding environment, compared to relying on the superhydrophobic properties of the surface only without effective pressure control. Approaches reported to increase the plastrons pressure, although limited, have been shown to obtain interesting results. These include; creating a pressure feedback channel for plastrons, pressurising the samples during testing, and pumping air through a porous superhydrophobic surface.

5.2.2 Application under air-saturated water. Xiang *et al.* investigated the effect of using air-saturated water for immersion testing on plastron stability.[174] Lotus leaves, which are not known for high stability underwater, were tested using the setup shown in Fig. 35a. The setup involved a bubbling device to ensure continuous air-dissolution, as well as a confocal microscope to follow the wetting transitions with time. The experiment conducted at 1.5 bar and a flow rate of 23 mL min^{-1}. In the case of unsaturated water, the air–water interface (indicated by the red regions in Fig. 35b–e) has completely disappeared after 2 min. On the other hand, using a saturated water-flow enhanced the retention ability 120-times, as the leaves maintained the air-pockets until 240 min without showing a sign of decay.[174] The significance of this experiment was not just in obtaining these results under flow conditions, which are known to decrease plastron lifetime by ~50%,[175] but also to achieve this with a surface that displays no significant air-retention abilities under normal conditions. As a reference, Sheng *et al.* stated that, under static conditions and unsaturated water, lotus leaves showed a WCA (measured after being just removed from water) of 150 °C after various pressure treatments, reaching 13.5 kPa (0.135 bar) where the WCA dropped to ~56°.[176,177]

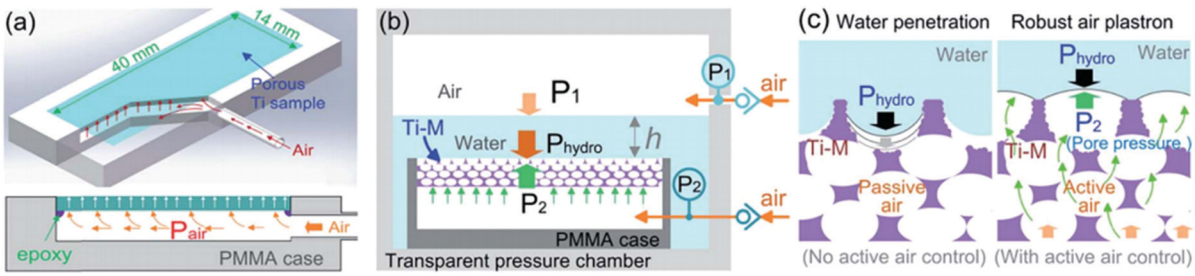

Fig. 34 Schematic of the setup utilized by Li *et al.* (a) The porous superhydrophobic surface is attached to an inner cell, which is connected to an air supply source. (b) As the water pressure increases, the air supply continues to feed the plastrons, making the trapped-air pressure increases. (c) A comparison between (no-active-air-control) case (left) *versus* the presence of air control (right). In the first case, water pressure (P_{hydro}) forces the decay of the plastrons, while in the second case, an opposing pressure (P_2) is applied by the air supply, making the plastrons more stable. (a–c) Reproduced with permission from ref. 141. Copyright (2019) The Royal Society of Chemistry.

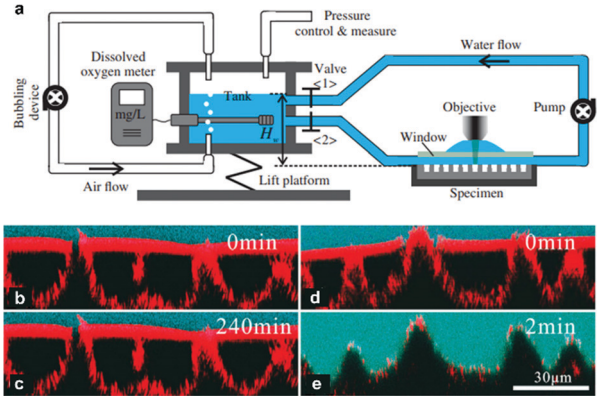

Fig. 35 (a) A schematic showing the experiment setup. Water saturation is maintained and controlled by attaching a bubbling device and a dissolved oxygen meter. Confocal microscopy was incorporated to visualize plastrons decay. (b–e) Images obtained from confocal microscopy of a lotus leaf placed under (b and c) saturated and (d and e) unsaturated water. The blue and red regions show water and air–water interface, respectively. (a–e) Reproduced with permission from ref. 174. Copyright (2017) American Physical Society.

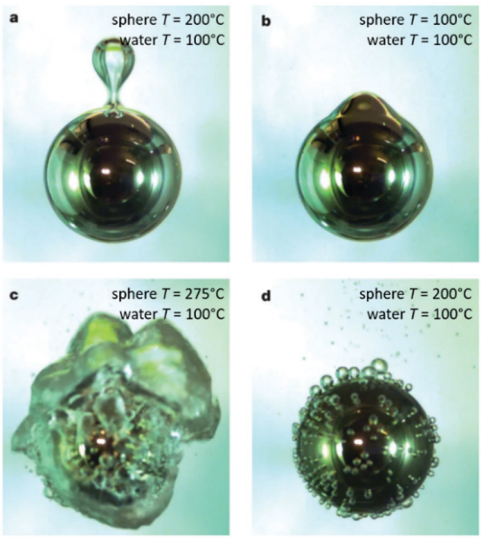

Fig. 36 The cooling of a superhydrophobic sphere (a and b) and a hydrophilic sphere (c and d). (a and b) Reproduced with permission from ref. 29. Copyright (2012) Nature Publishing Group.

5.2.3 Leidenfrost surfaces. When a hot surface comes in contact with a liquid, a vapour film is generated which surrounds the solid surface and isolate it from that liquid, this is known as Leidenfrost effect.[29,57,178,179] A stable vapour layer is only obtained when the surface reaches a certain critical temperature.[29,179] This layer decelerates the heat exchange process between solid and liquid. Once the solid cooled down below the critical temperature, the vapour layer vanishes rapidly.[29] As the Leidenfrost effect can significantly reduce surface drag, this phenomenon has been considered in underwater surfaces.[29,57] A challenge in applying this principle is the elevated temperatures that are required for vapour layer formation, which can reach as high as 700 °C.[29]

Vakarelski *et al.* showed that textured superhydrophobic surfaces can prevent vapour-layer collapse until completely cooled, and that their critical temperature is typically lower compared with hydrophilic and superhydrophilic surfaces. The maximum critical temperature for a hydrophobic or superhydrophobic surface required to observe this behaviour is ~400 °C.[29] Considering the cooling process, Fig. 36a shows the formation of a stable vapour layer around a superhydrophobic sphere at T = 200 °C, water T = 100 °C. This layer was not disturbed until the sphere reached the ambient temperature (100 °C, Fig. 36b). On the other hand, a hydrophilic sphere at T = 275 °C, water T = 100 °C shows an immediate transformation from vapour-layer boiling to a nucleate boiling, which leads to few isolated air bubbles as the sphere reached T = 200 °C (Fig. 36c and d).

Using the Leidenfrost effect still faces many challenges, like the design complexity in continuous heating that needs to be implemented to sustain the vapour layer during the whole application period. The research in this area is considered to be at its elementary steps. Further research should be conducted to optimize surface properties, as well as finding suitable applications where this method can compete with other approaches to fabricate underwater hydrophobic surfaces.

5.3 Plastron regeneration/recovery

A general aim for the discussed research focuses on increasing the plastrons lifetime. However, in most cases, it is shown that plastrons' failure (although delayed) is not completely hindered.[115,141] If long-term applications are being targeted, this would present itself as one of the greatest challenges for these systems, giving that the average plastrons lifetime ranges from hours to a few weeks.[72,73,180,181] Therefore, considering the ability of a failed system to recover and be re-used could be a solution to this issue.[148]

Water splitting reactions have been considered by many researchers as a method of regenerating lost plastrons, as this can be facilitated with low energy consumption, due to the generated gas being stable and compatible with water (*i.e.* non-reactive). Additionally, incorporation into superhydrophobic systems is likely to be straightforward.[50,111,148,182] The gas generated by this reaction can refill the damaged plastron, returning the air-sustaining properties.[111] Lee *et al.* fabricated a gold-coated nanostructured surface that is decorated with other micro-posts made by the patterning of a photoresist, followed by photolithography (Fig. 37a).[148] For the electrolysis reaction, the gold layer acts as the cathode, while a copper wire is placed in the water and acts as the anode. Starting the experiment from the wetted state (with nanoscale grooves still unwetted), bubbles were observed. After less than a minute (for a sample with 100 μm pitch, 50 μm height and 95% gas fraction), the dewetted state was achieved.[148] In another report, photoelectrochemical (PEC) water splitting was applied on a hierarchical SiC/Si nanostructure surface to regenerate the plastron.[111] The fabrication method is shown in Fig. 37b, in which both SiC nanowires and Si micro-posts were combined. Again, after performing the PEC reaction, the surface restored its superhydrophobicity and drag reduction ability.[111] The same conclusion was reached when Zn/O nanorod/Si micro-post hierarchical structures were utilized.[50]

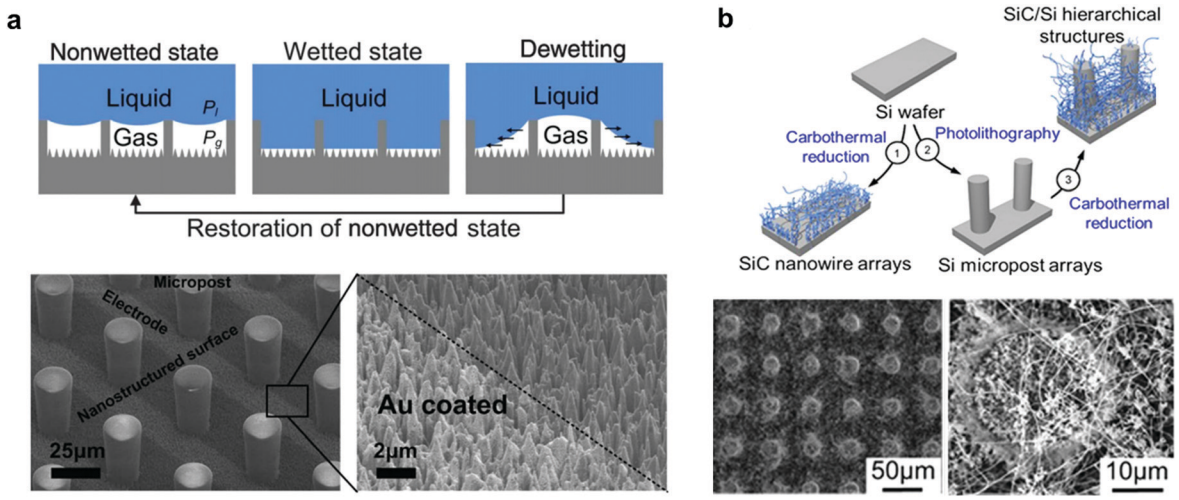

Fig. 37 (a) (above) A schematic for the wetting/dewetting process and (below) SEM images for the prepared surface, showing the micro-posts and the nanoscale gold-coated features. (b) (above) The fabrication of hierarchical SiC/Si nanostructure and (below) SEM of the prepared surface. (a) Reproduced with permission from ref. 148. Copyright (2011) The American Physical Society. (b) Reproduced with permission from ref. 111. Copyright (2016) Nature Publishing Group.

It is notable that for the regeneration of the plastron in these examples, a combination of micro/nanostructuring was required. It is well-established that such a combination is beneficial for superhydrophobicity and all subsequent properties, similar to the Lotus leaves and water spiders' legs.[183,184] In addition, the wetting state from which the plastron is being regenerated is a micro-Wenzel–nano-Cassie state, in which, while the micron-size grooves are wetted, the nano-size pockets remain dry. Therefore, it could be concluded that for a microstructured surface, which facilitates complete Wenzel wetting, it would be challenging to recover after plastron failure. Verho *et al.* highlighted this in their experiment (illustrated in Fig. 38).[185] Simple water suction by a syringe could not restore a single-level topography wetted surface, and the wetting, in this case, is considered to be irreversible. Alternatively, when considering the micro-nano surface topography, the surface could be restored from a nano-Cassie state. In another report, Lee *et al.* showed the possibility of achieving regeneration in various ways (placing in air-saturated water, bringing part of the sample near the surface of the water – the air–water interface – and gas generation) giving that the nano-posts remain unwetted.[186]

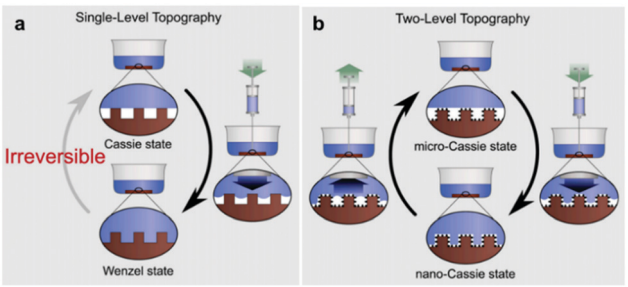

Fig. 38 (a) Single-level *versus* (b) two-level topography in plastrons regeneration. In the first case, the wetting process is irreversible, while for the second, dewetting could be restored. (a and b) Reproduced with permission from ref. 185. Copyright (2012) PNAS.

In response to this challenge, Panchanathan *et al.* reported a micro-structured Si–Pt–Teflon surface where a regeneration from Wenzel wetting was successfully achieved (Fig. 39a and c).[45] The micropillars were constructed from silicon, which is then coated with Pt (except for the tops), and finally with Teflon to make the surface hydrophobic (Fig. 39b).[45] Decomposition of H_2O_2 over a Pt catalyst was chosen as the plastron-regeneration method. It was shown that, even where no nanostructuring was induced, the produced oxygen helped surface recovery and restored the unwetted Cassie state.[45]

In summary, plastrons regeneration could provide a feasible solution to extend or regain plastrons with short lifetimes. This is becoming of high importance as developing a system with general underwater stability is very challenging. Working on

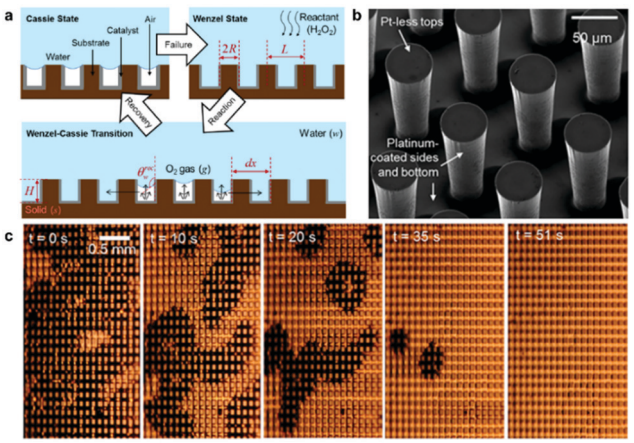

Fig. 39 (a) A schematic of the recovery process proposed. (b) SEM image of the surface, showing where Pt-coated is located. (c) Underwater plastrons recovery at 4.5% wt H_2O_2. The images are taken using total internal reflection at the air–water surface. Reproduced with permission from ref. 45. Copyright (2018) American Chemical Society.

the regeneration ability allows for a longer application time of surfaces and, hence, decreases potential cost. This approach is of great interest in long-term underwater submersion in particular, where durability is highly targeted to avoid/minimize maintenance expenses.

6 Highest-performing manufactured surfaces: what has been achieved

The challenges faced when maintaining plastrons underwater, as illustrated in Section 4, hugely limit the suitability of many surfaces in real-life applications. Developing surfaces with high plastron stability has been widely addressed by many reports in the literature. While many of them highlighted a sustained air layer during immersion for hours, a few reports presented surfaces that could achieve long-time stability and/or at harsh conditions of depth/flow rate.[115,174,181,187] The previous section outlined different approaches that have been employed to fabricate superhydrophobic surfaces with good air-retaining abilities. Here, examples with the highest reported underwater stability, to date, are investigated.

It must be considered that there are no universal plastron stability testing methods, and so variation in the assessment implemented makes it challenging to definitively identify those materials with the highest stability. While some materials have been reported for exceptional long air-layer stability, other materials can be tested in very different conditions. Because the surrounding environment can significantly change with respect to the aimed application, the conclusion on any reported examples must also differ accordingly. As a way to look at the literature more inclusively, the best performance will be judged firstly on the reported stability time (Table S1, ESI†), and then based on the water pressure they can withstand (Table S2, ESI†).

Starting with examples with the longest stability time, the material reported by Martinez-Gomez *et al.*[187] Samples were prepared using a range of hybrid organic–inorganic silica-based particles sprayed on glass substrates, and underwater stability was assessed by visually monitoring the mirror-like behaviour for the samples while immersed in a 2 cm depth of water. It was noticed that after 100 hours, the shiny look started to disappear from some spots instead of evenly covering the whole surface (Fig. 40). However, examining the surfaces immediately after removal from water (without drying) indicated the superhydrophobicity to be preserved. This was used to conclude that the air layer was maintained, and the observed reduction in reflection is linked to its thinning.[187] The surfaces were kept underwater for longer periods, and it was established that superhydrophobicity was sustained even after a six month immersion period.[187] To the best of our knowledge, this is the longest-reported plastron stability for a manufactured surface with straightforward water immersion testing.

Xu *et al.* have reported samples with 'infinite' lifetime underwater utilising trench structures with varying widths.[181] Three trenches with the same length (1 mm) and depth (~85 μm) but different widths (147, 96, 46 μm) were tested (Fig. 41a). The critical immersion depth (H_C), defined as the depth after which the lifetime of plastrons decreased rapidly, was identified for these samples. It was found that with decreasing the trench width, H_C increased from 5 cm to 7.5 cm and 16.5 cm, respectively (Fig. 41).[181] The main

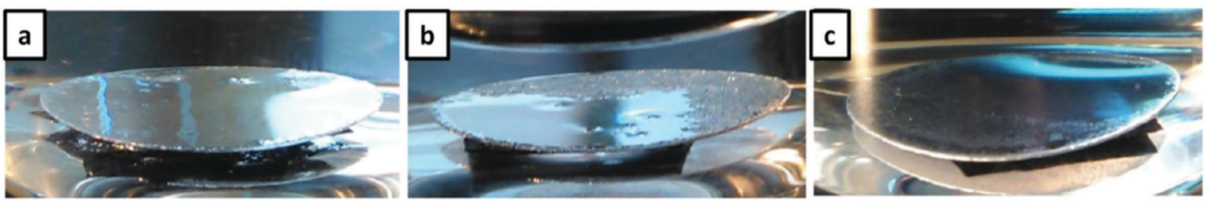

Fig. 40 Photos for coated substrates immersed in water for (a) a few minutes, (b) 100 hours, and (c) after removing and placing in the water again. (a–c) Reproduced with permission from ref. 187. Copyright (2017) American Chemical Society.

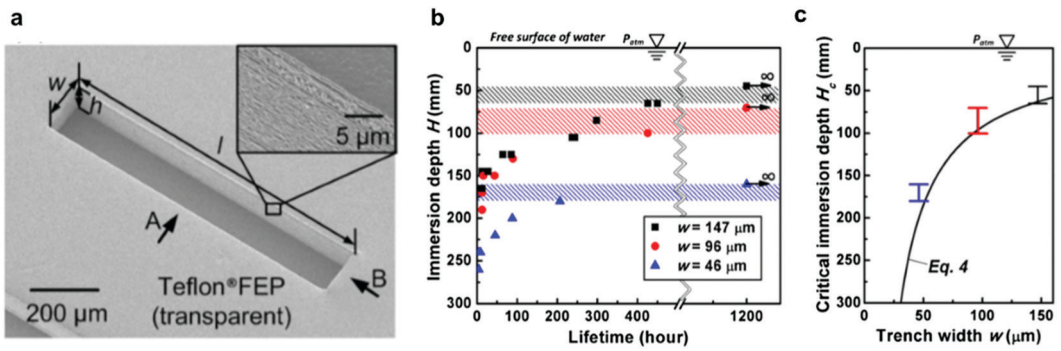

Fig. 41 (a) SEM image of the trench used, with length (l), depth (h) and width (w) indicated. (b) Plastrons lifetime at different immersion depths for 147, 96, and 46 μm trench widths. The graph shows the maximum depth for each trench width at which an infinite lifetime (>50 days) can be obtained (c) critical immersion depth (H_C) for each trench width. (a and b) Reproduced with permission from ref. 181. Copyright (2014) American Physical Society.

finding was that for depths smaller than H_C, the air layer remained stable typically >50 days (indicated as ∞ in Fig. 41b), after which the experiment was terminated.[181] This highlights the possibility of getting long-term stability if depth can be controlled to be less than H_C.

Considering other samples with shorter plastron lifetime, the nanofur prepared by Vüllers *et al.* (Section 5.1) and assessed using LSCM (water depth = 4 mm) showed a sustained air-layer for 31 days, after which the experiment was terminated.[116] In addition, Lee *et al.* reported their $W_{18}O_{49}$ nanowire arrayed superhydrophobic surfaces to remain dry under water-depth of 5 cm for around 9 days, before they started to rapidly become wetted (Section 4.1).[106]

For applications that involve subtle interaction with water, the previous examples could be highly relevant. However, as many of the application fields require operating under deeper water depths, and/or faster flow conditions, *etc.*, the environment chosen for these examples can be seen as too mild, which makes judging on reported stability time only not sufficient to choose the best performing samples. Another issue with applying mild conditions is that the only limiting factor in most cases will be time, which makes many experiments terminate prior to full failure. This makes it more challenging to differentiate between various materials.

Another way to examine this is by comparing the maximum tolerated pressure. In this context, we are looking at the pressure for which failure in air-layer reservation starts. It worths mentioning that some reports chose to state the pressure at which a complete wetting occurs, which sometimes varies significantly from the value we are considering here, especially for samples with a slow degradation of the air layer.

As discussed previously in Section 5.2, controlling the plastrons internal pressure can improve the air-retention ability, by significantly reducing air shrinking. This was illustrated most effectively by Vüllers *et al.* in pressurized nanofur samples (Fig. 33), which was stable for the whole experiment time (4 hours) when operating at 3.5 bar, and for 2 hours at 4 bar.[115] This is equivalent to a depth at least 250 times greater (40 m) compared with the previous examples. To the best of the authors' knowledge, this is the highest tolerated pressure that has been reported. This would be followed by the porous Ti surfaces reported by Li *et al.*, also discussed in Section 5.2, with an air-layer being sustained under a maximum of 3.5 bar.[141]

Applied flow conditions are highly relevant to many fields (*e.g.* drag reduction), and these testing environments represent a similar challenge to submersion depth, albeit not the same. Experimental conditions across the literature are varied, however, work conducted by Xiang *et al.* on lotus leave (Section 5.2) highlighted the effect of using air-saturated water on enhancing the plastrons stability under 1.5 bar and a flow rate of 23 mL min^{-1}.[174] Compared with the case of using unsaturated water, during which plastrons decayed after 2 minutes, the saturated water extended this time to 4 hours, after which the experiment was terminated (Fig. 35).[174] Although the reported pressure is lower compared with the previous two examples, the combination of this with flow conditions makes it challenging to identify the effect of solely using air-saturated water.

Doubly reentrant SiO_2/Si cavities, reported by Domingues *et al.* (Section 5.1), recorded a breakthrough pressure between 1–1.2 bar, depending on the cavity opening shape and diameter.[188] The non-pressurized nanofur, although failed at much less pressure compared with the pressurized one mentioned earlier in this section (typically 0.9 bar), is still considered to be good relative to many other examples.[115]

While the examples mentioned in this section are considered to be among the best-performing surfaces underwater, they demonstrate how much additional progress is required to attain the targeted properties. For real-life applications (discussed in the following section), where deep immersions and/or high flow rates are expected, these systems currently face major limitations.[91,189,190] Cutting edge research reveals some structural aspects that can enhance plastrons stability generally. These include: (i) low-magnitude roughness (nanoscale), (ii) non-wide grooves with a low gas-to-solid ratio, (iii) ordered roughness textures with sufficient density, and (iv) moderate surface energy. Low-magnitude roughness is more able to preserve a stable air layer for a longer time, as the small air pockets are easier to maintain.[187] Considering the reentrant structures reported by Domingues *et al.*, it was predicted that by reducing the cavities size from micro to nanoscale (typically to 100 nm), the breakthrough pressure will increase to 17 bar.[188] Small, narrow grooves protect trapped air better than wider grooves, as the latter suffer more from oscillating pressures.[191–193] In addition, small plastrons generally result in greater solid–water contact, which although leads to lower WCAs, is considered better for long-term air trapping.[193] Ordered structures ensure no sudden increase in pitch between textures and provide better plastron support, and their high density has the same effect in decreasing the pitch as well.[70,131] The surface energy controls water pinning, with low surface energy coatings not supporting this effect.[115] However, the enhanced air-stability resulting from these structural enhancements may still not be sufficient. Further research should be conducted to improve the properties of the fabricated surfaces and make them adequate for the current needs. Currently, materials have been shown demonstrate resilience to particular environments, but the search for a universal approach is still ongoing.

7 Applications

Superhydrophobic materials are widely covered in detail in the scientific literature for their many proposed application areas, primarily in non-submerged environments. However, the challenges faced in submerged applications differ greatly from those that do not consider trapped air. In simple terms, the material with the highest WCA does not necessarily provide the greatest underwater stability, and so this introduces a layer of complexity in the search for technological solutions. This section covers the most prevalent applications for submerged superhydrophobic materials.

7.1 Drag reduction

One of the main applicational areas for underwater superhydrophobic materials stems from their ability to reduce drag.

Frictional drag results when materials travel through fluid phases, which is highly relevant to marine vessels moving through water. This added drag results in a higher energy requirement, leading to a significant increase in fuel consumption and an increase in transport costs and emissions (CO_2). Marine transportation accounts for 12% of the world's transportation energy consumption, and 60% of this is used to overcome frictional drag, therefore a reduction in these forces would greatly benefit both the environment and economy.[194–196] Fluid drag is not just limited to marine vessels; applications including the transportation of fluid through pipelines would also see a great benefit from the reduction of drag forces. Implementation of drag reduced surfaces would allow for lower power usage by engines and hydraulic pumps, and consequently lower energy consumption and costs. Superhydrophobic materials have been demonstrated as a potential solution for this purpose.

7.1.1 No-slip boundary conditions. For the vast majority of materials, the no-slip boundary condition is an assumption that holds for the flow of Newtonian fluids. The boundary condition states that the surface localised flow (tangential velocity) component of the viscous fluid at the fluid–solid interface relative to the solid is zero.[197] That is to say, the fluid at the interface moves with the same velocity as the solid surface. The fluid molecules at the surface do not move with the flow as they are instead displaced as a result of dominating adhesive forces relative to the cohesive liquid force. The relative fluid velocity, u, therefore decreases with distance, y, from the moving surface as the extra momentum is displaced *via* collisions of fluid molecules. This leads to the formation of a linear velocity profile, Fig. 42, for materials exhibiting the no-slip boundary condition. The difference in velocity between the fluid layers (velocity gradient) is known as the shear rate, $\frac{du}{dy}$.

One of the exceptions to this boundary condition is superhydrophobic surfaces. When air is trapped in the rough micro/nanostructures on a superhydrophobic surface, it creates a complex interface with regions of water–solid and water–air contact. In flow conditions, the water–solid regions adopt a typical flow profile, in contrast, the regions of water–air contact enable water to flow over the structures with an 'effective slip' (Fig. 43). Slip is a microscopic phenomenon in which the relative velocity at the interface is no longer equal to that of the solid. The air–liquid interface has a considerably lower friction force than the corresponding solid–liquid interface creating the apparent slip and allowing for the reduction of drag. The resulting fluid velocity at the surfaces is named the slip velocity, u_0.[198] An effective way of quantifying the level of slip a surface exhibits is by measuring the slip-length, b, which is related to the slip velocity and shear rate by:[198]

$$u_0 = b\left|\frac{du}{dy}\right|$$

The greater the slip-length the greater the reduction of drag forces.[199] However, the relationship of this is dependent on factors such as the type of flow that is occurring.[200,201] Further still, for the drag to be reduced enough that it is of significant value, the slip length must be comparable to the length scale of the flow. As a general rule to achieve a drag reduction of approximately 10%, the slip length should be 10% of the characteristic length scale. For marine vessels, this characteristic value is millimetres in length and as such for marine transport to achieve a 10% reduction of drag, a slip length in the order of 100 μm would be required.[198]

An important detail to bear in mind is that the drag reduction is not directly related to the WCA value and as such, measurement of the WCA alone is not enough to declare a material as drag reducing. For instance, materials that exhibit Wenzel wetting may possess a high WCA but due to the lack of retained air, slip lengths are low and drag reduction will not occur.[198,202] As a result, the design of drag-reducing superhydrophobic materials requires a more in-depth characterization,

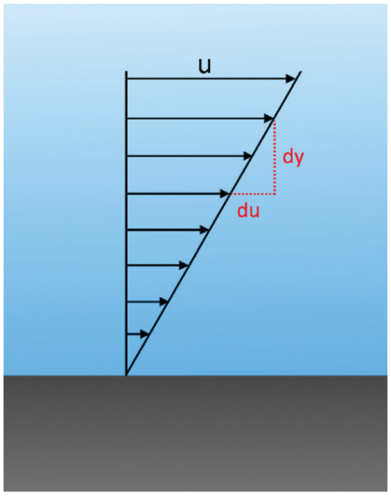

Fig. 42 Schematic showing the velocity profile for the no-slip boundary condition. Velocity, u, of the fluid at the surface is 0 relative to the surface. $\frac{du}{dy}$ represents the shear rate of the fluid.

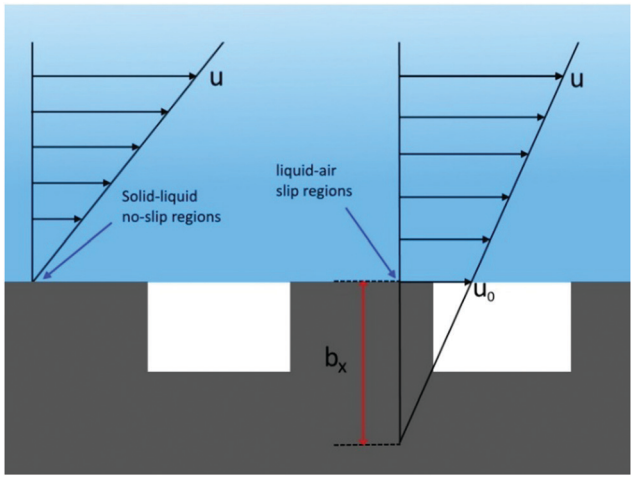

Fig. 43 Schematic showing the velocity profile of a superhydrophobic surface. Regions of solid–water contact show the typical no-slip boundary condition whereas liquid–air regions allow for an "effective slip".

such as measuring surface flow properties like the slip length, to fully quantify the effects and compare materials.

7.1.2 Drag-reduction studies. Many materials have been made for the intention of drag reduction, the slip lengths and reduction percentage of which vary greatly between them. The variation arises from the difference in surface structures and properties, as well as a difference in measuring conditions and techniques. As previously discussed in Section 4.1 fluid shear forces can act to reduce the plastron volume by increasing the pressure felt on the air–water interface. This in-turn can lead to a lowering of drag-reducing potential caused by the trapped air. Quantitative comparison between materials is therefore challenging due to the difference in testing conditions used, as the drag-reducing effect is dependent on both the nature of the plastron and its response to any applied force. Rong *et al.* fabricated complex "flower-like" micro and nanostructures (similar to that of the lotus leaf) onto steel balls using acid etching and oxidation.[203] The treated steel ball had a visibly higher velocity than an untreated ball when moving through water and by calculation using falling time and water volume gave an overall drag reduction of 84.06%. Additional simulations to prove the validity of the experiment using 3D models in laminar conditions showed the highest drag reduction ratio to be 63.4%. Xu *et al.* produced superhydrophobic PTFE by embossing with a fine stainless steel mesh, as well as a spray-coated TiO_2 surface.[204] The slip lengths were accurately measured with a cone and plate rheometer showing drag reductions of 7.0% (b = 27 μm) and 13.3% (b = 55 μm) for the PTFE and TiO_2 surfaces respectively (Fig. 44). The use of rheometric methods allowed for precise measurement of the drag reduction (*via* slip length measurements) lowering the uncertainty of the obtained value as opposed to other measuring techniques.

Rajappan *et al.* evaluated the drag reduction performance of randomly structured superhydrophobic materials.[205] This included aluminium which had been spray-coated with a fluorinated silsesquioxane, chemically etched with acid or sandblasted. Frictional torque measurements allowed for the determination of the slip lengths which ranged from 12.1% (b = 8.4 μm) to 26.9% (b = 32.1 μm). Zhang *et al.* similarly used chemical etching to produce superhydrophobic materials from drag reduction studies.[206] The produced surface consisted of ZnO nanowires on steel substrates and exhibited drag reduction between 40–50% compared to untreated surfaces (Fig. 45).

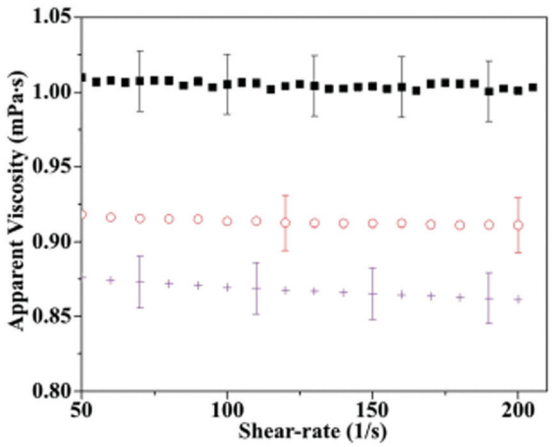

Fig. 44 Slip-length measurements carried out on a cone and plate rheometer. The black square represents water baseline test carried out on a stainless steel surface (b = 0 μm), red circles represent PTFE surface (b = 27 μm) and purple crosses represent TiO_2 surfaces (b = 55 μm). Error bars were calculated by variation from repeats. Reproduced with permission from ref. 204. Copyright (2018) The Royal Society of Chemistry.

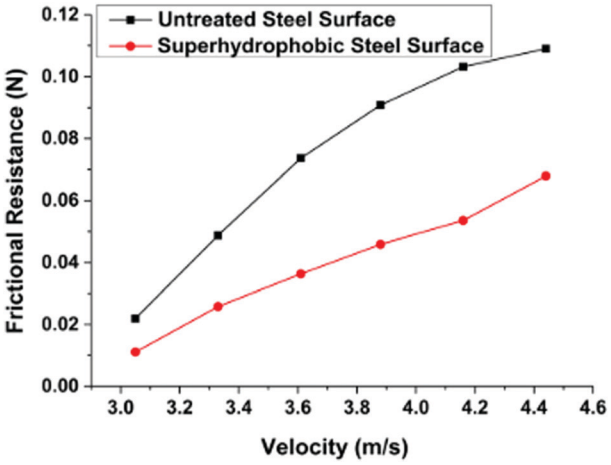

Fig. 45 Change in frictional drag with velocity of water flowing over untreated steel substrated coated in ZnO nanowires. The superhydrophobic surface shows a drag reduction between 40–50% of the untreated surface. Reproduced with permission from ref. 206. Copyright (2017) Institute of Materials, Minerals and Mining Published by Taylor & Francis on behalf of the Institute.

As drag reduction is a direct consequence of trapped air, the surface morphology and chemistry (which control the possible volume of air) are the main influencing factors. For instance, Samah *et al.* demonstrated the effects a random topography had *vs.* microfabricated structures using numerical simulations.[207] Random roughness is highly desirable for real-world applications as they lower costs and for the most part are easier to scale up. The work showed that the random micro-post structure led to lower frictional forces compared to the regular structures, this was amplified with an increased gas fraction. It was believed this is due to the possibility of finding larger areas to flow through which would have lower resistance and hence lower overall friction. As the gas fraction increases, the possibility of these large passages also increases leading to the increased difference in the drag reduction of the two. A similar study was carried out by Aziz *et al.* investigating slip on random and designed granular coatings.[208] Their simulation also varied the hydrostatic pressure so that at an increased pressure the air–water interface moved deeper into the coatings. This meant calculations were undertaken on a curved interface as opposed to the flat interface in the work by Samah *et al.*[207] It showed in all particle arrangements the slip decreased with increased pressure due to the increased wetted contact area. However, the random structures were much more susceptible to wetting with a lower critical hydrostatic pressure. Furthermore, with increased gas fractions (particles more spaced out) the degree of

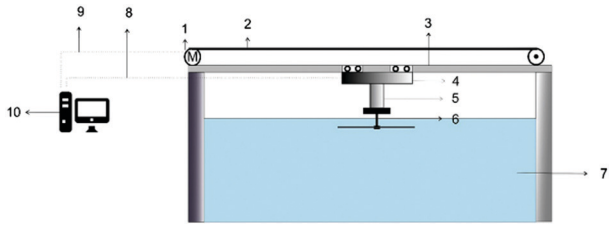

Fig. 46 Schematic of test equipment and tank used by Taghvaei *et al.* (1) Electromotor, (2) cable to transmit motion, (3) supporting structures, (4) datalogger to record drag values, (5) dynamometer to measure exerted drag on the surface by the water, (6) superhydrophobic substrate connected by threaded shaft and nut, (7) towing tank, (8) wire to transmit data, (9) wire to transmit commands and (10) processing computer. Reproduced with permission from ref. 209. Copyright (2017) Elsevier Ltd.

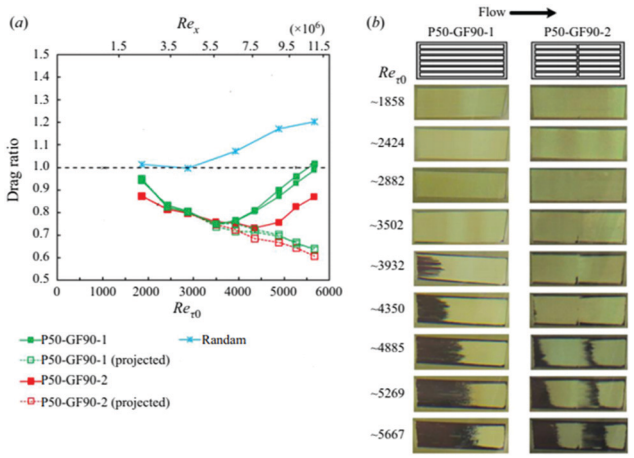

Fig. 47 (a) Towing experiment results showing the drag ratio (relative to a smooth surface). P50-GF90 refers to a pitch of 50 μm and 90% gas area fraction for the trench structures. The ordered trenches were also compared to a random structured superhydrophobic material. On the trenches, drag reduction increased with increased flow rate up until too much wetting occurred at a Re value of $\sim 6 \times 10^6$ and $\sim 8 \times 10^6$, after which the drag reduction began to decrease. The random structure on the other hand showed a continued decrease in drag reduction with increased speed. (b) Pictures of the superhydrophobic surface after towing tests at increasingly high Reynolds numbers. Wetted areas are visible as the darker regions and areas where the plastron remains are bright. An increased loss of air is visible at higher speeds. (a and b) Reproduced with permission from ref. 210. Copyright (2020) Xu *et al.*, Published by Cambridge University Press.

partial wetting is also greatly increased. The increased water penetration will lead to increased friction and as such increased drag. This work by Aziz *et al.* opposes that done by Samah *et al.* and highlights the importance of considering both structural properties and environmental factors such as pressure.[207,208]

Other research has focused on the difference in drag reduction between surfaces with roughnesses on a single scale and one that is hierarchical. Taghvaei *et al.* produced aluminium substrates with a hydrophobic Al_2O_3 micro/nanoparticle coating to create a dual structured surface that could be compared to a non-hierarchical nanostructured counterpart.[209] The surfaces were submerged in water (as shown in Fig. 46) before being moved at a range of velocities, up to 0.5 m s^{-1} and the resulting drag across the surface measured by a dynamometer.

By also testing an as-received aluminium sheet the percentage drag reduction could be calculated. For the hierarchically structured surface, drag reduction was achievable over a wider range of velocities with reductions ranging between 7–77%. On the single scale surface, a drag reduction of 78% was achieved at 0.1 m s^{-1}, however, this decreased with increasing velocity to the point that no reduction was seen at velocities greater than 0.38 m s^{-1}. Furthermore, the drag after this point was even higher than that of the smooth as bought aluminium. It was concluded that on the hierarchical structure, nanoparticles embedded in the micro-particles delay water from entering the pores and so stabilise the trapped air at higher velocities, allowing the air to reduce the drag forces. When only nanoparticles existed, water was easily pushed into the surface at higher velocities, increasing the contact area and hence the drag force.

Recently Xu *et al.* utilised a high-speed towing tank to produce high-Reynolds-number flows, similar to that which would be seen for boats in open waters (Fig. 47).[210] A superhydrophobic surface composed of micro-trenches was chosen in which careful consideration of plastron stability was observed during fabrication. Whilst a larger trench would allow for higher fluid slip and as such greater drag reduction, smaller trenches would increase the stability against diffusion and hydrostatic pressure (Section 4). The final trench composed of a gas fraction of approximately 90%. Further still re-entrant edges were produced to aid in the pinning of the plastron and preserve the drag reduction. The towing speed went to a maximum of 10.06 m s^{-2} ($Re = 1.12 \times 10^7$). The results showed an increase in drag reduction at low/medium speeds up to a maximum of 27%. However, upon reaching higher speeds all drag reduction was lost due to a loss of plastron (as seen *via* optical camera and applied thresholds).[210] This work by Xu *et al.* highlights the importance of reporting testing parameters due to the effect of flow on the measured drag reduction.

All these studies have demonstrated the potential of superhydrophobic surfaces to minimise drag as a direct result of trapped air in a laboratory environment. However, further testing is required if the materials are to be implemented in real-world environments and for long-term use. There are two ways in which the drag-reducing properties of the material can be lost; either through the loss of plastron (*via* diffusion, hydrostatic pressure, *etc.*) or by loss of surface features, the former of which is discussed in Section 4. The micro/nanostructures, fundamental to superhydrophobicity are inherently weak, as such the surface roughness can readily be lost. Unlike the loss of trapped air which can be recovered using techniques such as air injection and gas generation, damage to surface structures is permanent and cannot be recovered. Partial removal of surface roughness by degradation may reduce the volume of air that can be trapped in the surface and hence, increase the extent of drag felt by the surface coating. Further still, complete removal or surface features would result in a complete loss of superhydrophobicity and drag-reducing properties. Therefore, it is vital when fabricating materials and coatings to reduce drag that both the mechanical stability of the surface and the stability of the air layer are considered.

7.2 Antifouling

7.2.1 Process of biofouling. Biofouling refers to the impairment or degradation of surfaces, equipment, and structures, as a result of gradual accumulation, growth, or activity of living organisms such as bacteria (and their extracellular products), protozoa, and other fouling animals on surfaces (Fig. 48).[211,212] For underwater applications, biofouling is a major concern, particularly in the marine sector where biofouling prevention is focused on surface contamination by algae and barnacles.

The biofouling process is generally initiated by the deposition of a conditioning film, which is a thin coating that helps promote microbial attachment, and is primarily composed of proteins and glycoproteins,[211] but may also contain other organic and inorganic molecules.[213] The deposition of proteins on surfaces is largely driven by physiochemical dynamics and protein stability, in addition, electrostatic interactions are also considered to play a role. In an aqueous environment, softer proteins (those with lower internal stability) can denature, exposing hydrophobic cores, which in turn may favourably bind to hydrophobic materials.[214,215] Electrostatic interaction of proteins with the surface is highly dependent on the type of suspension medium, local conditions (*e.g.* temperature), and individual protein characteristics.[216] The formation of the conditioning layer has been shown to occur within minutes of immersion in seawater. In underwater environments, the conditioning layer facilitates the binding of microorganisms including bacteria, diatoms, and animal cells. This biofilm layer is occasionally referred to as the slime layer, as it can dramatically change the texture and appearance of surfaces. For much of the biofilm growth process it is not readily visible, however, the final phase of fouling in marine environments is the growth of macroscopic organisms such as algae.[217]

Once microorganisms establish a biofilm, they can become highly resistant to both chemical and physical means of removal. The biofilm presence can have a considerable effect on a material's performance, for example, an increase in fluid drag, which can drastically decrease the fuel efficiency of marine vessels (as discussed in Section 7.1). Fouling can also accelerate corrosion of marine vessels, as the attachment/growth of biofilms can accelerate surface-based reactions.[218,219] Also, biofouling has associated ecological implications, as it can facilitate the transportation of invasive species to new environments.[211,220]

7.2.2 Motivations and limitations for use in antifouling applications. Most antifouling coatings currently in use prevent surface colonisation through biocidal means; however, many regulatory bodies have sought to restrict the use of biocidal agents, particularly tributyltin, to protect marine environments and human health.[221] Furthermore, while metal-based coatings achieve antifouling properties through oligodynamic effects, killing colonising organisms, it has been demonstrated that biocidal coatings for antifouling surfaces contributed to both decreased susceptibility to heavy metals, as well as traditional antimicrobials.[222] As such, purely biocidal approaches to antifouling are unlikely to be effective in the long term and may have detrimental effects on human and marine ecosystems.

Thus, superhydrophobic surfaces are of growing interest as their antifouling properties do not require biocides, therefore, lowering their ecological impact compared with conventional technologies. Superhydrophobic surfaces are also of particular interest in the prevention of biofouling due to the presence of the plastron. While it has been demonstrated that the presence of an air layer is not a necessary condition for superhydrophobic surfaces to repel all bacteria,[223] the trapped air decreases surface-water contact area, and therefore also limits contact with water-borne components, including proteins and microbes. Thus decreasing the likelihood of hydrophobic and electrostatic interactions and molecular rearrangement/attachment to the surface. Generally, most antifouling approaches tend to be overcome in environments with a high protein concentration.[224]

Considering the highly dynamic and complex nature of the biofouling process, it is not surprising that a universally antifouling design has yet to be reported to our knowledge. Similarly, evaluation of antifouling properties must be done appropriately. It is difficult to conclude as designs are evaluated inconsistently;

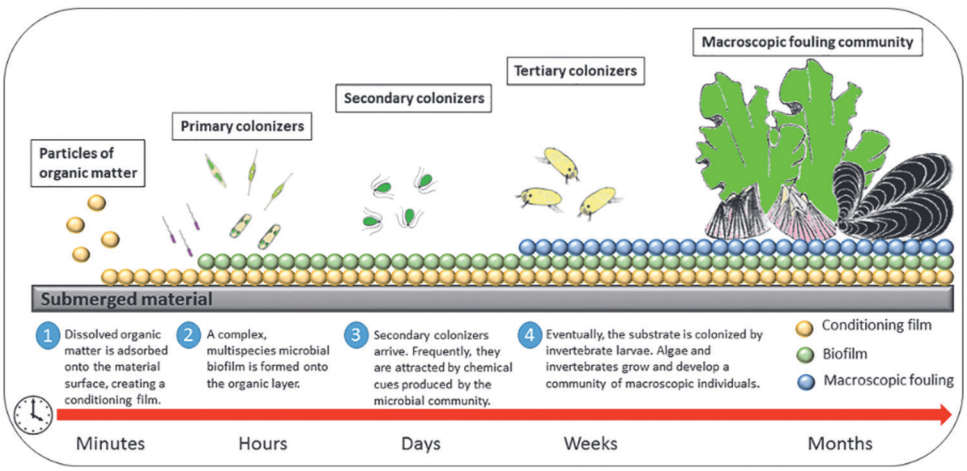

Fig. 48 The sequence and time scale of each stage of the biofouling process. Reproduced with permission from ref. 212. Copyright (2015) Martín-Rodríguez *et al.*

however, certain testing regimes may be more informative of the ultimate performance of an antifouling design than others. For example, Ferrari *et al.*[225] compared commercially available fluoropolymer antifouling blend (non-superhydrophobic) with a superhydrophobic coating on aluminium alloy samples through mesocosm experiments, in which samples were exposed to replicated euphotic seawater conditions for three weeks. Their evaluation demonstrated similar antifouling behaviour between their superhydrophobic coating and a biocidal, fluoropolymer antifouling coating. They also noted that the superhydrophobicity of their surface was ultimately lost, suggesting that other factors such as temperature, sunlight irradiation, and other environmental variables are important factors for the design of superhydrophobic coatings for marine antifouling applications. They also suggest that the process of applying superhydrophobic coatings may be critical in maintaining its properties, as shown in Fig. 49. Methods such as those employed by Ferrari *et al.* in which the material is submerged in its intended environment is likely to be more representative of its overall performance compared to those with laboratory-based approaches since various relevant physiochemical dynamics would be encountered. Furthermore, such an approach does not require prior knowledge of the microbes and proteins that may be present or their behaviour in artificial environments.

Some designs for superhydrophobic surfaces also incorporate bactericidal components such as copper nanoparticles to boost their efficacy.[226] While superhydrophobicity can reduce adhesion, inactivation of adherent bacterial would further prevent biofouling. Antibacterial mechanisms can include photocatalytic effects that produced reactive oxygen species, compromising of the bacterial membrane, or the disruption of electron transport in bacterial membranes.[227] Other designs attempt to prolong the lifespan on antifouling properties by plastron regeneration.[49]

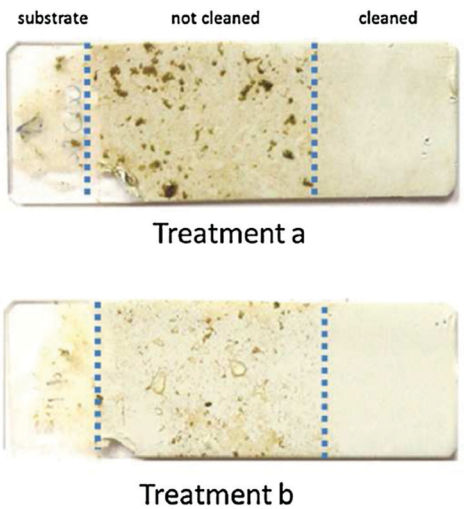

Fig. 49 Macroscopic biofouling coverage after one-week exposure in marine mesocosms that allowed for the development of shallow seawater photobiology. Treatment (a) refers to the application of the superhydrophobic coating when the undercoating was completely dry, treatment (b) refers to the application of the superhydrophobic coating when the substrate undercoat was not yet dry. Reproduced with permission from ref. 225. Copyright (2015) Elsevier B.V.

Currently, universal repulsion of bacteria using superhydrophobic surfaces has yet to be achieved, with current efforts focusing on optimising surface architectures to facilitate this property.[224] When generally considering the microbial adhesion to surfaces, an increase in surface roughness typically enhances bacterial binding – which is not the case for superhydrophobic materials and is likely due to the plastron. Due to the range of protein dynamics and varied microbial adhesion strategies that play a role in the interaction with a material surface, creating a surface that universally repels bacteria under all conditions is unlikely;[228–230] however, strategies to preserve and regenerate the plastron seem to be the most promising. Though even temporary loss of the plastron may facilitate the formation of a conditioning film and negation of superhydrophobic surface architecture. Due to inconsistent testing methodologies, evaluating between designs and drawing generalisable conclusions regarding surface architecture is difficult.

7.3 Underwater gas/involving reactions

Countless chemical reactions involve the generation/consumption of gas. For many of these, the reaction medium is water, bringing to interest the wettability of the reaction catalyst/electrode as it can be crucial in the reaction progression. Well reported examples for such reactions include; hydrogen evolution reactions (HER, gas generation) and oxygen reduction reactions (ORR, gas consumption), which are significant for many applications, particularly those related to energy generation and storage, and chemical synthesis.[62,231–235] Both HER/ORR reactions take place in aqueous media, however, the interfacial chemical dynamics in each reaction necessitate variation in targeted catalyst designs. The surfaces where these reactions take place (*e.g.* catalyst/electrode) play a vital role in facilitating the reaction, which determines its efficiency and resulting industrial costs.[233] For gas-generating reactions, the accumulation of gaseous products on the reaction surface hinders the accessibility of reactants to reaction sites, which significantly lower the reaction efficiency.[233] Surfaces with a hydrophilic nature are desirable for these reactions, as their strong interaction with water would be preferred over gas bubbles, and hence these bubbles would be displaced by water once generated. In contrast, the gas-consuming reactions that occur underwater suffer from the insufficient delivery of reactant gases through water covering the surface, especially if gases involved have low solubilities in water.[64,233] In this case, the surface ability to sustain a gas layer in close proximity to reaction sites is crucial to sustaining an ongoing reaction.[64,233,236]

Complementary to this, underwater gas transportation becomes essential in many processes, including underwater micro-reactions, water treatment, and selective aeration.[237–241] Whether gases are meant to be delivered to the reaction place or removed away from it, controlling the bubbles pathway is important for process completion.[233,242] Generally, bubble movement is influenced by buoyancy forces, which could make the process less concerning in some cases.[237,239] However, when directional

and continuous transportation is required, effective manipulation and control need to be applied. In addition, relying on buoyancy, while being possible for small bubbles, becomes inefficient when bubble volume increases.[233,237,239] For these reasons, finding a method to provide sufficient gas transportation is required.

As the focus in this review is on underwater superhydrophobicity, processes where the air is being pulled away from the surface are not discussed here, as aerophobic (air-repellent) surfaces underwater tend to be hydrophilic in air. Therefore, gas-consuming reactions and gas transportation, as examples for events that need superhydrophobic surfaces, are discussed in this section.

7.3.1 Gas-consuming reactions. Because of the high significance of the electrochemical ORR in many processes, studying the reaction dynamics has received much attention.[232–234,243] A major challenge facing this reaction is the low solubility of O_2 in water, which affects its diffusion to the reaction sites.[64,233] Hence, this slows the reaction kinetics. Investing in the enhancement of catalyst performance, as well as it is not addressing the main issue of reactants accessibility, increases the production cost without significantly boosting the reaction rate.[64,233] An alternative route is to operate the reaction at a three-phase contact point (TPCP), where solid (catalyst), water (electrolyte), and gas (O_2) all meet (Fig. 50). In this way, O_2 can be easily diffused through the air and supplied to feed the reaction. In a commercially-available catalyst, (Fig. 50a), the Pt/C catalyst nanoparticles are directly loaded on a Teflon-treated carbon fiber paper (CFP). This does not allow for as many TPCPs, as the catalyst surface can easily undergo complete wetting, resulting in blocking O_2 pathways.[64] As a response to this problem, Lu *et al.* have suggested a catalyst structure that allows for more abundant TPCPs, as illustrated in Fig. 50b.[64] Here, a superhydrophobic surface of PTFE-modified CoNCNTs (cobalt-incorporated nitrogen-doped carbon-nanotubes) arrays grown on a CFP was generated. The high level of roughness, combined with the hydrophobic nature of the material, enabled a stable O_2 layer which created a TPCP at each CNT tip. Compared with the Pt/C catalyst, CoNCNTs provided a higher current density and, hence, improved performance in both base and acid media.[64]

Another example where the availability of O_2 underwater becomes significant is wastewater treatment. Using photocatalysis to generate charge carriers (*i.e.* electrons/holes) can be effective for the decomposition of organic contaminants.[244] However, electrons and holes can easily recombine again, reducing activity, which is the primary limitation of this process. To avoid this, O_2 is used as a stable carrier for electrons. Sheng *et al.* reported the fabrication of TiO_2-nanoparticles deposited on a porous PTFE-treated carbon fibre substrate.[244] The high porosity of the structure allows water to wet the TiO_2-catalyst surface while not penetrating further to displace trapped O_2, and hence, solid–liquid–gas contact is achieved.[244]

Gao *et al.* have utilized surface-enhanced Raman spectroscopy (SERS) to investigate the effect of surface wetting behaviour on the plasmon-driven catalytic-coupling reaction of *p*-aminothiophenol (PATP) into *p*,*p*′-dimercaptoazobenzene (DMAB), which require the presence of O_2 as an oxidizing agent for PATP molecules.[236] A hierarchical surface made from silver micro-balls decorated with silver nano-dendrites was employed as a SERS active reaction surface, and surface-modification was carried out to make samples with different wetting behaviours; hydrophilic, hydrophobic and superhydrophobic.[236] It was revealed that for superhydrophobic surfaces, a higher Raman intensity was detected for PATP binding to the catalyst surface, indicating an increase in the reaction dynamics.[236]

Other gases have been involved additionally in underwater gaseous reactions. CO_2 reduction provides an interesting way to both recycle CO_2 harmful emissions and to produce other valuable chemicals.[243,245] Chen *et al.* reported the selective reduction into CO using a superhydrophobic carbon nanofibre

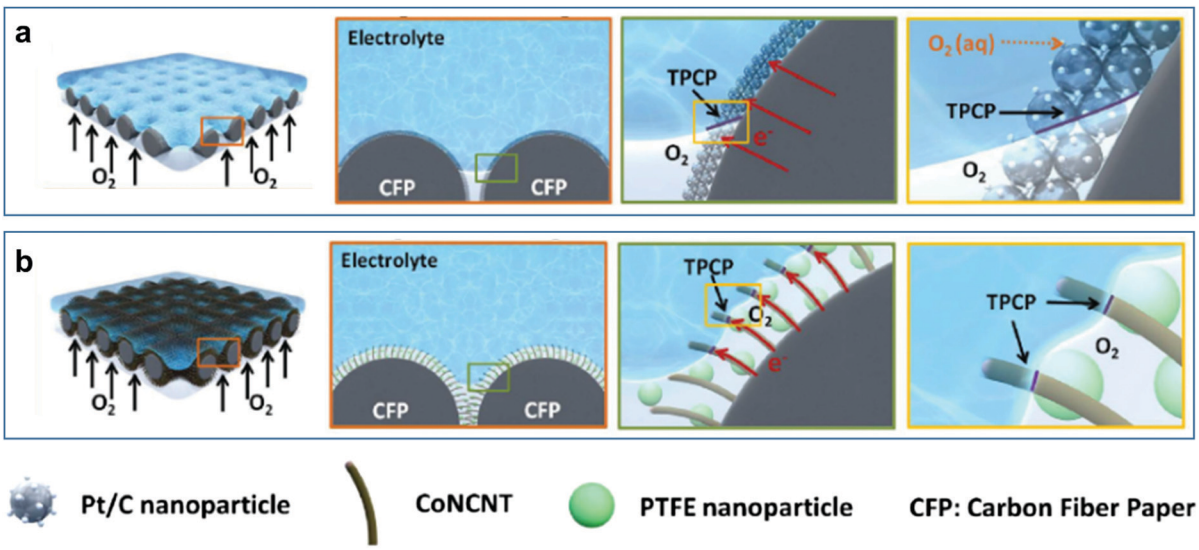

Fig. 50 (a) A schematic for Pt/C commercial catalyst used in ORR, showing the reduced TPCPs and the insufficient delivery of O_2 gas. (b) A schematic for the proposed design using CoNCNT electrode, showing how the structure arrangement allows for higher TPCPs and a sustained layer of O_2 gas. (a and b) Reproduced with permission from ref. 64. Copyright (2016) Wiley-VCH Verlag GmbH & Co. KGaA.

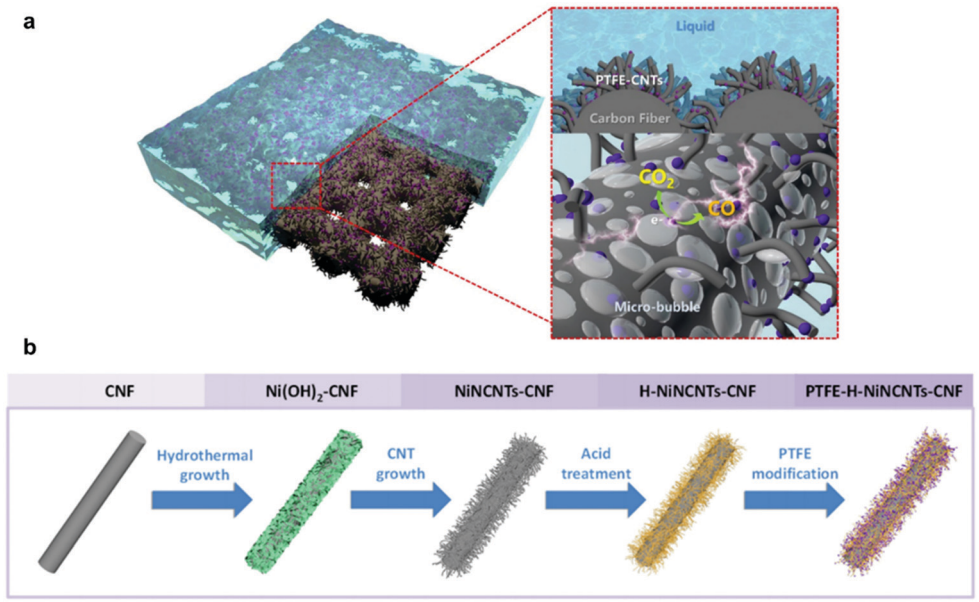

Fig. 51 (a) A schematic for CO_2 reduction reaction over PTFE-H-NiNCNTs-CNF surface. The superhydrophobic nature allows for micro-bubble adhesion on the surface underwater and helps reaction progression. (b) A schematic for the fabrication method. Macroporous CNF were used to vertically grow Ni-incorporated N-doped CNTs and then treated with PTFE to give the hydrophobic properties. (a and b) Reproduced with permission from ref. 243. Copyright (2019) American Chemical Society.

(CNF)-based system, in which Ni-incorporated N-doped CNTs were grown vertically on its surface (Fig. 51).[243] The fibres were then treated by PTFE to add the hydrophobic nature, as well as to enhance the mechanical properties and long-term durability of the system. In addition, the PTFE-H-NiNCNTs-CNF structure enhanced the selectivity of the catalyst to CO_2 reduction over H_2O reduction into H_2, which takes place with the desired reaction for the un-coated NiNCNTs-CNF.[243] This is explained by the superhydrophobic nature of the PTFE-coated fibres, which reduces water binding to the reaction sites and also preserves an air layer to feed the main reaction. Similarly, Cai *et al.* used a PTFE-modified Cu nanoarray electrode for the same reaction.[245] Again, the porous Cu surface allows CO_2 transportation, while the hydrophobic treatment decreased H_2 production to less than the half compared to the untreated electrode.[245]

Another reaction field that has been investigated by Li *et al.* is liquid hydrogenation, which is widely applied in many chemical and pharmaceutical processes.[246] Superhydrophobic surfaces provide a way to solve the main kinetic limitation of these reactions embodied in the low hydrogen concentration in the aqueous environment.[246] Pd catalyst nanoparticles were loaded on a graphene aerogel, and the hydrophilicity of the surface was changed and tested for hydrogenation reaction. The highest observed reaction rate was achieved with superhydrophobic samples.[246]

This concept provides a promising way to enhance the rate and efficiency of gas-consuming reactions that occur underwater. By making participating gases more abundant around the reaction sites, the reaction can progress much further in comparison to other designs that do not prevent a complete wetting of the catalyst. This could lead to a facilitated operation process and lower costs.

7.3.2 Gas transportation. Underwater gas manipulation and transportation is inspired by many natural species, including the diving bell spider (*Argyroneta aquatica*) mentioned earlier in Section 2.1, which can bring air bubbles from the surface and store them underwater for respiration requirements.[75,85] As gas transportation is relevant to many application fields, many reports investigated methods to direct the flow of gas bubbles. Some of them utilise physical properties only, including buoyancy forces, and Laplace pressure gradients with oily/slippery surfaces to control bubble movement.[239,242] Other reports combined this with the chemical superhydrophobic nature of the surfaces utilized. H. Ma *et al.* used sandpaper-roughened polyethene sheets, which was cut into a trapezoidal shape to impose a geometry gradient of bubble movement.[247] This enabled a directional and continuous flow of bubbles.[247] R. Ma *et al.* reported a copper wire with 3D micro-porous structures constructed on the surface, which maintained a constant gas film underwater and allowed for gas capturing and transporting.[248]

Copper cones have been reported for directional transportation.[63,237] Yu *et al.* utilized roughened cones and treated them with a low-surface-energy coating, which showed bubble movement from the cone tip towards the base.[63] This movement direction was maintained regardless of cone alignment, even travelling against buoyancy forces when the cone tip is pointing up (cone is standing vertically on its base). They also reported that higher transportation velocity was achieved with smaller bubble volume and higher apex angles (Fig. 52a–d).[63] In a comparison between superhydrophobic and hydrophobic cones, it was found that hydrophobic cones display a random

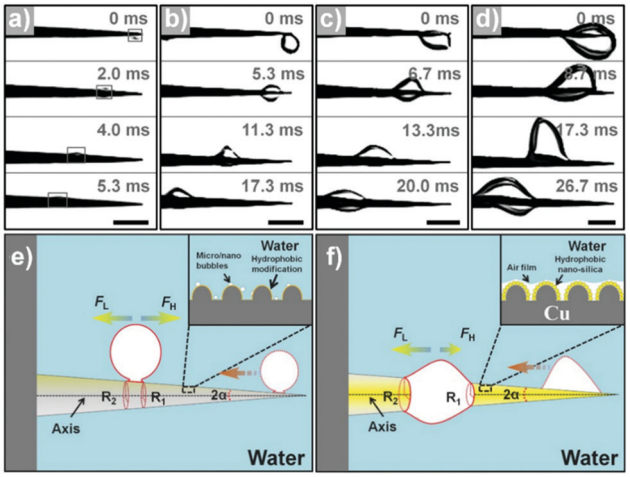

Fig. 52 (a–d) Recorded images for directional transportation of gas bubbles on copper cones with apex angle 5°. The bubble volume used was (a) 0.02, (b) 0.50, (c) 4.20, and (d) 14.20 μL. (e and f) Schematics showing the mechanism of bubble transportation on a hydrophobic (e) and a superhydrophobic (f) copper cones. Randomly-arranged bubbles on the hydrophobic surface, in contrast to the superhydrophobic cone, does not form a continuous air film which increases hysteresis resistance force (F_H). (a–f) Reproduced with permission from ref. 63. Copyright (2016) Wiley-VCH Verlag GmbH & Co. KGaA.

arrangement of micro/nanobubbles adhered to the surface that is not sufficient to facilitate movement. This was rationalised through the high hysteresis resistance force (F_H) acting in the opposite direction of the movement of the bubbles. In contrast, the air film adhering to the superhydrophobic cone surface decreases F_H to almost 0 μN, and hence, the Laplace force (F_L) pushes the bubble along the cone axis (Fig. 52e and f).[63] Benefiting from this, Xue *et al.* applied superhydrophobic copper cones to remove CO_2 microbubbles which stagnate on metal surfaces underwater and accelerate corrosion, leading to potential surface damage.[237] Duan *et al.* replicated this with polymer-based cones (made from PTFE and textured using a two-step femtosecond laser direct writing technique). The cones maintained gas-transport ability after immersion in different corrosive solutions (1 M HCl, 1 M NaOH, and 10 wt% NaCl).[249]

Aiming to achieve a more controlled delivery, Yu *et al.* suggested a superhydrophobic helix structure with a high air-affinity (Fig. 53a–c) to transport bubbles sticking to its surface.[250] The mechanism is illustrated in Fig. 53d and e. Buoyancy forces keep the bubble always adhering to the highest point of the helix rather than sticking to a single physical point on it. Subsequently, the bubble is moving from one helix ring to another, instead of rotating with one single ring. As the helix rotates, the bubble will be remain pushed to the top, which makes the bubble travel along the helix towards the rotation axis. In this way, the transportation velocity can be controlled by changing the spacing length of the helix and rotational speed, with larger spaces and speeds, allowing for faster delivery.[250] The effect of bubble volume was examined, with small bubbles (5 μL) adhering strongly to the helix surface, which causes them to rotate with the helix instead of being moved along it. Conversely, large bubbles (30 μL) were not well adhered to the surface and were easily released from the helix. Volumes between these two extremes could be transported successfully.[250] Due to the high controllability of the delivery speed for such small gas volumes, a micro-reaction between H_2 and O_2 bubbles placed on two attached oppositely-rotating helixes was conducted. This opens pathways for enhancing the efficiency of aqueous reactions in micro-systems.[250]

Cao *et al.* investigated how hydrophilic defects on superhydrophobic surfaces can change the gas-delivery mechanism, and used this to induce directional transportation.[251] Laser ablation was used to create precise defects, ranging between slight, medium and serious. They showed that for a defect-free surface, the bubble tends to spread creating a gas film, and then re-collect and detach at the release point (Fig. 54a). Inducing defects creates a motion barrier, making gas-layer formation difficult. The bubble volume increases (volume of air forming a gas-layer decrease) as defects get more severe, until reaching the surface with serious defects where the transportation is failed (Fig. 54b–d). This is explained by the decreased width

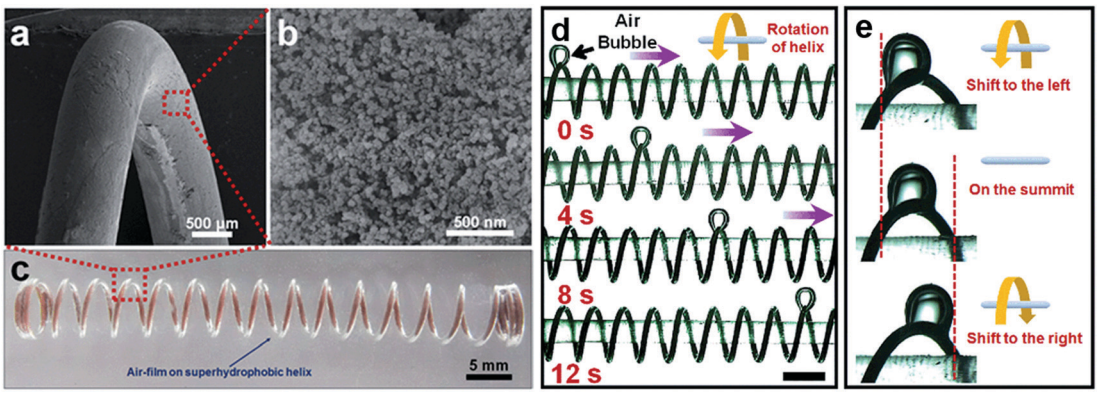

Fig. 53 (a and b) SEM images of the superhydrophobic helix, where the nanostructuring of its surface is shown in (b). (c) An optical picture of the helix underwater, with the shiny surface indicating its superhydrophobicity. (d) Shows the bubble movement with time. As the bubble sticks to the helix summit, the helix rotation makes the bubble shifts to the direction of the rotation axis. Scale bar = 5 mm (e) illustrates how the bubble stays at the helix summit during its rotation. (a–e) Reproduced with permission from ref. 250. Copyright (2016) The Royal Society of Chemistry.

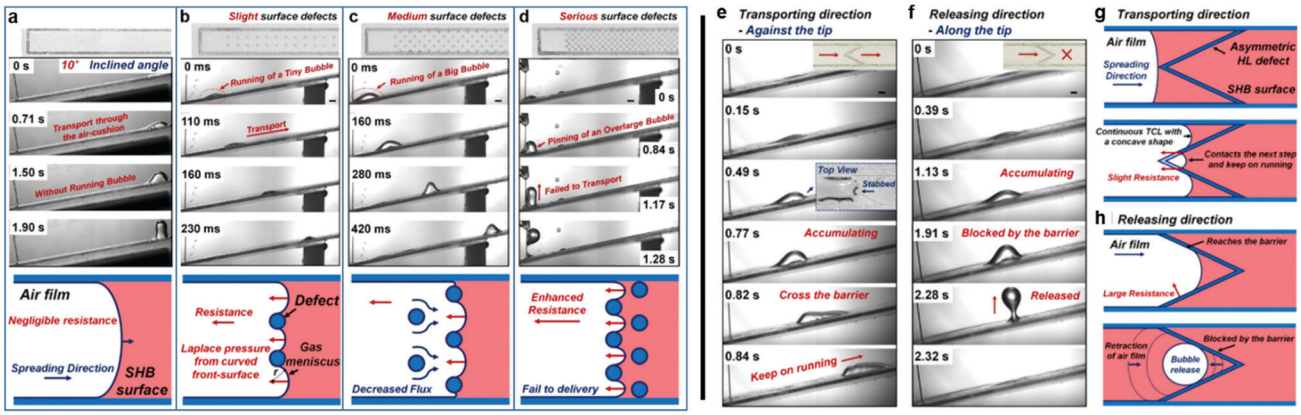

Fig. 54 (a–d) The effect of increased defects on gas transportation behaviour, compared with the defect-free surface. (e–h) An anisotropic defect can support bubble transformation through one direction only and suppress it in the opposite direction. (a–h) Reproduced with permission from ref. 251. Copyright (2018) American Chemical Society.

between two defects, which enhances the surface resistance for bubble motion. Using this finding, an anisotropic angular defect has been created to induce unidirectionality (Fig. 54e–h). In the transporting direction, the bubble starts to accumulate at the small tip of the defect but will pass through it and continue moving. At the release (opposite) direction, the long defect sides will create a larger resistance force, stopping bubble progression.[251]

The previous systems are examples of gas transportation methods on open surfaces. An issue that open surfaces may suffer from is the resistant buoyancy forces, which intensify when the transportation occurs in the opposite direction of the buoyancy force component.[241] A pipe-like design could provide a solution for this, as such forces get reduced in closed surfaces. This also could be beneficial in cases where physical forces become insufficient for transportation, like transporting large bubble volumes or under high depths.[241] Zhang *et al.* suggested superhydrophobic yarn-like fibres were to be used for this purpose.[241] The resistance-force reduction was indicated by the consistent flow from the injection point to the highest escape point (yarn end), regardless of how the yarn was being shaped. Moreover, when the yarn is U-shaped with one of the ends being underwater, the gas flow was observed indicating siphon-effect.[241] Another system that combines both storage and transporting capabilities was reported by Chen *et al.*[240] as a way to collect and eliminate methane generated under oceans and avoid its release into the atmosphere, as it contributes significantly to the greenhouse effect.[252–254] Porous polyurethane sponges were dip-coated by a silica nanoparticles/polystyrene mixture to add the hydrophobic nature. In comparison to other porous materials reported for methane storage (zeolites, metal–organic frameworks, porous coordination polymers, *etc.*), the superhydrophobic nature of these sponges protects them from being filled with water, saving all the storage capability selectively for methane bubbles. The effect of increasing immersion depths on the absorbed methane was found to be advantageous, due to the additional water pressure compressing larger methane volumes into the sponges. Finally, the collection of the absorbed gas from an immersed sponge was achieved by connecting it to a pipe, where the gas was driven along if by the differential pressure.[240]

As a part of constructing a transportation system, it is important to control the pathway of the gas molecules. Fabricating sheets that can either allow/block the gas flow has been reported. Yong *et al.* used femtosecond laser ablation to structure sheet materials (including Al, stainless steel, Cu, Ni, Si (all were subsequently modified by FAS), PTFE and PDMS).[255,256] The resultant material changes its gas-passage behaviour depending on its hydrophobicity state, with the hydrophilic (underwater aerophobic) sheets block gas passage due to low surface affinity to bubble-interaction, and the sheets with opposite properties allow gas flow through them.[256] In another report, they used this behaviour to create a device that removes gas from water and forces it to leave through a designated route.[257] This was made by placing a rough copper mesh (hydrophilic) against water flow as a filter to pass through, while covering a side-hole with FAS-treated mesh (hydrophobic) to act as a gas-exit gate. A similar concept was used to make a gas-collecting device as well.[257]

A more advanced approach was reported by Chen *et al.* for which the gas passage is unidirectional.[258] In the previous examples, the homogeneity in the hydrophobicity state for both sheet sides equalises the passage behaviour in both flow directions. In contrast, Chen *et al.* fabricated a "Janus mesh", which is a mesh with two different wettabilities on each side.[61] TiO_2 nanoparticles were used to cap one side during the hydrophobic treatment, followed by a UV application on that side, generating a hydrophilic-top/superhydrophobic-bottom mesh (Fig. 55a). This hybrid nature of the mesh imposes a single direction delivery of gas bubbles, as bubbles adhere to the superhydrophobic side, resulting in a blockage of flow (Fig. 55b and c).[258] An important difference to note here is that, opposite to the homogeneously hydrophobic membranes, the superhydrophobic (underwater superaerophilic) side in a Janus mesh would block the gas flow through the mesh towards the hydrophilic side. This is explained by the more favoured interaction between

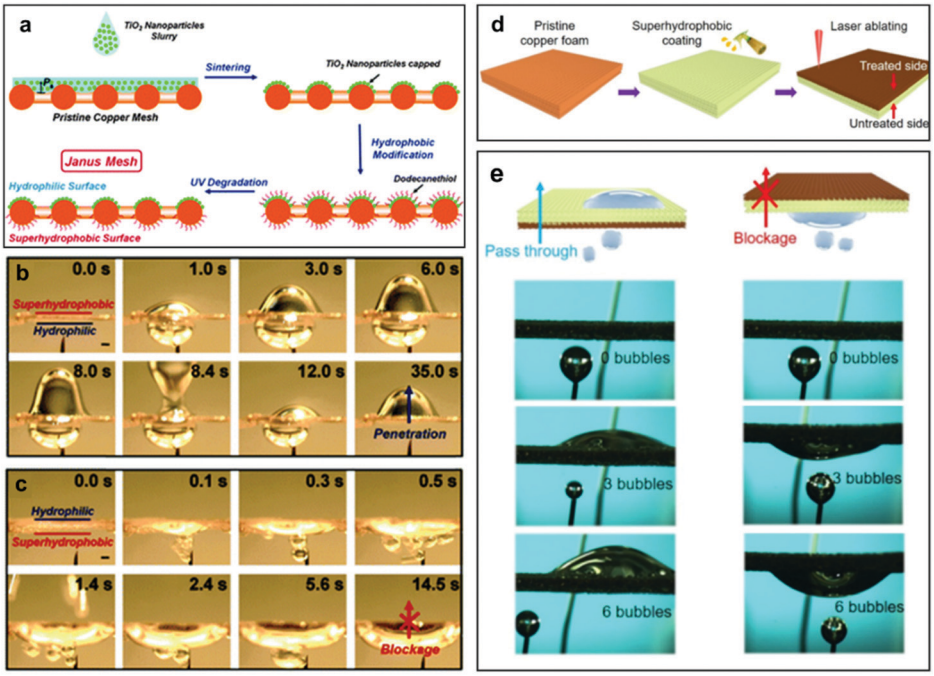

Fig. 55 (a) A schematic for the fabrication of Janus mesh with a TiO_2 nanoparticles hydrophilic-coated side and a hydrophobic-modified copper on the other side. (b and c) shows the penetration/blockage of air bubble travelling through the hydrophilic/superhydrophobic side of the mesh, respectively. (d) A schematic of the fabrication another Janus foam, where laser ablation was used to treat one side of the foam. (e) Shows the passage behaviour of air bubbles through each of the foam sides. (a–c) Reproduced with permission from ref. 258. Copyright (2015) Royal Society of Chemistry. (d and e) Reproduced with permission from ref. 238. Copyright (2020) American Chemical Society.

the superaerophilic side and gas bubbles, in comparison to the aerophobic nature of the other side. This would make bubbles stick to the membrane. In contrast, the unified aerophilic membranes can exchange gases freely between both sides, supporting gas flow. A similar approach was followed by Yin *et al.* who applied femtosecond laser direct writing technology on one side of a PTTE mesh, creating a hydrophobic/superhydrophobic asymmetry.[257] Although the contrast in water-affinity nature was not huge, the hydrophobic side with Wenzel-wetting behaviour supported gas flow. In addition, Zhu *et al.* used laser ablation on one side of a superhydrophobic-coated copper foam to reverse the hydrophobic nature (Fig. 55d and e).[238] This was used to unidirectionally transport CO_2 and collect a maximum of 15 mL cm^{-2} min^{-1} which was effective to neutralize an alkaline solution connected to the Janus foam. This reflects the potential of these systems in underwater organic-gas harvesting.

The achieved progress in making gas-transporting surfaces brings us closer to designing fully functional systems that selectively transport gas to/from the desired media, with a control on the flow parameters that enables optimum results. With remaining challenges relating to transport volume and time, the applicability of the process still needs further developments.

8 Conclusions

The literature covered in this review embraces a range of topics related to air layer stability at submerged superhydrophobic surfaces. The understanding of the impact of the air layer on the surface properties/functionality underwater has been established from various examples of natural underwater superhydrophobic surfaces, like water-bound insects and the famous *Salvinia* leaf. This impact has been utilized to differentiate between different wetting states of the surface and to track the plastron decay, which enables surface characterization using a range of optical, force-based, acoustic and electrochemical methods. With the information obtained using these characterization techniques, different theories have been confirmed to affect plastrons lifetime and challenge their real-life applications. These include pressure exerted by water, diffusion of trapped air and condensation. The understanding of natural occurring plastrons and their performance in challenging environments have been transferred into designing surfaces with high air retention underwater. While some designs were inspired by natural-existing structures, other reports suggested controlling the ambient environment (introducing adjustable plastrons pressure, reducing gas-solubility of water to control plastron diffusion, *etc.*) to reduce its detrimental effect on plastron lifetime. Among these suggested designs, the highest performing materials were highlighted to probe current achievements and to look into their applicability. Finally, examples of applications where underwater air-retention becomes crucial were discussed, these include drag reduction, anti-fouling and underwater gas-consuming processes/gas transportation.

Although reaching a system with ultimate air-layer stability under severe conditions has not been achieved yet, the study of natural systems alongside man-made surfaces have suggested

some common factors that enhance plastrons stability. As discussed, structural factors such as the size of air pockets can affect their lifetime, as smaller pockets tend to show higher stability against the pressure exerted by water. Another structural factor is the fabrication of rough geometries in a controlled/ordered pattern, compared with a statistical/random surface roughness. Random surface designs result in an uneven distribution of pocket sizes/air volumes, which could create points of defects in the surface that are less likely to remain stable with time and can induce a rapid decay of the remaining surface. In addition, although the fundamental science behind air-layer stability is generally well understood (Section 1.3), complexities are observed to arise when precisely engineered surfaces are exchanged for materials with a variant, less ordered morphology. The performance of those materials with irregular air bubble shape/size, distribution, and surrounding surface morphology, are particularly challenging to predict, model, and consequently optimise.[259]

The material choice also has an impact on water-pinning ability. It is suggested that systems with intermediate surface-energy material coatings or hybrid hydrophobic/hydrophilic coatings are more likely to hold water droplet above the air pockets and resist plastrons wetting, compared with superhydrophobic coatings with high water repellence.

Despite the amount of research that has been devoted to improving air-retention ability in superhydrophobic surfaces, there is a large gap between the performances of the developed systems and the targeted performance required for these systems to be implemented in a real-life application. This could be attributed to/hindered for many reasons, including the following:

• The development of underwater superhydrophobic materials involves a more complicated set of properties compared to those required for the typical development of superhydrophobic materials. For a superhydrophobic surface, maximisation of WCAs, and minimising contact angle hysteresis will lead to better functionality. This differs for surfaces fabricated for underwater stability. Particularly, the inclusion of water pinning points and having smaller air/solid ratios, which lead to an increase in the measured WCAs.

• As a result of the advantages offered by uniform surface architectures (highlighted earlier), the research field is dominated by precisely engineered materials with regular surface features. These are generally not suited to real-world application through direct scale-up.

• There is a disparity between some of the proposed testing systems and the consideration of the potential for wider applicability. Although some testing methods have been proven to be effective compared to other designs, these systems can be hard to implement. Some reports recommend putting the whole testing setup under pressure, and others attempted to gas-saturate a large amount of water to control air diffusion. Considering the scaling up of these methods, it would be challenging to ensure the same testing conditions are applied.

The review highlights the optimisation of air-layer stability as a key challenge, specifically, to identify the most successful surface architecture for resisting external degradation forces. The numerous testing methods discussed herein, further emphasises the complexity of monitoring air–water-surface interfaces. Due to this, there is a general lack of consistency across the literature, with many different probing forces (*e.g.* submersion pressure, or water flow rate) implemented, with differences also in adopted monitoring methods. Although not all the mentioned points could be avoided/solved, they open questions and possibilities for future improvements. The scalability and availability of advanced techniques required for designing precisely engineered surfaces could enhance the surfaces applicability and increase the potential for further developments. Adjusting the idealized successful systems to be more suited in the application field is also of great importance to maintain progress in real-life use. In addition, the above conclusions suggest that a unified testing regime for air layer retention would provide a greater understanding, and therefore a more rapid development of these materials. Although this is a logical deduction, it must also be considered that the different testing regimes (*e.g.* submersion depth *vs.* flow intensity) are designed around respective potential application areas. Therefore, a comprehensive examination of air-layer stability must be multifaceted. Future advances in this area must also stem from technological developments, providing greater availability, and methods with superior analytical power. This is of specific relevance to the visualisation in real-time of the complex solid–fluid interface on the micro/nanoscale, which can only currently be achieved through less common techniques including synchrotron X-ray imaging.[260] The real-time monitoring of this interface will allow for a greater predictive ability to be achieved, and true progress to be accomplished.

Conflicts of interest

There are no conflicts to declare.

Acknowledgements

The authors would like to thank the EPSRC and Royal Society for research funding.

References

1 M. Ghasemlou, F. Daver, E. P. Ivanova and B. Adhikari, *J. Mater. Chem. A*, 2019, **7**, 16643–16670.
2 Z. Guo, W. Liu and B.-L. Su, *J. Colloid Interface Sci.*, 2011, **353**, 335–355.
3 Y. Liu, H. Gu, Y. Jia, J. Liu, H. Zhang, R. Wang, B. Zhang, H. Zhang and Q. Zhang, *Chem. Eng. J.*, 2019, **356**, 318–328.
4 W. Barthlott and C. Neinhuis, *Planta*, 1997, **202**, 1–8.
5 Y. Yang, X. Li, X. Zheng, Z. Chen, Q. Zhou and Y. Chen, *Adv. Mater.*, 2018, **30**, 1704912.
6 X. Gao, X. Yan, X. Yao, L. Xu, K. Zhang, J. Zhang, B. Yang and L. Jiang, *Adv. Mater.*, 2007, **19**, 2213–2217.
7 J. Yao, J. Wang, Y. Yu, H. Yang and Y. Xu, *Chin. Sci. Bull.*, 2012, **57**, 2631–2634.
8 G. D. Bixler and B. Bhushan, *Nanoscale*, 2014, **6**, 76–96.

9 C. Neinhuis and W. Barthlott, *Ann. Bot.*, 1997, **79**, 667–677.
10 R. L. Upton and C. R. Crick, *Mol. Syst. Des. Eng.*, 2020, **5**, 876–881.
11 S. Gao, J. Huang, S. Li, H. Liu, F. Li, Y. Li, G. Chen and Y. Lai, *Mater. Des.*, 2017, **128**, 1–8.
12 G. B. Hwang, A. Patir, K. Page, Y. Lu, E. Allan and I. P. Parkin, *Nanoscale*, 2017, **9**, 7588–7594.
13 H. Qian, D. Xu, C. Du, D. Zhang, X. Li, L. Huang, L. Deng, Y. Tu, J. M. C. Mol and H. A. Terryn, *J. Mater. Chem. A*, 2017, **5**, 2355–2364.
14 N. A. Patankar, *Langmuir*, 2004, **20**, 8209–8213.
15 R. Chen, Y. Wan, W. Wu, C. Yang, J.-H. He, J. Cheng, R. Jetter, F. K. Ko and Y. Chen, *Mater. Des.*, 2019, **162**, 246–248.
16 R. Fürstner, W. Barthlott, C. Neinhuis and P. Walzel, *Langmuir*, 2005, **21**, 956–961.
17 R. L. Upton, Z. Davies-Manifold, M. Marcello, K. Arnold and C. R. Crick, *Mol. Syst. Des. Eng.*, 2019, **5**, 477–483.
18 Y. A. Mehanna, R. L. Upton and C. R. Crick, *J. Mater. Chem. A*, 2019, **7**, 7333–7337.
19 H. C. Barshilia and N. Gupta, *Vacuum*, 2014, **99**, 42–48.
20 J. Lomga, P. Varshney, D. Nanda, M. Satapathy, S. S. Mohapatra and A. Kumar, *J. Alloys Compd.*, 2017, **702**, 161–170.
21 Y. Shi, Z. Jiang, J. Cao and K. F. Ehmann, *Appl. Surf. Sci.*, 2020, **500**, 144286.
22 Y. A. Mehanna and C. R. Crick, *Materials*, 2020, **13**, 3160.
23 L. Wen, Y. Tian and L. Jiang, *Angew. Chem., Int. Ed.*, 2015, **54**, 3387–3399.
24 N. Verplanck, Y. Coffinier, V. Thomy and R. Boukherroub, *Nanoscale Res. Lett.*, 2007, **2**, 577.
25 M. Callies and D. Quere, *Soft Matter*, 2005, **1**, 55–61.
26 C. Dorrer and J. Ruhe, *Soft Matter*, 2009, **5**, 51–61.
27 M. Miwa, A. Nakajima, A. Fujishima, K. Hashimoto and T. Watanabe, *Langmuir*, 2000, **16**, 5754–5760.
28 J. Bico, U. Thiele and D. Quéré, *Colloids Surf., A*, 2002, **206**, 41–46.
29 I. U. Vakarelski, N. A. Patankar, J. O. Marston, D. Y. C. Chan and S. T. Thoroddsen, *Nature*, 2012, **489**, 274–277.
30 D. Quéré, *Annu. Rev. Fluid Mech.*, 2013, **45**, 197–215.
31 A. B. D. Cassie and S. Baxter, *Trans. Faraday Soc.*, 1944, **40**, 546–551.
32 R. N. Wenzel, *Ind. Eng. Chem.*, 1936, **28**, 988–994.
33 R. N. Wenzel, *J. Phys. Chem.*, 1949, **53**, 1466–1467.
34 D. Quéré, A. Lafuma and J. Bico, *Nanotechnology*, 2003, **14**, 1109.
35 L. Gao and T. J. McCarthy, *Langmuir*, 2006, **22**, 6234–6237.
36 A. Lafuma and D. Quéré, *Nat. Mater.*, 2003, **2**, 457–460.
37 X. Tian, S. Shaw, K. R. Lind and L. Cademartiri, *Adv. Mater.*, 2016, **28**, 3677–3682.
38 Y. Lu, S. Sathasivam, J. Song, C. R. Crick, C. J. Carmalt and I. P. Parkin, *Science*, 2015, **347**, 1132–1135.
39 R. Gupta, V. Vaikuntanathan and D. Sivakumar, *Colloids Surf., A*, 2016, **500**, 45–53.
40 H. Xu, C. R. Crick and R. J. Poole, *J. Mater. Chem. A*, 2018, **6**, 4458–4465.
41 C. R. Crick, *Superhydrophobic Surfaces-Fabrications to Practical Applications*, IntechOpen, 2018, pp. 11–38.
42 K. Golovin, M. Boban, J. M. Mabry and A. Tuteja, *ACS Appl. Mater. Interfaces*, 2017, **9**, 11212–11223.
43 X. Zhang, D. Zhi, L. Sun, Y. Zhao, M. K. Tiwari, C. J. Carmalt, I. P. Parkin and Y. Lu, *J. Mater. Chem. A*, 2018, **6**, 357–362.
44 D. Quéré, *Annu. Rev. Mater. Res.*, 2008, **38**, 71–99.
45 D. Panchanathan, A. Rajappan, K. K. Varanasi and G. H. McKinley, *ACS Appl. Mater. Interfaces*, 2018, **10**, 33684–33692.
46 L. Whitehead, M. Mossman and A. Kushnir, *Phys. Canada*, 2008, **64**, 7–12.
47 B. V. Hokmabad and S. Ghaemi, *Sci. Rep.*, 2017, **7**, 1–10.
48 C.-H. Xue, X. Bai and S.-T. Jia, *Sci. Rep.*, 2016, **6**, 27262.
49 T. Simovich, A. Rosenhahn and R. N. Lamb, *Adv. Eng. Mater.*, 2020, **22**, 1900806.
50 J. Lee and K. Yong, *NPG Asia Mater.*, 2015, **7**, e201.
51 W. H. Thorpe, *Biol. Rev.*, 1950, **25**, 344–390.
52 M. T. Marx and B. Messner, *Org. Divers. Evol.*, 2012, **12**, 403–408.
53 G. B. Hwang, K. Page, A. Patir, S. P. Nair, E. Allan and I. P. Parkin, *ACS Nano*, 2018, **12**, 6050–6058.
54 F. Cirisano, A. Benedetti, L. Liggieri, F. Ravera, E. Santini and M. Ferrari, *Colloids Surf., A*, 2016, **505**, 158–164.
55 P. Wang, R. Qiu, D. Zhang, Z. Lin and B. Hou, *Electrochim. Acta*, 2010, **56**, 517–522.
56 M. Cheng, M. Song, H. Dong and F. Shi, *Small*, 2015, **11**, 1665–1671.
57 D. Saranadhi, D. Chen, J. A. Kleingartner, S. Srinivasan, R. E. Cohen and G. H. McKinley, *Sci. Adv.*, 2016, **2**(e1600686), 1–9.
58 N. J. Shirtcliffe, G. McHale, M. I. Newton and Y. Zhang, *ACS Appl. Mater. Interfaces*, 2009, **1**, 1316–1323.
59 J. Song, Z. Liu, X. Wang, H. Liu, Y. Lu, X. Deng, C. J. Carmalt and I. P. Parkin, *J. Mater. Chem. A*, 2019, **7**, 13567–13576.
60 J. Yong, F. Chen, Y. Fang, J. Huo, Q. Yang, J. Zhang, H. Bian and X. Hou, *ACS Appl. Mater. Interfaces*, 2017, **9**, 39863–39871.
61 S. Yang, K. Yin, D. Chu, J. He and J. A. Duan, *Appl. Phys. Lett.*, 2018, **113**, 203701.
62 M. Qiao and M. Titirici, *Chem. – Eur. J.*, 2018, **24**, 18374–18384.
63 C. Yu, M. Cao, Z. Dong, J. Wang, K. Li and L. Jiang, *Adv. Funct. Mater.*, 2016, **26**, 3236–3243.
64 Z. Lu, W. Xu, J. Ma, Y. Li, X. Sun and L. Jiang, *Adv. Mater.*, 2016, **28**, 7155–7161.
65 A. A. Hemeda and H. V. Tafreshi, *Langmuir*, 2014, **30**, 10317–10327.
66 J. Zhang, B. Li, L. Wu and A. Wang, *Chem. Commun.*, 2013, **49**, 11509–11511.
67 W. Shen, C. Zhang, Q. Li, W. Zhang, L. Cao and J. Ye, *J. Cleaner Prod.*, 2015, **87**, 762–765.
68 A. Chabas, T. Lombardo, H. Cachier, M. H. Pertuisot, K. Oikonomou, R. Falcone, M. Verità and F. Geotti-Bianchini, *Build. Environ.*, 2008, **43**, 2124–2131.
69 N. J. Shirtcliffe, G. McHale, M. I. Newton, C. C. Perry and F. B. Pyatt, *Appl. Phys. Lett.*, 2006, **89**, 104106.
70 F. Vüllers, S. Peppou-Chapman, M. N. Kavalenka, H. Hölscher and C. Neto, *Phys. Fluids*, 2019, **31**, 12102.

71 W. Barthlott, T. Schimmel, S. Wiersch, K. Koch, M. Brede, M. Barczewski, S. Walheim, A. Weis, A. Kaltenmaier, A. Leder and H. F. Bohn, *Adv. Mater.*, 2010, **22**, 2325–2328.
72 M. A. Samaha, H. Vahedi Tafreshi and M. Gad-el-Hak, *Phys. Fluids*, 2012, **24**, 112103.
73 R. Poetes, K. Holtzmann, K. Franze and U. Steiner, *Phys. Rev. Lett.*, 2010, **105**, 1–4.
74 X. Gao and L. Jiang, *Nature*, 2004, **432**, 36.
75 D. Neumann and D. Woermann, *SpringerPlus*, 2013, **2**, 1–7.
76 Y. Xiang, S. Huang, T. Y. Huang, A. Dong, D. Cao, H. Li, Y. Xue, P. Lv and H. Duan, *Proc. Natl. Acad. Sci. U. S. A.*, 2020, **117**, 2282–2287.
77 A. Balmert, H. Florian Bohn, P. Ditsche-Kuru and W. Barthlott, *J. Morphol.*, 2011, **272**, 442–451.
78 X. Feng and L. Jiang, *Adv. Mater.*, 2006, **18**, 3063–3078.
79 D. J. Crisp and W. H. Thorpe, *Discuss. Faraday Soc.*, 1948, **3**, 210–220.
80 P. Ditsche, E. Gorb, M. Mayser, S. Gorb, T. Schimmel and W. Barthlott, *Appl. Phys. A: Mater. Sci. Process.*, 2015, **121**, 505–511.
81 D. L. Hu, B. Chan and J. W. M. Bush, *Nature*, 2003, **424**, 663–666.
82 M. Dickinson, *Nature*, 2003, **424**, 621–622.
83 M. A. Caponigro and C. H. Eriksen, *Am. Midl. Nat.*, 1976, **95**, 268.
84 C. R. Crick and I. P. Parkin, *Chem. – Eur. J.*, 2010, **16**, 3568–3588.
85 R. S. Seymour and S. K. Hetz, *J. Exp. Biol.*, 2011, **214**, 2175–2181.
86 N. N. Smirnov, *Hydrobiologia*, 1960, **15**, 208–224.
87 N. Andersen, *Vidensk. Meddelelser fra Dansk Naturhistorisk Foren.*, 1976, **139**, 337–396.
88 L. Rowe, *Assoc. Study Anim. Behav.*, 1994, **48**, 1049–1056.
89 M. C. Parsons, *Z. Morphol. Tiere*, 1970, **66**, 242–298.
90 M. Amabili, A. Giacomello, S. Meloni and C. M. Casciola, *Adv. Mater. Interfaces*, 2015, **2**, 1500248.
91 Y. Xue, P. Lv, H. Lin and H. Duan, *Appl. Mech. Rev.*, 2016, **68**, 030803.
92 M. Mail, M. Moosmann, P. Häger and W. Barthlott, *Philos. Trans. R. Soc., A*, 2019, **377**, 20190126.
93 R. Dufour, N. Saad, J. Carlier, P. Campistron, G. Nassar, M. Toubal, R. Boukherroub, V. Senez, B. Nongaillard and V. Thomy, *Langmuir*, 2013, **29**, 13129–13134.
94 J. Yu, H. Wang and X. Liu, *Int. J. Heat Mass Transfer*, 2013, **57**, 299–303.
95 D. Bartolo, F. Bouamrirene, E. Verneuil, A. Buguin, P. Silberzan and S. Moulinet, *Europhys. Lett.*, 2006, **74**, 299–305.
96 R. Dufour, M. Harnois, Y. Coffinier, V. Thomy, R. Boukherroub and V. Senez, *Langmuir*, 2010, **26**, 17242–17247.
97 E. Bormashenko, R. Pogreb, G. Whyman and M. Erlich, *Langmuir*, 2007, **23**, 6501–6503.
98 Z. Han, B. Tay, C. Tan, M. Shakerzadeh and K. Ostrikov, *ACS Nano*, 2009, **3**, 50.
99 D. Wang, Q. Sun, M. J. Hokkanen, C. Zhang, F.-Y. Lin, Q. Liu, S.-P. Zhu, T. Zhou, Q. Chang, B. He, Q. Zhou, L. Chen, Z. Wang, R. H. A. Ras and X. Deng, *Nature*, 2020, **582**, 59.
100 C. Peng, Z. Chen and M. K. Tiwari, *Nat. Mater.*, 2018, **17**, 355–360.
101 C. H. Kung, P. K. Sow, B. Zahiri and W. Mérida, *Adv. Mater. Interfaces*, 2019, **6**, 1900839.
102 N. Saad, R. Dufour, P. Campistron, G. Nassar, J. Carlier, M. Harnois, B. Merheb, R. Boukherroub, V. Senez, J. Gao, V. Thomy, M. Ajaka and B. Nongaillard, *J. Appl. Phys.*, 2012, **112**, 104908.
103 L. Gao and T. J. Mccarthy, *Langmuir*, 2009, **25**, 14105–14115.
104 R. Dufour, M. Harnois, V. Thomy, R. Boukherroub and V. Senez, *Soft Matter*, 2011, **7**, 9380–9387.
105 P. Wang, J. Su, M. Shen, M. Ruths and H. Sun, *Langmuir*, 2017, **33**, 638–644.
106 J. Lee and K. Yong, *J. Mater. Chem.*, 2012, **22**, 20250–20256.
107 D. Axelrod, *Traffic*, 2001, **2**, 764–774.
108 F. A. Schaberle, L. A. Reis, C. Serpa and L. G. Arnaut, *New J. Phys.*, 2019, **21**, 033013.
109 M. S. Bobji, S. V. Kumar, A. Asthana and R. N. Govardhan, *Langmuir*, 2009, **25**, 12120–12126.
110 J. Cheek, A. Steele, I. S. Bayer and E. Loth, *Colloid Polym. Sci.*, 2013, **291**, 2013–2016.
111 B. J. Lee, Z. Zhang, S. Baek, S. Kim, D. Kim and K. Yong, *Sci. Rep.*, 2016, **6**, 1–11.
112 M. A. Samaha, H. Vahedi Tafreshi and M. Gad-el-Hak, *Colloids Surf., A*, 2012, **399**, 62–70.
113 C. Luo, H. Zheng, L. Wang, H. Fang, J. Hu, C. Fan, Y. Cao and J. Wang, *Angew. Chem., Int. Ed.*, 2010, **49**, 9145–9148.
114 M. N. Kavalenka, F. Vüllers, S. Lischker, C. Zeiger, A. Hopf, M. Röhrig, B. E. Rapp, M. Worgull and H. Hölscher, *ACS Appl. Mater. Interfaces*, 2015, **7**, 10651–10655.
115 F. Vüllers, Y. Germain, L. M. Petit, H. Hölscher and M. N. Kavalenka, *Adv. Mater. Interfaces*, 2018, **5**, 1–8.
116 M. Röhrig, M. Mail, M. Schneider, H. Louvin, A. Hopf, T. Schimmel, M. Worgull and H. Hölscher, *Adv. Mater. Interfaces*, 2014, **1**, 1–10.
117 A. Elbourne, M. F. Dupont, S. Collett, V. K. Truong, X. M. Xu, N. Vrancken, V. Baulin, E. P. Ivanova and R. J. Crawford, *J. Colloid Interface Sci.*, 2019, **536**, 363–371.
118 M. Moosmann, T. Schimmel, W. Barthlott and M. Mail, *Beilstein J. Nanotechnol.*, 2017, **8**, 1671–1679.
119 R. Wang, L. Cong and M. Kido, *Appl. Surf. Sci.*, 2002, **191**, 74–84.
120 A. Checco, H. Schollmeyer, J. Daillant, P. Guenoun and R. Boukherroub, *Langmuir*, 2006, **22**, 116–126.
121 M. J. Mayser, H. F. Bohn, M. Reker and W. Barthlott, *Beilstein J. Nanotechnol.*, 2014, **5**, 812–821.
122 J. Su, H. Esmaeilzadeh, P. Wang, S. Ji, M. Inalpolat, M. Charmchi and H. Sun, *Sens. Actuators, A*, 2019, **286**, 115–122.
123 P. Roach, G. McHale, C. R. Evans, N. J. Shirtcliffe and M. I. Newton, *Langmuir*, 2007, **23**, 9823–9830.
124 M. Lee, S. Lee, C. Yim and S. Jeon, *Sens. Actuators, B*, 2015, **220**, 799–804.
125 J. C. Tuberquia, W. S. Song and G. K. Jennings, *Anal. Chem.*, 2011, **83**, 6184–6190.
126 J. C. Tuberquia, N. Nizamidin and G. K. Jennings, *Langmuir*, 2010, **26**, 14039–14046.

127 L. Lei, H. Li, J. Shi and Y. Chen, *Langmuir*, 2010, **26**, 3666–3669.
128 Y. C. Jung and B. Bhushan, *Langmuir*, 2008, **24**, 6262–6269.
129 M. A. Samaha, H. V. Tafreshi and M. Gad-El-Hak, *Langmuir*, 2012, **28**, 9759–9766.
130 J. F. Ou, X. Z. Fang, W. J. Zhao, S. Lei, M. S. Xue, F. J. Wang, C. Q. Li, Y. L. Lu and W. Li, *Langmuir*, 2018, **34**, 5807–5812.
131 B. Emami, H. V. Tafreshi, M. Gad-El-Hak and G. C. Tepper, *Appl. Phys. Lett.*, 2011, **98**, 1–4.
132 P. Lv, Y. Xue, Y. Shi, H. Lin and H. Duan, *Phys. Rev. Lett.*, 2014, **112**, 196101.
133 H. Duan, *Procedia IUTAM*, 2017, **20**, 128–135.
134 H. Wu, Z. Yang, B. Cao, Z. Zhang, K. Zhu, B. Wu, S. Jiang and G. Chai, *Langmuir*, 2016, **33**, 407–416.
135 Y. Xue, S. Chu, P. Lv and H. Duan, *Langmuir*, 2012, **28**, 9440–9450.
136 N. A. Patankar, *Langmuir*, 2016, **32**, 7023–7028.
137 P. S. Epstein and M. S. Plesset, *J. Chem. Phys.*, 1950, **18**, 1505–1509.
138 P. Lv, Y. Xue, H. Liu, Y. Shi, P. Xi, H. Lin and H. Duan, *Langmuir*, 2015, **31**, 1248–1254.
139 D. Dilip, S. Vijay Kumar, M. S. Bobji and R. N. Govardhan, *Int. J. Heat Mass Transfer*, 2018, **119**, 551–563.
140 D. Dilip, N. K. Jha, R. N. Govardhan and M. S. Bobji, *Colloids Surf., A*, 2014, **459**, 217–224.
141 Z. Li, J. Marlena, D. Pranantyo, B. L. Nguyen and C. H. Yap, *J. Mater. Chem. A*, 2019, **7**, 16387–16396.
142 Y. Yang, X. Li, X. Zheng, Z. Chen, Q. Zhou and Y. Chen, *Adv. Mater.*, 2018, **30**, 1–11.
143 O. Tricinci, T. Terencio, B. Mazzolai, N. M. Pugno, F. Greco and V. Mattoli, *ACS Appl. Mater. Interfaces*, 2015, **7**, 25560–25567.
144 D. Zheng, Y. Jiang, W. Yu, X. Jiang, X. Zhao, C. H. Choi and G. Sun, *Langmuir*, 2017, **33**, 13640–13648.
145 B. J. Deka, E. J. Lee, J. Guo, J. Kharraz and A. K. An, *Environ. Sci. Technol.*, 2019, **53**, 4948–4958.
146 C. F. Carlborg and W. van der Wijngaart, *Langmuir*, 2011, **27**, 487–493.
147 P. Du, J. Wen, Z. Zhang, D. Song, A. Ouahsine and H. Hu, *Ocean Eng.*, 2017, **130**, 328–335.
148 C. Lee and C. J. Kim, *Phys. Rev. Lett.*, 2011, **106**, 1–4.
149 A. P. Steigleder and L. Roldo, *Rev. Mater.*, 2019, **24**, e-12480.
150 D. J. Babu, M. Mail, W. Barthlott and J. J. Schneider, *Adv. Mater. Interfaces*, 2017, **4**, 1–6.
151 O. Tricinci, T. Terencio, N. M. Pugno, F. Greco, B. Mazzolai and V. Mattoli, *Micromachines*, 2017, **8**, 366.
152 R. Di Mundo, F. Bottiglione, M. Notarnicola, F. Palumbo and G. Pascazio, *Biomimetics*, 2017, **2**, 1.
153 R. Di Mundo, F. Bottiglione, F. Palumbo, M. Notarnicola and G. Carbone, *J. Colloid Interface Sci.*, 2016, **482**, 175–182.
154 J. H. Crowe and K. A. Magnus, *Comp. Biochem. Physiol., Part A: Mol. Integr. Physiol.*, 1974, **49**, 301–309.
155 M. Akram Raza, E. S. Kooij, A. Van Silfhout and B. Poelsema, *Langmuir*, 2010, **26**, 12962–12972.
156 J. Li, T. Kleintschek, A. Rieder, Y. Cheng, T. Baumbach, U. Obst, T. Schwartz and P. A. Levkin, *ACS Appl. Mater. Interfaces*, 2013, **5**, 6704–6711.
157 R. Helbig, J. Nickerl, C. Neinhuis and C. Werner, *PLoS One*, 2011, **6**, 25105.
158 L. Chen, Z. Guo and W. Liu, *J. Mater. Chem. A*, 2017, **5**, 14480–14507.
159 A. K. Kota, G. Kwon and A. Tuteja, *NPG Asia Mater.*, 2014, **6**, 109.
160 S. R. Gonzalez-Avila, D. M. Nguyen, S. Arunachalam, E. M. Domingues, H. Mishra and C. D. Ohl, *Sci. Adv.*, 2020, **6**, 6192–6219.
161 E. M. Domingues, S. Arunachalam, J. Nauruzbayeva and H. Mishra, *Nat. Commun.*, 2018, **9**, 1–11.
162 E. M. Domingues, S. Arunachalam and H. Mishra, *ACS Appl. Mater. Interfaces*, 2017, **9**, 21532–21538.
163 H. Zhao, K.-C. Park and K.-Y. Law, *Langmuir*, 2012, **28**, 14925–14934.
164 A. Tuteja, W. Choi, M. Ma, J. M. Mabry, S. A. Mazzella, G. C. Rutledge, G. H. McKinley and R. E. Cohen, *Science*, 2007, **318**, 1618–1622.
165 A. Tuteja, W. Choi, J. M. Mabry, G. H. Mckinley, R. E. Cohen and J. M. Prausnitz, *Proc. Natl. Acad. Sci. U. S. A.*, 2008, **105**, 18200–18205.
166 R. Hensel, R. Helbig, S. Aland, A. Voigt, C. Neinhuis and C. Werner, *NPG Asia Mater.*, 2013, **5**, e37.
167 T. Liu and C. J. Kim, *Science*, 2014, **346**, 1096–1100.
168 L. Cao, T. P. Price, M. Weiss and D. Gao, *Langmuir*, 2008, **24**, 1640–1643.
169 L. Cao, H.-H. Hu and D. Gao, *Langmuir*, 2007, **23**, 4310–4314.
170 A. Ahuja, J. A. Taylor, V. Lifton, A. A. Sidorenko, T. R. Salamon, E. J. Lobaton, P. Kolodner and T. N. Krupenkin, *Langmuir*, 2008, **24**, 9–14.
171 A. Grigoryev, I. Tokarev, K. G. Kornev, I. Luzinov and S. Minko, *J. Am. Chem. Soc.*, 2012, **134**, 12916–12919.
172 C. Boo, J. Lee and M. Elimelech, *Environ. Sci. Technol.*, 2016, **50**, 8112–8119.
173 E. J. Lee, B. J. Deka, J. Guo, Y. C. Woo, H. K. Shon and A. K. An, *Environ. Sci. Technol.*, 2017, **51**, 10117–10126.
174 Y. Xiang, S. Huang, P. Lv, Y. Xue, Q. Su and H. Duan, *Phys. Rev. Lett.*, 2017, **119**, 1–5.
175 B. V. Hokmabad and S. Ghaemi, *Sci. Rep.*, 2017, **7**, 1–10.
176 S. S. Latthe, C. Terashima, K. Nakata and A. Fujishima, *Molecules*, 2014, **19**, 4256–4283.
177 X. Sheng and J. Zhang, *Colloids Surf., A*, 2011, **377**, 374–378.
178 Y. Pomeau, M. Le Berre, F. Celestini and T. Frisch, *Comptes Rendus – Mec.*, 2012, **340**, 867–881.
179 M. Shirota, M. A. J. Van Limbeek, C. Sun, A. Prosperetti and D. Lohse, *Phys. Rev. Lett.*, 2016, **116**, 064501.
180 M. S. Bobji, S. V. Kumar, A. Asthana and R. N. Govardhan, *Langmuir*, 2009, **25**, 12120–12126.
181 M. Xu, G. Sun and C. J. Kim, *Phys. Rev. Lett.*, 2014, **113**, 1–5.
182 R. Freeman, A. C. Houck and C. J. Kim, *2015 Transducers – 2015 18th International Conference on Solid-State Sensors, Actuators and Microsystems, TRANSDUCERS 2015*, Institute of Electrical and Electronics Engineers Inc., 2015, pp. 1818–1821.
183 C. Lee, *Langmuir*, 2009, **25**, 12812–12818.
184 Y. Su, B. Ji, K. Zhang, H. Gao, Y. Huang and K. Hwang, *Langmuir*, 2010, **26**, 4984–4989.

185 T. Verho, J. T. Korhonen, L. Sainiemi, V. Jokinen, C. Bower, K. Franze, S. Franssila and R. H. A. Ras, *Proc. Natl. Acad. Sci. U. S. A.*, 2012, **109**, 10210–10213.
186 C. Lee and C. J. Kim, *J. Microelectromech. Syst.*, 2012, **21**, 712–720.
187 A. Aránzazu Martínez-Gómezgómez, S. Lópezlópez, T. García, R. De-Francisco, P. Tiemblo and N. García, *ACS Omega*, 2017, **2**, 8928–8939.
188 E. M. Domingues, S. Arunachalam, J. Nauruzbayeva and H. Mishra, *Nat. Commun.*, 2018, **9**, 1–11.
189 K. Chen, Y. Wu, S. Zhou and L. Wu, *Macromol. Rapid Commun.*, 2016, **37**, 463–485.
190 K. Liu, X. Yao and L. Jiang, *Chem. Soc. Rev.*, 2010, **39**, 3240–3255.
191 L. Piao and H. Park, *Langmuir*, 2015, **31**, 8022–8032.
192 J. R. Panter and H. Kusumaatmaja, *J. Phys.: Condens. Matter*, 2017, **29**, 084001.
193 M. Lee, C. Yim and S. Jeon, *Appl. Phys. Lett.*, 2015, **106**, 011605.
194 M. Lynes, *International energy outlook 2016, Transportation Sector*, 2016.
195 M. Xu, A. Grabowski, N. Yu, G. Kerezyte, J. W. Lee, B. R. Pfeifer and C. J. Kim, *Phys. Rev. Appl.*, 2020, **13**, 1.
196 S. A. Mäkiharju, M. Perlin and S. L. Ceccio, *Int. J. Nav. Archit. Ocean Eng.*, 2012, **4**, 412–422.
197 R. S. Voronov, D. V. Papavassiliou and L. L. Lee, *Chem. Phys. Lett.*, 2007, **441**, 273–276.
198 C. Lee, C. H. Choi and C. J. Kim, *Exp. Fluids*, 2016, **57**, 1–20.
199 K. Watanabe, *Am. J. Sci. Technol.*, 2015, **2**, 106–110.
200 C. H. Choi and C. J. Kim, *Phys. Rev. Lett.*, 2006, **96**, 1–4.
201 C. H. Choi, U. Ulmanella, J. Kim, C. M. Ho and C. J. Kim, *Phys. Fluids*, 2006, **18**, 087105.
202 M. Liravi, H. Pakzad, A. Moosavi and A. Nouri-Borujerdi, *Prog. Org. Coat.*, 2020, **140**, 105537.
203 W. Rong, H. Zhang, Z. Mao, X. Liu and K. Song, *Mater. Res. Express*, 2020, **7**, 015092.
204 H. Xu, C. R. Crick and R. J. Poole, *J. Mater. Chem. A*, 2018, **6**, 4458–4465.
205 A. Rajappan, K. Golovin, B. Tobelmann, V. Pillutla, W. C. Abhijeet, A. Tuteja and G. H. Mckinley, *Phys. Fluids*, 2019, **31**, 042107.
206 H. Zhang, Y. Tuo, Q. Wang, B. Jin, L. Yin and X. Liu, *Surf. Eng.*, 2018, **34**, 596–602.
207 M. A. Samaha, H. Vahedi Tafreshi and M. Gad-el-Hak, *Phys. Fluids*, 2011, **23**, 012001.
208 H. Aziz and H. V. Tafreshi, *Int. J. Multiphase Flow*, 2018, **98**, 128–138.
209 E. Taghvaei, A. Moosavi, A. Nouri-Borujerdi, M. A. Daeian and S. Vafaeinejad, *Energy*, 2017, **125**, 1–10.
210 M. Xu, N. Yu, J. Kim and C. J. C. Kim, *J. Fluid Mech.*, 2020, **908**, 6.
211 H. Dang and C. R. Lovellc, *Am. Soc. Microbiol.*, 2015, **80**, 91–138.
212 A. J. Martín-Rodríguez, J. M. F. Babarro, F. Lahoz, M. Sansón, V. S. Martín, M. Norte and J. J. Fernández, *PLoS One*, 2015, **10**, 0123652.
213 A. Jain and N. B. Bhosle, *Biofouling*, 2009, **25**, 13–19.
214 E. Ostuni, B. A. Grzybowski, M. Mrksich, C. S. Roberts and G. M. Whitesides, *Langmuir*, 2003, **19**, 1861–1872.
215 C. Compère, M. Bellon-Fontaine, P. Bertrand, D. Costa, P. Marcus, C. Poleunis, C. Pradier, B. Rondot and M. G. Walls, *Biofouling*, 2001, **17**, 129–145.
216 M. Ferrari and A. Benedetti, *Adv. Colloid Interface Sci.*, 2015, **222**, 291–304.
217 Z. Li and Z. Guo, *Nanoscale*, 2019, **11**, 22636–22663.
218 M. Smith, M. Bardiau, R. Brennan, H. Burgess, J. Caplin, S. Ray and T. Urios, *npj Mater. Degrad.*, 2019, **3**, 37.
219 R. E. Melchers and R. J. Jeffrey, *Corros. Eng., Sci. Technol.*, 2013, **48**, 496–505.
220 C. Hellio and D. M. Yebra, in *Woodhead Publishing Series in Metals and Surface Engineering*, ed. C. Hellio and D. M. Yebra, Advances in Marine Antifouling Coatings and Technologies, Woodhead Publishing, 2009, pp. 1–15.
221 M. Cloutier, D. Mantovani and F. Rosei, *Trends Biotechnol.*, 2015, **33**, 637–652.
222 C. F. Flach, C. Pal, C. J. Svensson, E. Kristiansson, M. Östman, J. Bengtsson-Palme, M. Tysklind and D. G. J. Larsson, *Sci. Total Environ.*, 2017, **590–591**, 461–468.
223 M. Mateescu, S. Knopf, F. Mermet, P. Lavalle and L. Vonna, *Langmuir*, 2020, **36**, 1103–1112.
224 K. Ellinas, D. Kefallinou, K. Stamatakis, E. Gogolides and A. Tserepi, *ACS Appl. Mater. Interfaces*, 2017, **9**, 39781–39789.
225 M. Ferrari, A. Benedetti, E. Santini, F. Ravera, L. Liggieri, E. Guzman and F. Cirisano, *Colloids Surf., A*, 2015, **480**, 369–375.
226 E. Ozkan, C. C. Crick, A. Taylor, E. Allan and I. P. Parkin, *Chem. Sci.*, 2016, **7**, 5126–5131.
227 A. J. Huh and Y. J. Kwon, *J. Controlled Release*, 2011, **156**, 128–145.
228 K. A. Poelstra, N. A. Barekzi, A. M. Rediske, A. G. Felts, J. B. Slunt and D. W. Grainger, *J. Biomed. Mater. Res.*, 2002, **60**, 206–215.
229 T. Harder and L. H. Yee, in *Woodhead Publishing Series in Metals and Surface Engineering*, ed. C. Hellio and D. M. Yebra, Advances in Marine Antifouling Coatings and Technologies, Woodhead Publishing, 2009, pp. 113–131.
230 Y. Yuan, M. P. Hays, P. R. Hardwidge and J. Kim, *RSC Adv.*, 2017, **7**, 14254–14261.
231 J. D. Benck, T. R. Hellstern, J. Kibsgaard, P. Chakthranont and T. F. Jaramillo, *ACS Catal.*, 2014, **4**, 3957–3971.
232 M. Qiao and M.-M. Titirici, *Carbon Hybrids Electrocatalysts for Oxygen Reduction Reaction in Fuel Cells*, 2018.
233 C. Yu, P. Zhang, J. Wang and L. Jiang, *Adv. Mater.*, 2017, **29**, 1703053.
234 C. Huang and Z. Guo, *Nanoscale*, 2018, **10**, 19659–19672.
235 W. Xu, Z. Lu, X. Sun, L. Jiang and X. Duan, *Acc. Chem. Res.*, 2018, **51**, 1590–1598.
236 Y. Gao, N. Yang, S. Lu, T. You and P. Yin, *J. Mater. Chem. C*, 2019, **7**, 9926–9932.
237 X. Xue, C. Yu, J. Wang and L. Jiang, *ACS Nano*, 2016, **10**, 10887–10893.
238 S. Zhu, J. Li, S. Cai, Y. Bian, C. Chen, B. Xu, Y. Su, Y. Hu, D. Wu and J. Chu, *ACS Appl. Mater. Interfaces*, 2020, **12**, 18110–18115.

239 C. Zhang, B. Zhang, H. Ma, Z. Li, X. Xiao, Y. Zhang, X. Cui, C. Yu, M. Cao and L. Jiang, *ACS Nano*, 2018, **12**, 2048–2055.
240 X. Chen, Y. Wu, B. Su, J. Wang, Y. Song and L. Jiang, *Adv. Mater.*, 2012, **24**, 5884–5889.
241 X. Zhang, Y. Dong, Z. He, H. Gong, X. Xu, M. Zhao and H. Qin, *ACS Appl. Mater. Interfaces*, 2020, **12**, 18174–18181.
242 C. Yu, X. Zhu, K. Li, M. Cao and L. Jiang, *Adv. Funct. Mater.*, 2017, **27**, 1701605.
243 R. Chen, W. Tian, Y. Jia, W. Xu, F. Chen, X. Duan, Q. Xie, C. Hu, W. Liu, Y. Zhao, Y. Kuang, Y. Zhang and X. Sun, *ACS Appl. Energy Mater.*, 2019, **2**, 3991–3998.
244 X. Sheng, Z. Liu, R. Zeng, L. Chen, X. Feng and L. Jiang, *J. Am. Chem. Soc.*, 2017, **139**, 12402–12405.
245 Z. Cai, Y. Zhang, Y. Zhao, Y. Wu, W. Xu, X. Wen, Y. Zhong, Y. Zhang, W. Liu, H. Wang, Y. Kuang and X. Sun, *Nano Res.*, 2019, **12**, 345–349.
246 Z. Li, C. Cao, Z. Zhu, J. Liu, W. Song and L. Jiang, *Adv. Mater. Interfaces*, 2018, **5**, 1801259.
247 H. Ma, M. Cao, C. Zhang, Z. Bei, K. Li, C. Yu and L. Jiang, *Adv. Funct. Mater.*, 2018, **28**, 1705091.
248 R. Ma, J. Wang, Z. Yang, M. Liu, J. Zhang and L. Jiang, *Adv. Mater.*, 2015, **27**, 2384–2389.
249 J. A. Duan, X. Dong, K. Yin, S. Yang and D. Chu, *Appl. Phys. Lett.*, 2018, **113**, 203704.
250 C. Yu, X. Zhu, M. Cao, C. Yu, K. Li and L. Jiang, *J. Mater. Chem. A*, 2016, **4**, 16865–16870.
251 M. Cao, Z. Li, H. Ma, H. Geng, C. Yu and L. Jiang, *ACS Appl. Mater. Interfaces*, 2018, **10**, 20995–21000.
252 W. T. Wood, J. F. Gettrust, N. R. Chapman, G. D. Spence and R. D. Hyndman, *Nature*, 2002, **420**, 656–660.
253 E. D. Sloan, *Nature*, 2003, **426**, 353–359.
254 D. A. Lashof and D. R. Ahuja, *Nature*, 1990, **344**, 529–531.
255 J. Yong, S. C. Singh, Z. Zhan, F. Chen and C. Guo, *ACS Appl. Mater. Interfaces*, 2019, **11**, 8667–8675.
256 J. Yong, F. Chen, J. Huo, Y. Fang, Q. Yang, J. Zhang and X. Hou, *Nanoscale*, 2018, **10**, 3688–3696.
257 J. Yong, F. Chen, W. Li, J. Huo, Y. Fang, Q. Yang, H. Bian and X. Hou, *Glob. Challenges*, 2018, **2**, 1700133.
258 J. Chen, Y. Liu, D. Guo, M. Cao and L. Jiang, *Chem. Commun.*, 2015, **51**, 11872–11875.
259 A. A. Hemeda and H. V. Tafreshi, *Langmuir*, 2014, **30**, 10317–10327.
260 D. I. Yu, S. Doh, H. J. Kwak, J. Hong, N. P. Sapkal and M. H. Kim, *Langmuir*, 2019, **35**, 6460–6467.

